ANKARA YILDIRIM BEYAZIT UNIVERSITY

GRADUATE SCHOOL OF NATURAL AND APPLIED SCIENCES

LIQUID PHASE SINTERING CHARACTERISTICS OF TUNGSTEN POWDER OBTAINED BY ELECTROCHEMICAL REDUCTION TECHNIQUE

M.Sc. Thesis by

Mahmut EROL

Department of Materials Engineering

July, 2017

ANKARA

LIQUID PHASE SINTERING CHARACTERISTICS OF TUNGSTEN POWDER OBTAINED BY ELECTROCHEMICAL REDUCTION TECHNIQUE

A Thesis Submitted to

The Graduate School of Natural and Applied Sciences of

Ankara Yıldırım Beyazıt University

In Partial Fulfillment of the Requirements for the Degree of Master of Science in Materials Engineering, Department of Materials Engineering

by

Mahmut EROL

July, 2017

ANKARA

M.Sc. THESIS EXAMINATION RESULT FORM

We have read the thesis entitled **"LIQUID PHASE SINTERING CHARACTERISTICS OF TUNGSTEN POWDER OBTAINED BY ELECTROCHEMICAL REDUCTION TECHNIQUE"** completed by **MAHMUT EROL** under the supervision of **ASSIST. PROF. DR. METEHAN ERDOĞAN** and we certify that in our opinion it is fully adequate, in scope and in quality, as a thesis for the degree of Master of Science.

Assist. Prof. Dr. Metehan ERDOĞAN

Supervisor

Prof. Dr. Cihangir DURAN

Jury Member

Prof. Dr. İshak KARAKAYA

Jury Member

Prof. Dr. Fatih V. ÇELEBİ

Director

Graduate School of Natural and Applied Sciences

ETHICAL DECLARATION

I hereby declare that, in this thesis which has been prepared in accordance with the Thesis Writing Manual of Graduate School of Natural and Applied Sciences,

- All data, information and documents are obtained in the framework of academic and ethical rules,

- All information, documents and assessments are presented in accordance with scientific ethics and morals,

- All the materials that have been utilized are fully cited and referenced,

- No change has been made on the utilized materials,

- All the works presented are original,

and in any contrary case of above statements, I accept to renounce all my legal rights.

Date: 04.07.2017

Signature:

Name & Surname: Mahmut EROL

ACKNOWLEDGMENTS

Foremost, I would like to thank my supervisor Assist. Prof. Dr. Metehan ERDOĞAN, for his scientific and humanitarian supports. His immense experience and invaluable advices help me while writing this thesis.

I also want to thank my thesis defense committee members, Prof. Dr. İshak KARAKAYA and Prof. Dr. Cihangir DURAN for their valuable contributions and constructive criticisms.

Electrochemically produced tungsten powder, which was employed in this study, was provided by the Thermochemical and Electrochemical Materials Processing Laboratory (TEMP LAB) of METU. In addition, characterization tests of initial powders and sintered specimens were performed in the Department of Metallurgical and Materials Engineering of METU.

I am indebted to all my friends and colleagues, especially, Mustafa ARAS, Oğuzhan DALDAL for sintering treatments and technical supports. In addition, I would like to thank Göhkan POLAT, Olgun YILMAZ, Semih AĞCA, Furkan ÖZDEMİR and Rauf AKSU for their contributions in characterization processes.

Last but not the least; I should express my profound appreciations to my wife, Sema AYAR EROL, our little pretty son, Toprak Aras EROL, and our families for their continuous support and encouragements.

2017, 4 July   **Mahmut EROL**

LIQUID PHASE SINTERING CHARACTERISTICS OF TUNGSTEN POWDER OBTAINED BY ELECTROCHEMICAL REDUCTION TECHNIQUE

ABSTRACT

A remarkable alternative extraction process has recently been announced for tungsten powder production, which is simpler and safer than the conventional fabrication method. Even though the process has a promising commercializing potential, sintering behavior of the produced tungsten powder has not been investigated up to now.

In this study, sintering behavior of the electrochemically produced tungsten powder was investigated and compared with a commercially available tungsten powder. Unalloyed and alloyed specimens, containing at least ninety weight percent commercial or produced tungsten powder, were sintered with different sintering conditions. The alloys had single additives W/X (X:Ni, Co, Fe) or different Ni/Fe, Co/Fe an Ni/Co/Fe ratios.

A series of characterization techniques were performed to investigate the micro and macro scale property variations in prepared pellets. The sintered densities of the specimens were measured by Archimedes method. Microstructure investigations were conducted by optical microscope (OM) and scanning electron microscope (SEM). In addition, x-ray diffractometry (XRD), x-ray fluorescence (XRF) and energy dispersive spectroscope (EDS) analyses were applied to determine the formed intermetallics, solid solution phases as well as impurities and their ratios. The mechanical properties of the selected specimens were measured using micro and macro hardness tests.

It was found that electrochemically produced tungsten powder employed heavy alloys could not densify up to expected relative density values, whereas the unalloyed ones demonstrated higher densification tendency than commercial tungsten pellets. This behavior was attributed to impurity content of the electrochemically produced tungsten.

Keywords: Tungsten, electrodeoxidation, calcium, solubility effect on densification, tungsten heavy alloys, solid state sintering, liquid phase sintering.

ELEKTROKİMYASAL İNDİRGEME TEKNİĞİ İLE ELDE EDİLMİŞ TUNGSTEN TOZUNUN SIVI FAZ SİNTERLEME KARAKTERİSTİĞİ

ÖZ

Geleneksel tungsten tozu üretim methodundan daha basit ve daha güvenli dikkate değer bir alternatif ekstrasyon prosesi yakın zamanda duyurulmuştur. Umut vaad eden bir ticarileşme potansiyeline sahip olmasına rağmen, üretilmiş tozun sinterleme davranışı bugüne kadar incelenmemiştir.

Bu çalışmada, elektrokimyasal olarak üretilmiş tungsten tozunun sinterleme davranışı araştırılmış ve ticari olarak ulaşılabilir bir tungsten tozu ile karşılaştırılmıştır. Alaşımsız ve en az ağırlıkça yüzde doksan ticari ya da üretilmiş tungsten tozu içeren alaşımlı numuneler farklı sinterleme koşullarında sinterlenmiştir. Alaşımlar tek ilaveler W/X (X:Ni, Co, Fe) ve farklı Ni/Co, Ni/Fe, Co/Fe ve Ni/Co/Fe oranlarına sahiptir.

Mikro ve makro ölçekte özellik değişimlerini incelemek için hazırlanan peletlere bir dizi karakterizasyon yöntemleri uygulanmıştır. Arşimet metodu ile numunelerin sinterlenmiş yoğunlukları ölçülmüştür. Mikroyapı incelemeleri ışık mikroskobu (OM) ve tarama elektron mikroskobuyla (SEM) yapılmıştır. Ayrıca, oluşan intermetalikleri, katı çözelti fazlarının yanı sıra safsızlıklar ve bunların oranlarını belirlemek için X-ışını kırınım cihazı (XRD), x-ışını florışıması (XRF) ve enerji dağılımlı spektroskopi (EDS) analizleri uygulanmıştır. Seçili numunelerin mekanik özellikleri mikro ve makro tip sertlik testleri kullanılarak ölçülmüştür.

Üretilmiş tungsten tozunun kullanıldığı ağır alaşımlar beklenen görünür yoğunluk değerlerine yoğunlaşamadığı tespit edilmiştir, oysa alaşımsız peletleri ticari tungsten peletlerine göre daha yüksek yoğunlaşma eğilimi göstermiştir. Bu davranış, elektrokimyasal olarak üretilmiş tungsten tozunun empürite içeriğine dayandırılmıştır.

Anahtar Kelimeler: Tungsten, elektrodeoksidasyon, kalsiyum, çözünürlüğün yoğunlaşmaya etkisi, tungsten ağır alaşımları, katı hal sinterleme, sıvı faz sinterleme.

vi

CONTENTS

LIST OF SYMBOLS

Roman Letter Symbols

D	Diffusion coefficient
D_o	Pre-exponential factor
Q	Activation energy
R	Gas constant
T	Absolute temperature, (°C)
T_m	Melting point (°C)
r	Radius of curvature
G	Sintered grain size
G_o	Initial grain size
K	Growth rate constant
t	Dwell time
N_A	Number of grains per square millimeter
N_{inside}	Number of complete grains in circle
$N_{intercept}$	Number of grains intercepted via circle
f	Jefferies multiplier
$\bar{A}$	Average grain area for each alloy
l	Liter
N	Newton

Greek Letter Symbols

Ψ	Densification parameter
ρ	Density g/cm^3
Δ	Difference
σ	Sintering stress
γ	Surface energy or face-centered cubic phase
η	Viscosity or Ni_4W intermetallic phase
ε	Co solid solution
μ	Co_7W_6 intermetallic phase

δ	NiW intermetallic phase
α	W terminal solid solution phase
π	NiW$_2$ intermetallic phase

Abbreviations

μm	Micrometer
MPa	Mega Pascal
nm	Nanometer
rpm	Rounds per minute
wt.%	Weight percent

Acronyms

AGS	Average Grain Size
AS	Activated Sintering
APT	Ammonium Paratungstate
BCC	Body-centered Cubic
BEI	Back-Scattered Electron Imaging
CEP	Calcium Evaporation Process
DC	Direct Current
EDS	Energy Dispersive Spectroscope
FCC	Face-centered Cubic
FFCCP	Fray-Farthing-Chen Cambridge Process
GSD	Grain Size Distribution
HCP	Hexagonal Closed Packed
HRA	Rockwell A Hardness
HV	Hardness Vickers
LPS	Liquid Phase Sintering
MSE	Moten Salt Electrolysis
MTU	One Hundredth of a Metric Ton of 1.000 Kilograms
OM	Optical Microscope
PM	Powder Metallurgy
RHL	Rhombohedral Lattice
SEI	Secondary Electron Imaging
SEM	Scanning Electron Microscope
SSS	Solid State Sintering

UHP	Ultrasonic Homogenization Process
XRD	X-Ray Diffraction
XRF	X-Ray Fluorescence
W	Commercially Available Tungsten Powder (Alfa Aesar 10400)
W*	Electrochemically Produced Tungsten Powder (Treated)
W**	Electrochemically Produced Tungsten Powder (Untreated)
WHAs	Tungsten Heavy Alloys
W*HAs	Electrochemically Produced Tungsten Employed Heavy Alloys

LIST OF TABLES

LIST OF FIGURES

xvii

xviii

CHAPTER 1

INTRODUCTION

Production of metal powder by employing molten salt processes can be preferred where pyrometallurgical reduction and hydrometallurgical methods are impossible or not feasible. Although metal production in molten salts is an old process, its significance has increased in recent years due to development of a novel process, Fray-Farthing-Chen Cambridge process (FFCCP) [1]. The process enables direct reduction of metal oxides, sulphides, carbides and nitrides to elemental metal powders or alloys of desired composition [2-3]. Due to its high oxygen dissolving capacity, molten calcium chloride is usually used as the electrolyte [1]. The process has a great importance especially for refractory metal powder production, because it offers lower processing steps and temperatures compared to conventional fabrication methods.

In addition, Erdoğan and Karakaya recently reported that elemental tungsten (W) powder can be obtained by modified FFCCP. In the process $CaWO_4$ is used as the starting material and reduced directly to metallic tungsten at 600 °C. Molten calcium chloride ($CaCl_2$) and sodium chloride (NaCl) mixture at eutectic composition is used as the electrolyte [4–6].

In this chapter, firstly brief explanations about W sources, applications and fabrication methods will be given. Secondly, application areas of tungsten heavy alloys and their sintering behaviors will be indicated together with a literature review of related works. Then, details of conducted experiments and characterization techniques will be given in Chapter 2. The results of experiments and investigated properties such as sintered mechanical, physical and microstructural characteristics will be presented and discussed in Chapter 3. Finally, the conclusions and future implications about the study will be given in Chapter 4. Additionally, all the other results about conducted experiments which were not given in Chapter 3, can be found in Appendices.

1.1 The Elemental Tungsten

Tungsten (W) is a well-known and valuable refractory metal. Owing to its excellent properties, it is added the strategic metal group. It is a good candidate for many specific engineering systems where high density and high strength at high temperatures are desired. Some of the general properties of tungsten are given in Table 1.1.

Table 1.1 Some of the crucial properties of tungsten [7].

Properties	Value
Atomic number	74
Atomic weight	183.84
Electron configuration	$\{Xe\}\ 4f^{14}\ 5d^4\ 6s^2$
Crystal structure	Body-centered cubic (BCC) A2
Density	19.25 g/cm^3
Melting point	3422±15 °C
Boiling point	5700±200 °C
Coefficient of thermal expansion	4.32-4.68x10^{-6}.K^{-1} (298 K)
Electrical resistivity	5.28 $\mu\Omega$.cm
Thermal conductivity coefficient	1.75.W.cm^{-1}.K^{-1} (298 K)
Modulus of elasticity	390-410 GPa (298 K)
Hardness	300-650 HV30

Tungsten products are manufactured by powder metallurgy (PM) process due to fabrication difficulties with conventional production methods. They are typically originated from high melting temperature and brittle characteristics of metallic tungsten. However, even when PM is used, it is still a challenging task to sinter elemental tungsten because of the high temperature and reducing atmosphere requirements. The sintering temperatures can be lowered by mixing tungsten with transition metals like Ni, Co, Fe and Cu. By this way, sintering temperatures can be lowered and ductility of the end product can be increased while significant properties such as low thermal expansion, good electrical and thermal conductivity and high wear and corrosion resistance are preserved to some extent.

1.1.1 Sources, Prices and Application Areas [8]

The requirement of tungsten can be supplied from primary and secondary sources. The ore concentrates must contain at least 0.3 and 1 % WO_3 to obtain economic profit depending on impurity types and contents. There are lots of tungsten minerals in the earth's crust, but only four types are employed for elemental tungsten production. They

are scheelite ($CaWO_4$), ferberite ($FeWO_4$), hübnerite ($MnWO_4$) and wolframite ((Fe,Mn)WO_4). Although last three minerals are widely used in extraction processes, scheelite is the most important raw mineral due to possessing highest WO_3 content, 80.6, and being the most common tungsten mineral in all over the world.

China has approximately 60 wt.% tungsten reserve of all the world, whereas the other major tungsten mineral suppliers such as Canada, Russia and USA have totally 22 wt.% tungsten reserve [9].

Türkiye has approximately 1.5% of total tungsten ore reserves. Nearly the all reserve of Türkiye is located in Uludağ/Bursa, which has higher than 0.4 wt.% WO_3 containing scheelite deposit. The estimated tungsten reserve of Uludağ is nearly 14 million tons of ore, in other words, 50 thousand tons of elemental W [10].

When it comes to secondary sources, they are as important as the commercial tungsten minerals due to containing high amount of tungsten. They are supplied from WC hard cements, tungsten heavy alloys (WHAs) containing between 90 wt.% and 98 wt.% W, and pure form applications. When the total tungsten reserve, 1-1.5 ppm, in the earth's crust is considered, it is thought that the amount of recycled tungsten from its scrap will be increased day by day.

Recent price fluctuations of tungsten is illustrated in Figure 1.1. As can be seen in the figure, the prices of ammonium paratungstate (APT), given in per mtu, demonstrated sharp increases and approximately reached 460 \$/per mtu in 2011 due to limited tungsten exportation from Republic of China. Per metric ton unit ("MTU" - one hundredth of a metric ton of 1.000 kilograms) represents the 10 kilograms of tungsten trioxide (WO_3) and/or 7.93 kilograms of pure tungsten. The prices has shown slight alternation between 200 and 250 \$ recently.

Currently, the biggest tungsten supplier and consumer is Republic of China and it is predicted that China will maintain dominating the global tungsten price and market in near future.
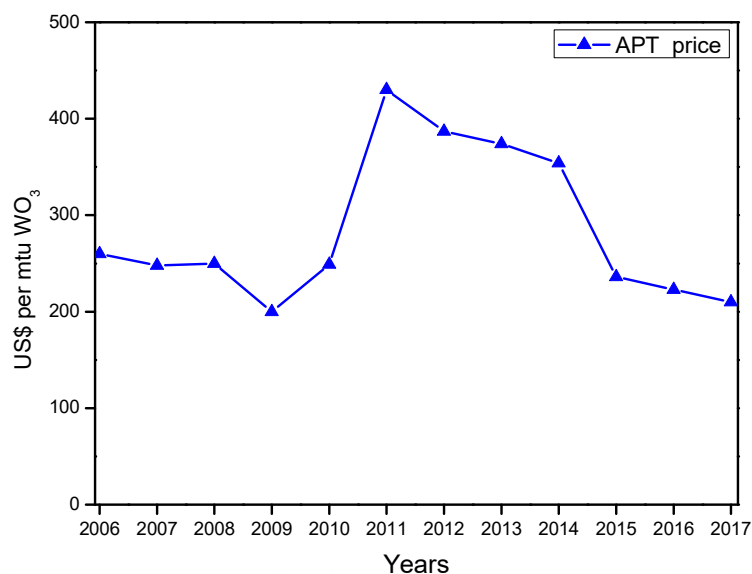
Figure 1.1 Ammonium paratungstate (APT) price fluctuations over the past decade [11].

Owing to its unique properties such as high melting point and density, tungsten and its compounds are widely used in many technological applications. These properties are mainly attributed to its half-filled 5d electron shells. The major usage areas of tungsten are given in

Figure **1.2**. They can be collected under four main application areas: hard metals, alloying elements in steel and/or base metal in tungsten heavy alloys, mill products, chemicals and other special applications.
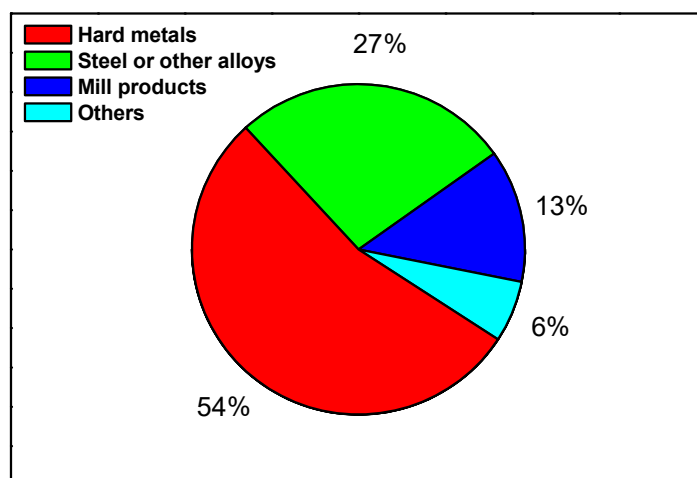
Figure 1.2 Tungsten application areas [12].

1.1.2 Industrial Tungsten Production

Industrial production of elemental tungsten powder generally begins with producing an intermediate product, ammonium paratungstate (APT, $(NH_4)_{10}(H_2W_{12}O_{42}).4H_2O$), but a series of hydrometallurgical treatments is required to obtain APT.

First of all, the expected 60-75 wt.% WO_3 concentration must be obtained from commercially valuable tungsten minerals. Both scheelite and wolframite ores can be enriched by flotation. Wolframite ores are sometimes enriched by magnetic separators thanks to its weakly magnetic structure. However, most of time, grinding and gravity separation are sufficient to provide the desired enrichment [13].

The prepared concentrates are then subjected to a leaching treatment to obtain APT. Sodium hydroxide (NaOH) solutions are used for $(Fe,Mn)WO_4$, whereas sodium carbonate (Na_2CO_3) is used for $CaWO_4$ [14].

Finally, APT is reduced to tungsten oxides at 400-900 °C in air or slightly reducing atmosphere which is provided by hydrogen or hydrogen and nitrogen gas mixture [8].

The second reduction process is performed under streaming hydrogen atmosphere between 600 and 1100 °C to obtain elemental tungsten powder [8]. The production steps of metallic tungsten powder from APT are given in Figure 1.3. Furthermore, the reduction reaction of tungsten trioxide is given in Eq. 1.1. The produced tungsten powder can be used in various forms such as, WC, WHAs, alloying elements for steel and other suitable materials, etc.

$$WO_{3(s)} + 3H_{2(g)} = W_{(s)} + 3H_2O_{(g)} \tag{1.1}$$

The current tungsten production method has some disadvantages that results from the following conditions:

a. Necessity of continuous external heat supply.
b. Difficulties of working with hydrogen atmosphere.
c. Relatively low driving forces at reduction, since W-WO_3 line is slightly above the H_2-H_2O line in the corresponding Ellingham diagram, which is provided in Figure 1.4 [15].
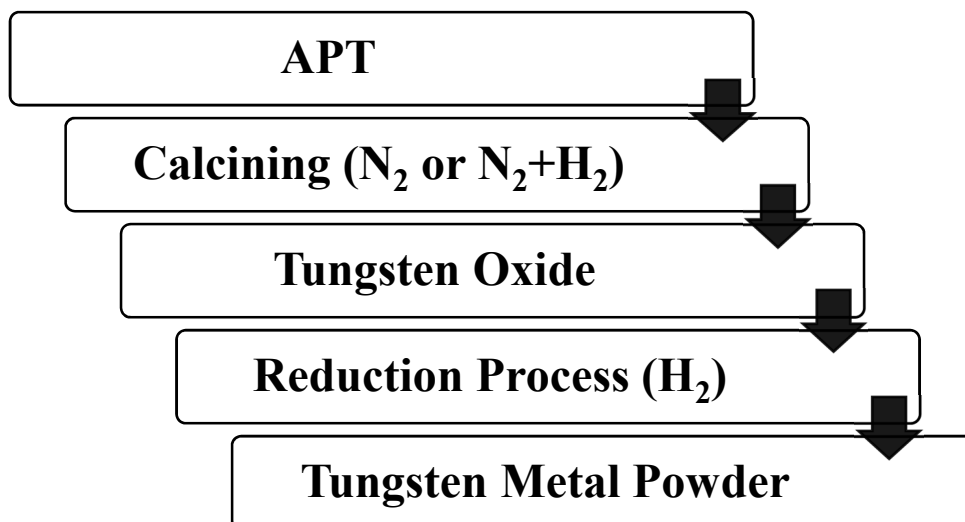
Figure 1.3 Elemental tungsten powder production from APT.

1.1.3 Electrochemical Reduction of Tungsten Compounds

Production of low melting point metals by molten salt electrolysis has been employed for more than ten decades. The molten metals are typically collected from the bottom of the reactors in liquid state or from the top as in the case of magnesium. However, high melting point metals could not be easily produced via this method due to production limitations.
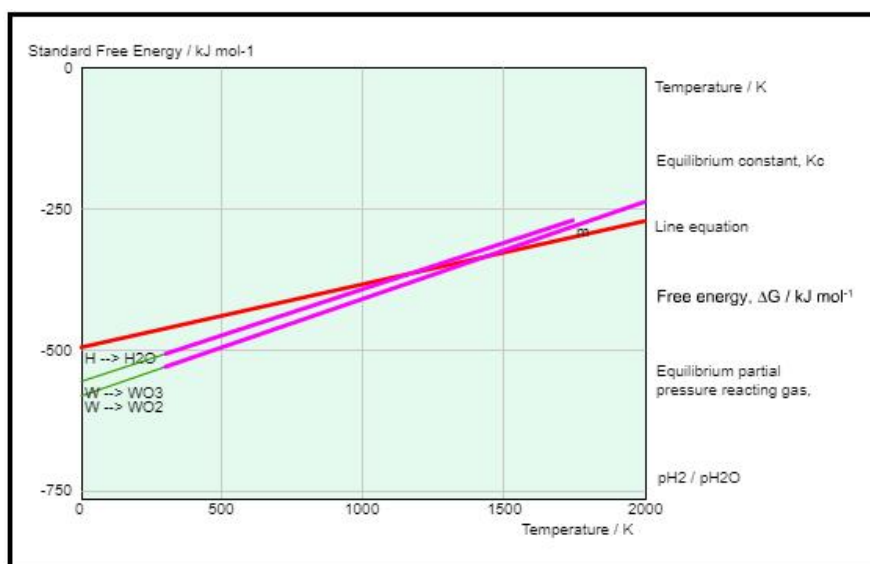
Figure 1.4 Ellingham diagram for W-WO$_2$ / W-WO$_3$ and H$_2$-H$_2$O systems
(Reproduced from [16]).

Although they can be reduced in solid state, but the process causes dendritic shape formation. Dendrites can cause short-circuiting of the electrodes and they also have high tendency to oxidation. Furthermore, the reduced materials should be scraped off from the cathode surface [17].

An alternative production method, electrodeoxidation, was announced recently which provides metal oxide reduction in molten salt solutions [1]. The process is based on the removal of oxygen from the metal oxide using a certain potential which is lower than the decomposition potentials of the salts compromising the electrolyte. The graphite rod is used as the anode, whereas metal oxide pellet is used as the cathode. The reactions take place in molten salt media, containing $CaCl_2$. The cathodic and anodic reaction are given in Eq. 1.2 and Eq. 1.3, respectively.

$$M_xO_y + 2\ ye^- = xM + yO^{2-}\ \text{(Cathodic)} \tag{1.2}$$

$$yO^{2-} + yC = yCO + 2ye^-\ \text{(Anodic)} \tag{1.3}$$

Many metals including Ti [18] and Cr [19] were produced in laboratory scale experiments by the electrodeoxidation process. However, the process is not suitable for WO_3 deoxidation due to formation of tungsten oxychloride (WO_2Cl_2) which is a gaseous species at the reaction temperature, thus, W losses are inevitable [3,17]. Erdoğan and Karakaya announced a modified FFCCP to produce W powder using $CaWO_4$ instead of WO_3 as the initial material [4-6,17]. The powder obtained by this process is named as "electrochemically produced tungsten" in this thesis.

The schematic appearance of experimental set up is given in Figure 1.5. By this setup, scheelite ($CaWO_4$) was reduced to elemental W powder in eutectic $CaCl_2$-NaCl electrolyte [17, 20]. The treatment was performed at 600 °C under Ar gas flow and a direct current (DC) supplier was used to provide potential differences higher than 2.5 V [17]. The produced tungsten powder was cleaned with dilute HCl solution to remove the Ca containing byproducts [17]. Furthermore, using pulse current in elemental W powder production has been studied recently [21]. In this thesis, the powder obtained from the study [21] was used for designed sintering experiments and the results will be discussed in Chapter 3.
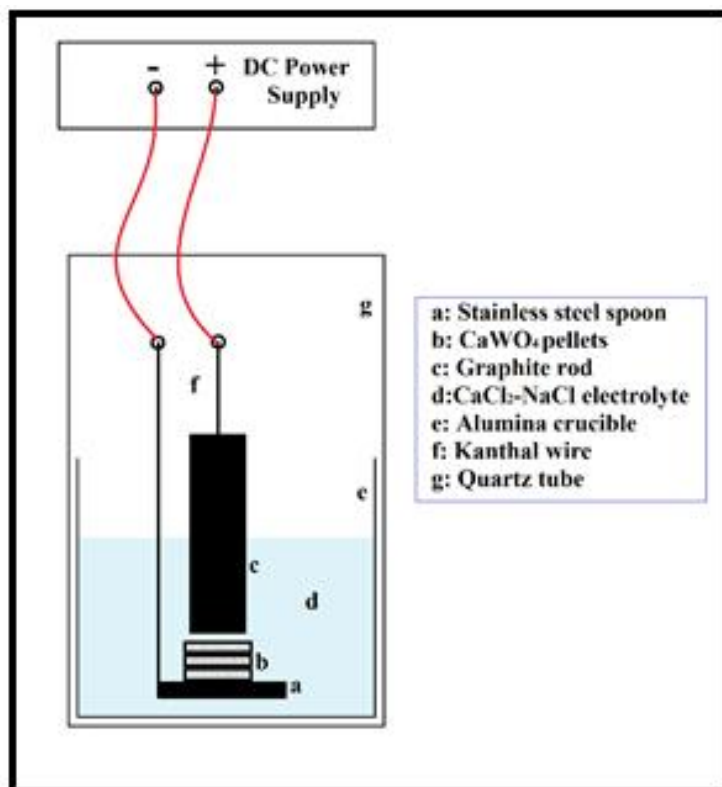
Figure 1.5 The experimental setup of electrochemical reduction process [22].

1.2 Processing of W Based Heavy Alloys

Pure W applications are not widely used due to production limitations and brittle nature of tungsten. Although heavy alloys form of tungsten can be produced using several methods such as electron beam melting, arc casting, hot extrusion, etc., powder metallurgy process (PM) is mostly preferred method.

1.2.1 Powder Metallurgy

Powder metallurgy (PM) is a heat treatment method, which consist of shaping and consolidation stages and applied to obtain near net shape products. It is mostly used for complex and small size parts. Furthermore, it is also used in cases where conventional fabrication methods are not feasible.

PM process involves three main investigation and/or fabrication steps; initial powder characteristics, processing variables and final product properties. The details of these steps are given in Figure 1.6.

Powder   **Processing**   **Properties**

-Microstructure	-Press	-Density
-Chemistry/Purity	-Roll	-Ductility
-Friction	-Extrude	-Magnetic
-Size	-Sinter	-Strength
-Shape	-Forge	-Conductivity
-Fabrication method	-Hot press	-Microstructure
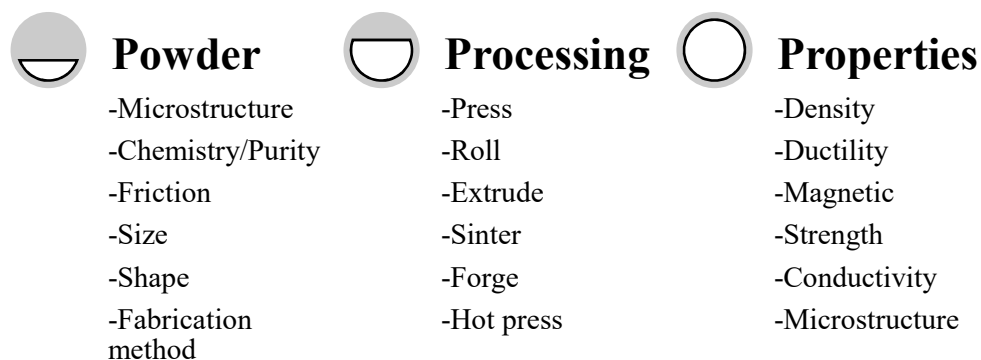
Figure 1.6 Powder metallurgy flow chart [23].

Powder mixing, powder compaction and sintering are the steps of PM process, which are applied to obtain the densified final products. The details and aim of these steps are given in the following titles.

1.2.2 Powder Blending and Mixing

The powder mixing step plays a crucial role to obtain homogenously mixed powders. Insufficiently mixed powders lead to wide compositional differences in prepared products. This has negative influences on the mechanical properties of final products [24].

During mixing and blending, lubricant addition and/or, mechanically alloying with high-energy ball milling can be applied where needed for specific PM processes.

Initial powder characteristics and mixing variables should be well-characterized and calculated. The variables such as mixer type, determination of critical mixing speed to obtain optimum milling performance, amount of powders and employed median, container size and shape, mixing time are as important as like employed powders to achieve homogeneous mixing [24]. Turbula mixer, attritor mill, ball mill, etc. can be used for powder mixing and/or mechanical alloying processes.

1.2.3 Powder Compaction

Before the sintering treatment, powder mixture should be compressed to obtain desired shape and denser structure. The shaping procedure is generally conducted using die compaction or cold isostatic pressing.

Furthermore, compression and sintering treatment can be performed at the same time by employing hot isostatic pressing.

The amount of porosity, porosity distribution, density variation and relative density of green compact are crucial parameters for sintering treatments. Therefore, the applied compression method, pressure and time should be investigated thoroughly.

Owing to suitable compression method and pressure, desired packing homogeneity and compacted powders are obtained. The relative green density and porosity distribution are important parameters for grain growth retardation and pore motion during sintering. Heterogeneously distributed pores may cause entrapped big pores formation in product which results in insufficiently densified structures and decreased mechanical properties. Densities and powder characteristics of compacted specimens demonstrate a great variation with applied compaction pressure. The relation is illustrated in Figure 1.7.
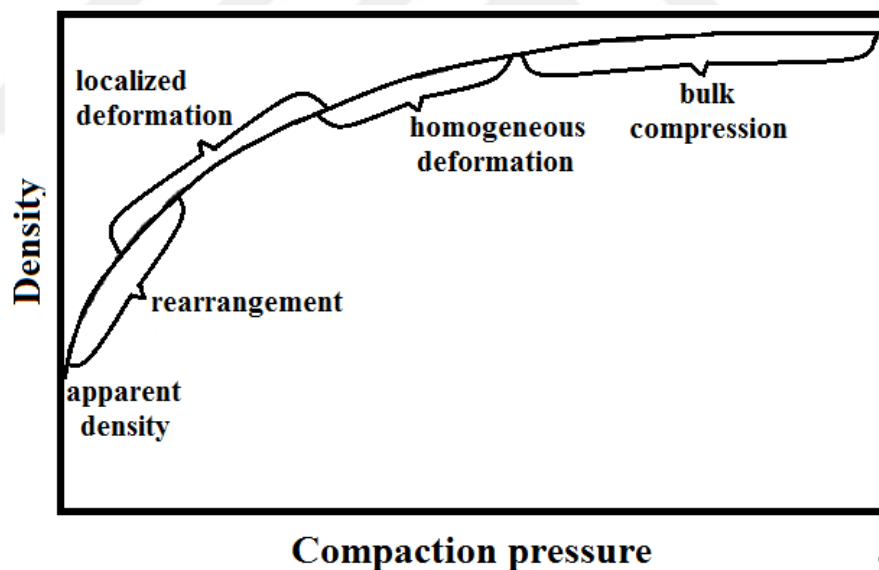
Figure 1.7 Density and compression process relation [23].

As can be seen in Figure 1.7, as the applied pressure increased, the density values of the pure and/or mixed powders also increase up to densification limit where entrapped pores may not be further compressed and thrown out. Relatively ductile powders such as metal powders can be deformed and considerably densified during compression, whereas brittle powders like alumina (Al_2O_3) cannot be easily compressed and mostly

fragmented during compression procedure. The hard and brittle powders are generally covered with a binder additive to enhance compression behavior and strength of green specimens.

Sintering is a diffusion controlled process; thus, the distance between the powders is an important parameter during sintering. Higher than 60 % relative density of green compact is typically sufficient to reach fully densified structure or at least higher than 95 % relative density. However, excessive relative density of compressed specimens sometimes negatively affects densification behavior of compact during sintering. Some of the suitable cold isostatic pressure ranges for selected materials are given in Table 1.2.

Table 1.2 Suitable pressure ranges for cold isostatic pressing [25].

Powder material	Pressure range (MPa)
Iron	311-414
Copper	138-276
Aluminum	55-138
Stainless steel	311-414
Lead	138-207
Titanium	310-415
Tungsten	240-415
Tungsten carbide	138-207

1.2.4 Sintering and Post Sintering Treatment

Sintering is an important forming processes, which provides interconnected solid particles and hence increases the strength of compressed green compacts by means of a sufficient sintering temperature. The solid skeleton occurs above homologous temperatures of about 0.5-0.75 T_m (melting temperature) by an atomic level mass transportation. Directions and rates of diffusional processes of mass transfer can be controlled by the system characteristics such as thermodynamic driving forces and kinetic parameters. The first mainly determines the way of process, while the second includes a series of interior and exterior complex parameters like magnitudes of kinetic coefficients, diffusion coefficient and realization of different mass transfer mechanisms.

Brittle nature of some materials, which causes difficulties during shaping via traditional production methods, inevitably causes employment of sintering processes. The consolidation method is generally divided two; pressureless and pressure assisted sintering. The pressureless sintering processes like solid state sintering (SSS), activated sintering (AS) and liquid phase sintering (LPS) will be explained here due to having wide application areas [24].

Solid state sintering is a thermal consolidation method which leads to formation of solid bonding between the small solid particles. The process is mostly used for ceramic powders sintering to control the sintered grain size. The applied sintering temperatures are between 0.5 and 0.7 of absolute melting point. During treatment, total energy of compacted specimens is decreased by two main mechanisms; elimination of free surface areas and formation of bigger particles/grains. The mechanisms generate driving forces for specimens to form denser structures by decreasing total system energy [24].

SSS is consisted of three main stages; initial stage, intermediate stage and final stage. The changes that take place during these stages are briefly given in Table 1.3.

Table 1.3 Solid state sintering stages for monosize spheres [24].

Variables	Initial stage	Intermediate stage	Final stage
Neck size ratio, X/D	< 0.33	0.33 to 0.5	> 0.5
Coordination, N_C	< 7	8 to 12	12 to 14
Density, %	60 to 66	66 to 92	> 92
Shrinkage, $\Delta L/L_O$ %	< 3	3 to 13	> 13
Surface area, S/S_O %	100 to 50	50 to 10	< 10
Grain size ratio, G/D	≈1	> 1	>> 1
Pore size ratio, d/G	< 0.2	Near constant	Shrinking

Where X is the neck diameter, D is the particle diameter, N_C is the coordination number, G is the grain size, G_O is the initial grain size and d is the pore diameter.

During the initial stage, necking between the particles forms and begins to grow. The formed neck causes approximately 50 % loss of surface area but the increase in relative density is slight.

At the intermediate stage, the pores the between the particles become rounded and elongated shape. Total open pores nearly disappear. Density of specimen may reach higher than 90 % relative density. On the other hand, coarsening tendency of grains and pores start at the later phases of this intermediate stage.

During the final stage, further surface area reductions are relatively negligible and the densification rate is slower. The closed pore formation and grain growth rate are faster than intermediate stage due to elimination of open pores which are more efficient in grain growth retardation [24].

The microstructure and relative density variation of sintered specimens are illustrated in Figure 1.8 and Figure 1.9, respectively.
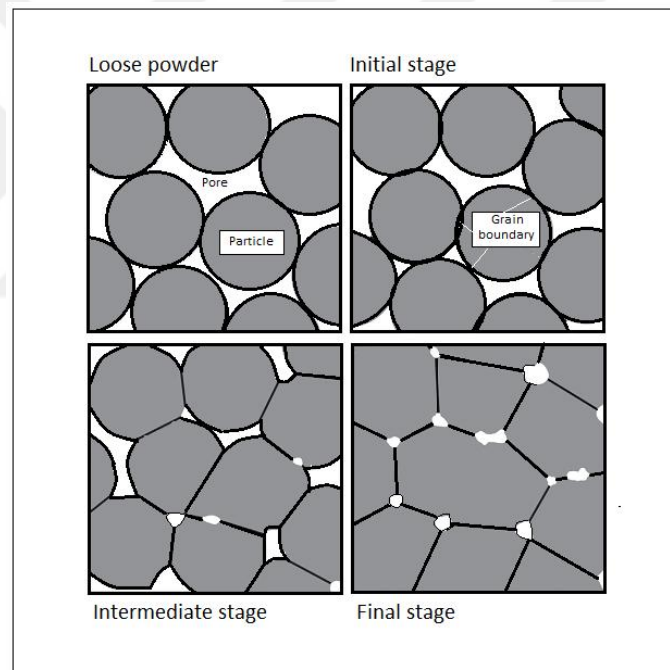
Figure 1.8 Schematic representation of particles to grains transformation during solid state sintering [24].

Mass transport mechanism in sintering is the main reason for densification, but all transport mechanisms do not provide densification. Bulk transport mechanism leads to densification, whereas surface transport mechanism does not result in densification due to surface to surface mass transport.
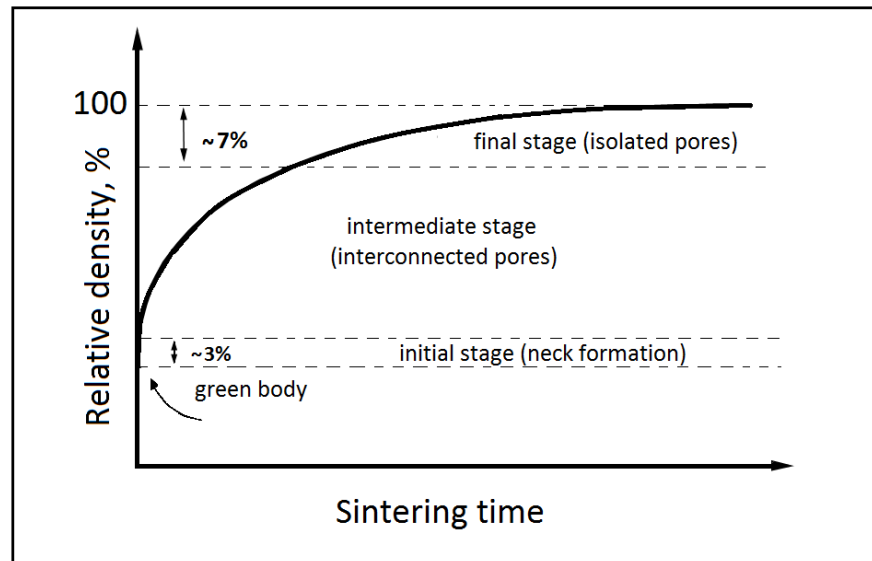
Figure 1.9 Sintering stages vs. relative density [26].

However, interior to surface mass transport occurs during the first mechanism. The mechanism types, mass source-sink places and related parameters are given in Table 1.4.

Table 1.4 Material transport mechanisms during solid state sintering [26].

Material transport mechanism	Material source	Material sink	Related parameter
Lattice diffusion	Grain boundary	Neck	Lattice diffusivity, D_l
Grain boundary diffusion	Grain boundary	Neck	Grain boundary diffusivity, D_b
Viscous flow	Bulk grain	Neck	Viscosity, η
Surface diffusion	Grain surface	Neck	Surface diffusivity, D_s
Lattice diffusion	Grain surface	Neck	Lattice diffusivity, D_l
Gas phase transport -Evaporation / Condensation -Gas diffusion	Grain surface Grain surface	Neck Neck	Vapor pressure difference, Δ_p Gas diffusivity, D_g

The schematic appearance of material transport mechanisms is given in Figure 1.10. Surface transport mechanism is generally dominant during initial and intermediate stages of sintering, whereas bulk transport mechanism is the determinative transport
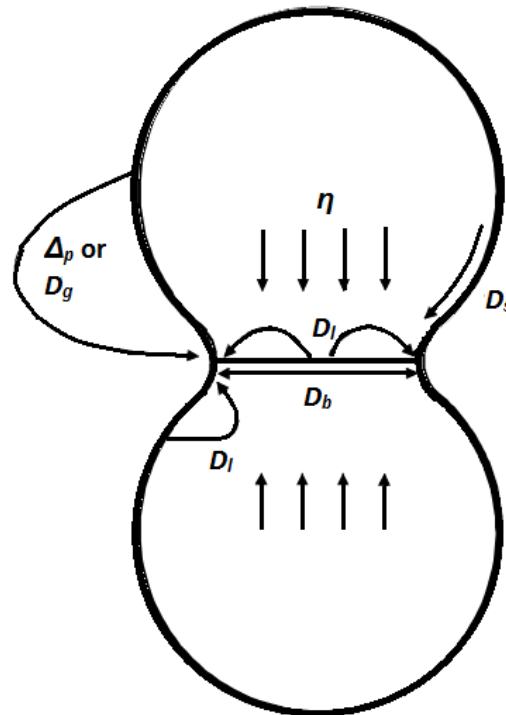
Figure 1.10 Material transport mechanisms [26].

type during final stage. The transport mechanism, which occurs from interior to surface, brings about the densification and shrinkage during sintering as mentioned earlier [26].

On the other hand, two different phenomena also play a crucial role in solid state sintering. The first phenomenon is the mass transport from convex surface under compression stress, to concave surface under tension stress. Filled mass from convex to concave provides a flattened surface, which has relatively low surface energy owing to decreased free surfaces. The schematic appearance of surface flattening mechanism is demonstrated in Figure 1.11.

The second phenomenon is preferentially mass transport from small particles to relatively big particles. The smaller particles have higher curvature than bigger particles. When the relation between the sintering stress (σ) and surface energy (γ) is considered, the sintering stress of the system increases as the particle radius decreases.
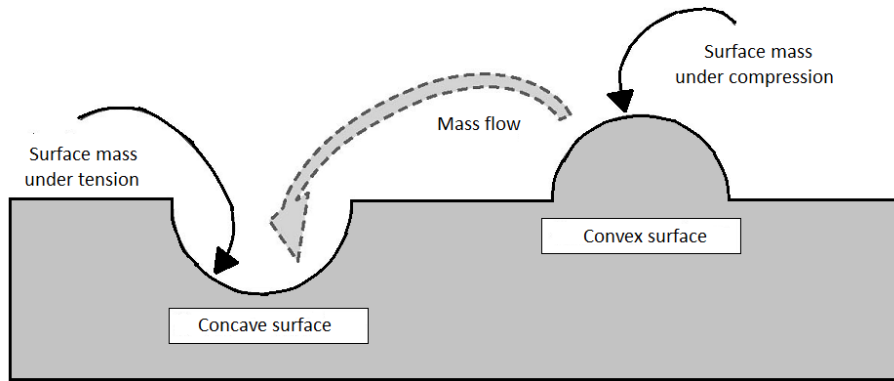
Figure 1.11 Surface flattening mechanism at concave and convex surfaces [27].

On the other hand, time, temperature, shape and size of particles are also important variables during solid state sintering. Temperature and particle size have a great influence on sintering rate. The related Arrhenius equation is given in Eq. 1.4.

$$D = D_0 e^{\frac{-Q}{RT}}$$ (1.4)

Where D is the diffusion coefficient, D_0 is the pre-exponential factor, Q is the activation energy, R is the gas constant, T is the absolute temperature.

For example, suitable solid state sintering temperature for a W product is approximately reach 2200 °C when the 0.5-0.7 (T_m) of absolute melting point is considered. The sintering temperatures can be provided by special sintering furnaces under controlled atmosphere, but the production costs are much higher. The temperature can be decreased via relatively small particle size (at nanoscale) and a long dwell time. By this way, the sintering temperature of pure tungsten compact may be decreased down to 1800 °C [27].

Adding small amounts of transition metals can decrease the temperature required for solid state sintering of tungsten. They enhance the densification rate and contribute obtaining a denser structure at a relatively lower sintering temperature and time compared to SSS processes. In this sintering method, which is called as activated sintering, liquid phase is not formed and the temperature should be adjusted carefully.

The additives have high diffusion coefficients at activated sintering temperatures for tungsten. High melting point metals should be dissolved in additive metals to obtain enhanced mass transport between base particles. Related phase diagram of high melting point material and activator metal or metals should have the properties which is illustrated in Figure 1.12.
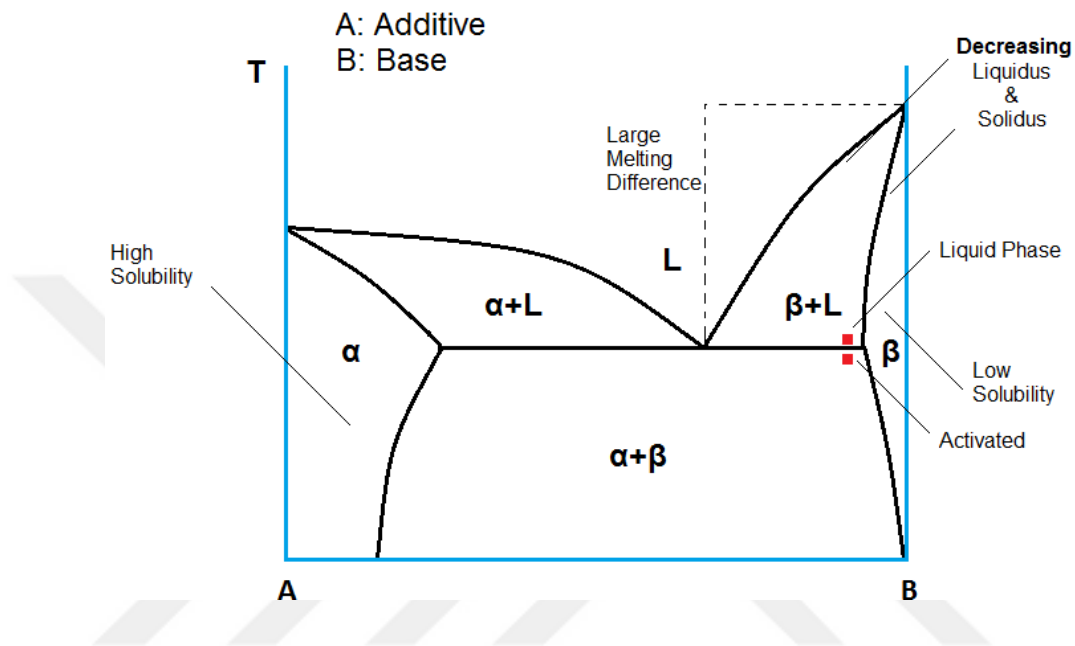
Figure 1.12 Suitable phase diagram for activated sintering [28].

On the other hand, the solubility of high melting point material in activator metals is a crucial parameter. Shrinkage performance of various transition metals added tungsten is demonstrated in Figure 1.13.

As illustrated in Figure 1.13, the amount of dissolved tungsten in activator elements affects the shrinkage behavior of mixed compact. Valence of additive metals play a crucial role in activated sintering. Cu cannot dissolve W in its structure, so W-Cu mixture indicate nearly the same shrinkage behavior as elemental tungsten. On the other hand, Pd, Pt and Ni, which are in the same group of the periodic table, cause a significant change on shrinkage behavior of tungsten specimens. make a significant contribution on shrinkage behavior of additive added tungsten specimens.
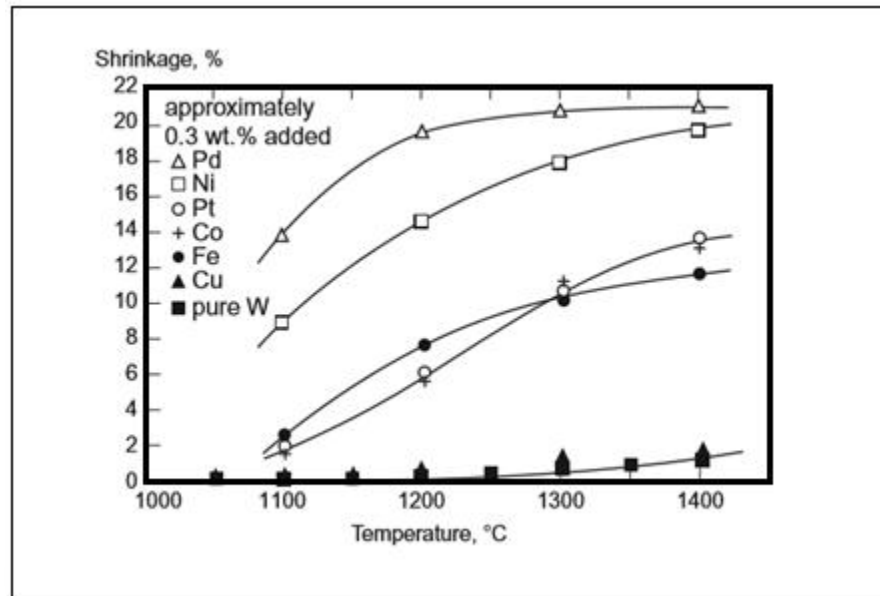
Figure 1.13 Transition metals effects on W compact shrinkage with altered
sintering temperature [24].

The effects of first transition metal series (from Cr to Zn) on shrinkage and activation
energy are illustrated in Figure 1.14.
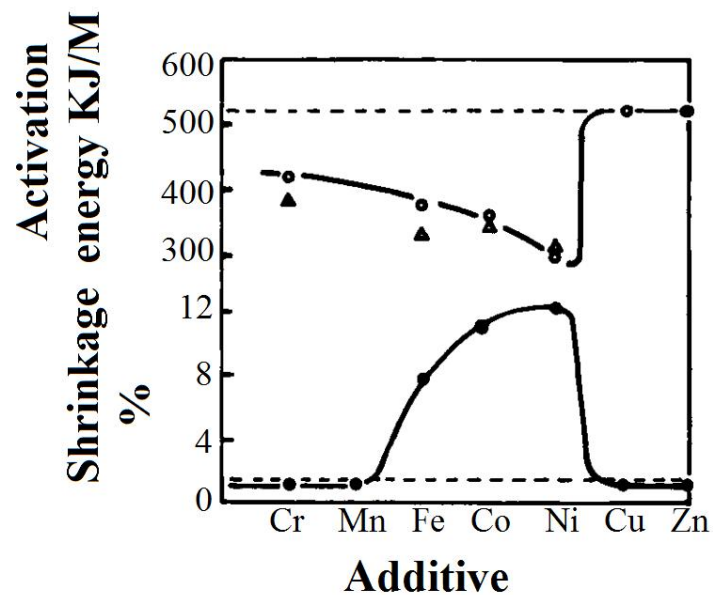
Figure 1.14 The effect of first transition metal series on shrinkage and activation
energy [28].

As can be seen in Figure 1.14, as the required activation energy decreases, the densification behavior of the compact increases. Ni is most effective transition metal in this studied group.

Liquid phase sintering (LPS) is a widely used consolidation method for refractory metals and ceramic powders sintering. Formation of liquid path between the particles enhances the densification rate via providing more effective transportation region. Therefore, densification rate of SSS and AS is relatively lower than LPS.

Wetting ability and solubility relations between base material and additive(s) are important parameters to prepare suitable mixed compacts. Additives should have high solubility and good wetting ability for the base material, whereas the base material should have very low or no solubility for the additives in its structure to obtain more densified mixed compacts. LPS process consists of four stages; which are solid state sintering, rearrangement, solution-reprecipitation stage and solid phase sintering stages. Region of each steps and the effects on density are demonstrated in Figure 1.15.
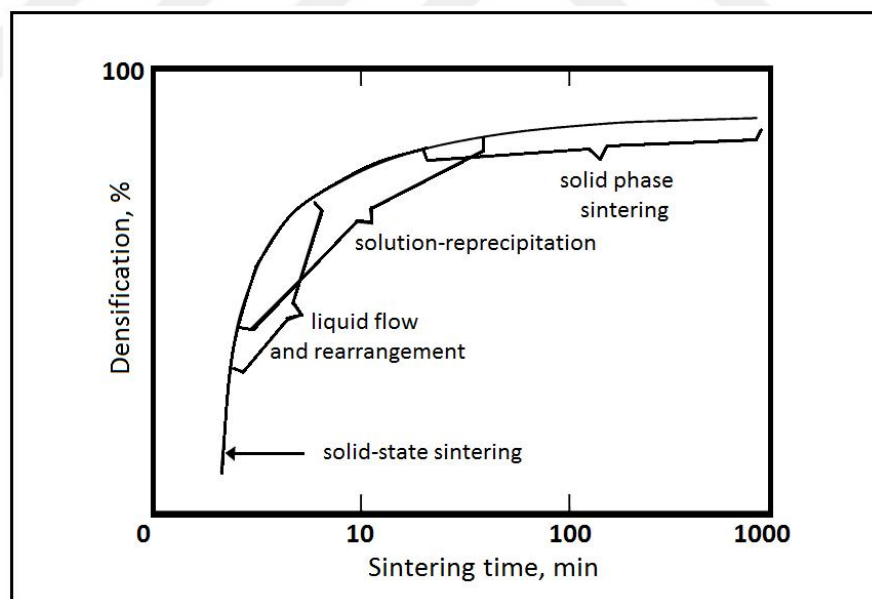
Figure 1.15 Stages of liquid phase sintering process [29].

As can be seen in Figure 1.15, the rate of densification is higher at early stages owing to chemical gradients between the mixed base material and additive(s). When the liquid phase forms, the solid particles rearranged which leads to more dense and

regular particle distribution. Relatively smaller particles, which have higher energies than coarse particles, are preferentially dissolved in liquid to decrease the total system energy. The dissolved atoms move and reprecipitate on the relatively coarser particle surfaces. The mechanism is called as Ostwald ripening theory.

Amount of additive(s) is an important parameter for LPS process. Densification value and shape of sintered grains are considerably controlled via amount of the liquid volume and distance between the grains [24].

Low liquid volume fraction leads to rather flat surface between the grains. This leads to better annihilation of pores between the grains, which relies on the grain packing [24].

Moderate liquid volume fraction results in formation of rounded grains. As the liquid volume increased, the shape of grains becomes more spheroidal [24].

High liquid volume fraction causes large distances between the particles (grains) and formation of solid-solid contact between neighboring grains at the same time. As the liquid volume increased, the shape of grains may transform to prismatic grain structure [24].

The density variation with volume of liquid phase is illustrated in Figure 1.16.
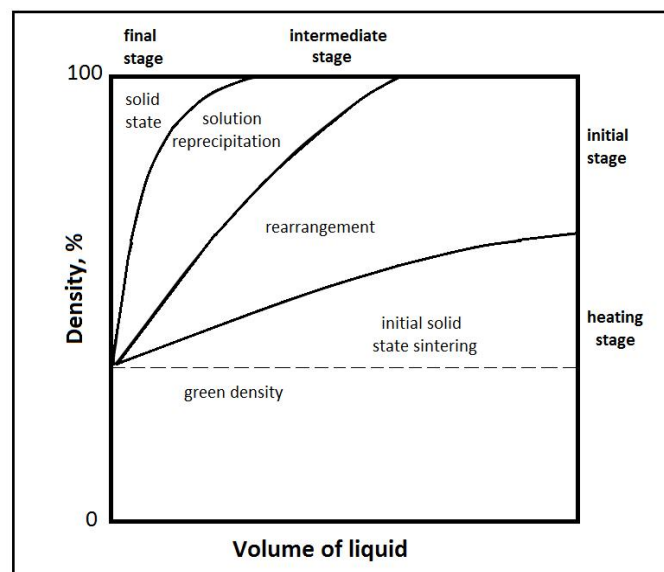
Figure 1.16 Volume of liquid and densification relation [29].

As can be seen in Figure 1.16, the volume of liquid phases has a great influence on LPS stages. As the amount of employed additive(s) increased, the fully densified structure can be obtained in initial stage of LPS process. In addition, densification rate, grains shape and coarsening behavior are also controlled via volume fraction of binder phase. On the other hand, as the volume of liquid decreased, the densification process is needs solution and reprecipitation mechanism and solid state sintering to reach fully densified structure [29].

W-Cu alloys can be given as an example for densification and volume of additive relation. Elemental Cu addition to W powder does not provide a remarkable enhancement in densification of tungsten as mentioned earlier. However, when Cu has a higher volume fraction (i.e. liquid phase), W compact can be densified at relatively lower sintering temperatures by means of rearrangement mechanism. The melted Cu rearranges the W particles, and hence more homogeneous and densely packed distribution can be obtained. Densification behavior of 32 wt.% Cu contained W-Cu alloys is illustrated in Figure 1.17.
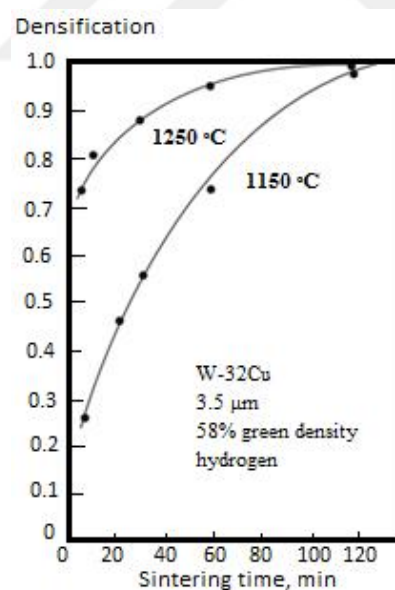
Figure 1.17 The effect of sintering temperature on W-32Cu densification [24].

As illustrated in Figure 1.17, even though Cu cannot dissolve W in its structure, rearrangement of W particles in liquid phase is sufficient to obtain fully densified structure.

During LPS process, the sharp corners of base materials are preferentially dissolved by liquid phase, thus flat surfaces between the grains are obtained. Furthermore, solution and reprecipitation mechanism takes place between small and big particles. Both mechanisms decrease the total energy of the compacted powders. The schematic representations of contact flattening and Ostwald ripening procedure are illustrated in Figure 1.18.
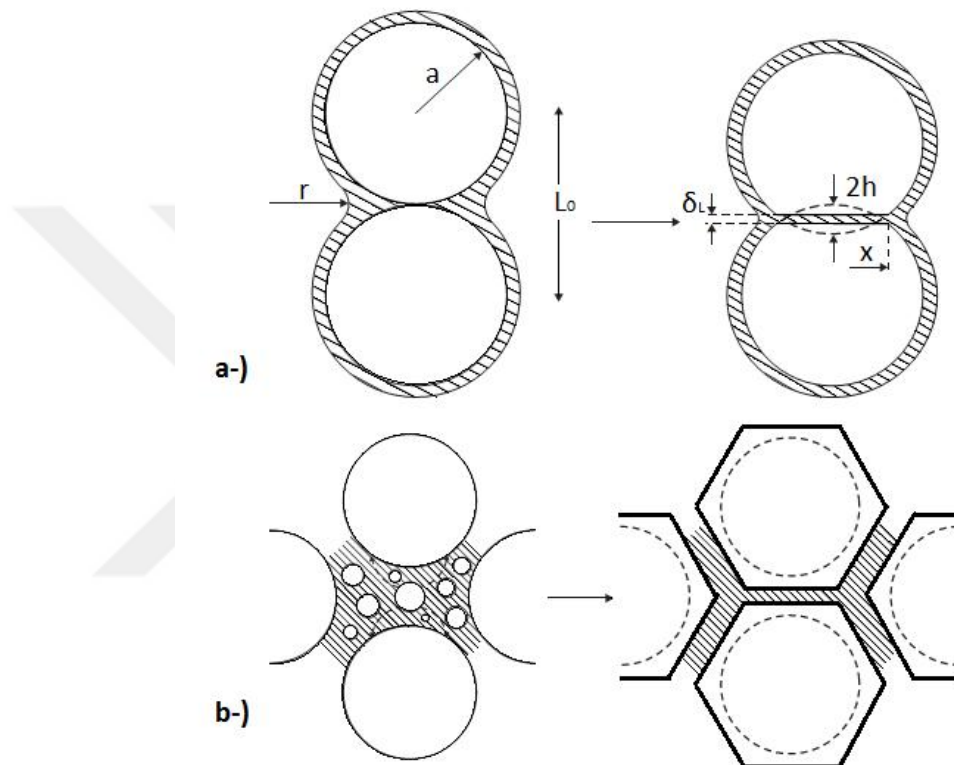
Figure 1.18 (a) Contact flattening and (b) Ostwald ripening mechanism during LPS process [27].

Accommodated grains start to coarsen in late of intermediate and final stages of LPS which enhances the density of compacted specimens. Vacuumed or low weight gas atmosphere should be employed to decrease the amounts of entrapped pores at solid state sintering stage of LPS.

The final grain sizes of sintered specimens are predicted via using in Eq. 1.5.

$$G^n = G_0^n + Kt \tag{1.5}$$

Where G_0 is the initial grain size, G is the fired grain size after LPS, K is the growth rate constant, t is the dwell time of sintering, n is a kinetic factor which varies between 2 to 4 and mostly taken as 3 for diffusion controlled coarsening processes.

LPS process provides many advantages for sintering of high melting point materials such as low sintering temperature and more densified structure after sintering. However, it has some disadvantages including uncontrolled and unpredictable interactions between base and additive metals, and excessive grain coarsening. They are generally resulted from accelerated mass transport rate in liquid. However, most of the hard materials are inevitably fabricated via LPS to obtain rapid densification and eliminate the shaping difficulties.

Contact angle (wetting angle) and dihedral angle are two crucial parameters for sintering applications. The contact angle is measured where solid, liquid and gas phases are present at the same time. Dihedral angle determines the grain boundary structure of fired specimens and measured via grain boundary energy intersecting a liquid phase for LPS processes or vapor phase for SSS processes. The schematic representations of both parameters are given in Figure 1.19.
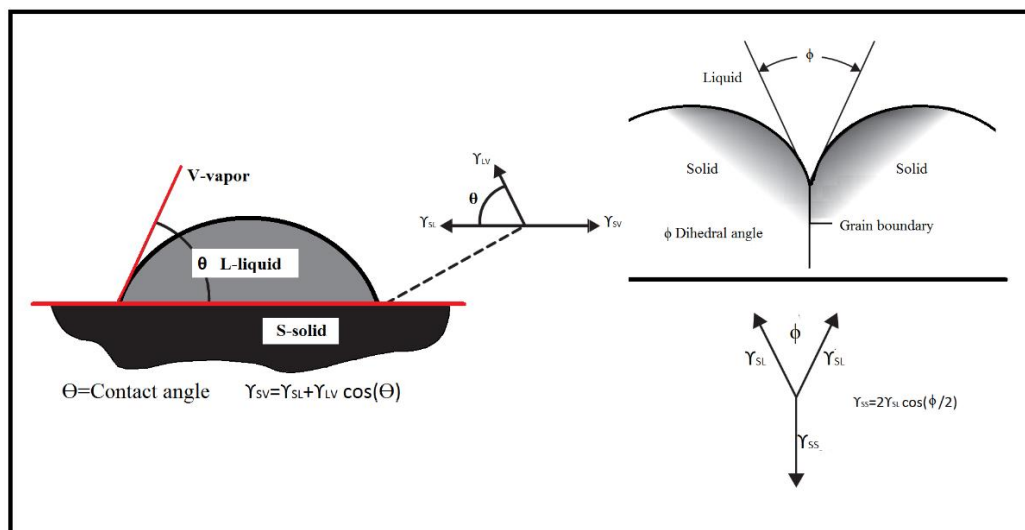
Figure 1.19 Schematic representations of contact angle and dihedral angle [27].

LPS need low dihedral and contact angles to obtain densified structures, whereas SSS application requires to high dihedral angle for neck formation between the particles.

The desired properties of contact angle and dihedral angle for LPS and SSS are given in Table 1.5.

Table 1.5 Desired contact angle and dihedral angle characteristics [30].

	Contact angle	Dihedral angle
SSS	-	high
LPS	low	low

Although SSS treatments are more controllable and predictable, LPS processes are mostly preferred in industry due to necessity of lower temperatures and shorter durations to obtain sintered products [31]. Lots of sintering variables have been investigated to control phenomena, which take place in the LPS process, but the complexity of the process could not have been understood properly yet.

1.3 Review of Related Works

There are lots of W-based heavy alloys in service and used in investigations. However, the studies on Ni-Cu, Ni-Fe and Ni-Co added alloys will be focused and discussed more comprehensively due to possessing wide applications in industry.

According to ASTM B 777-99, the prepared heavy alloys should meet the expected density and hardness properties which are given in Table 1.6.

Table 1.6 The wt.% W content, density and hardness values of WHAs in ASTM B 777-99.

Class	wt.% W content	Density /g/cm3)	Maximum hardness (HRC)
1	90	16.85-17.25	32
2	92.5	17.15-17.85	33
3	95	17.75-18.38	34
4	97	18.25-18.85	35

Kiran et al. [32] investigated the effect of cobalt (Co) and rhenium (Re) addition on mechanical and microstructural parameters of 93W-4.9Ni-2.1Fe (wt.%) heavy alloy composition. They found that addition of rhenium could retard the grain growth of the Re-free alloy. Furthermore, Co led to a relatively high matrix volume fraction formation and higher dissolved W in binder phase. Co addition also improved the impact strength and elongation and hence, it increased the ductility of the alloy. It was

attributed to low contiguity of W-W grains, which decreased the brittleness of the alloys. On the other hand, rhenium added alloys had the highest tensile strength which might have resulted from the finer tungsten grains.

Molybdenum (Mo) addition was studied to obtain finer tungsten grains and hence improve the mechanical properties of tungsten heavy alloys [33-35]. Addition of Mo decreased dissolved W in binder phase, which decelerated the Ostwald-ripening mechanism during sintering [33-35]. Therefore, dissolved Mo in binder might have led to formation of relatively low average W grain size.

Wensheng et al. [36] reported the effects of minor Cr addition on the mechanical properties of 93W-4.9Ni-2.1Fe alloys. The study demonstrated that addition of minor elemental Cr up to 1 wt.% had a negative influence on sintered relative density, tensile strength and elongation. The tensile strength of Cr-free alloy decreased from 997.2 MPa to 844.4 MPa by elemental Cr addition. This was resulted from interfacial cohesion of Cr added alloys which took place at the interphases between chromium, oxygen and the additives.

Dinçer [37] investigated the effect of Ni/Co ratio on microstructural properties and sintering behavior of various W-Ni-Co alloys. He found that as the Ni/Co ratio decreased, densification characteristics of prepared alloys decreased due to solid state binder phase formation at studied sintering temperatures.

The effects of heating method were investigated by microwave and spark plasma sintering. Mondal et al. [38] investigated the effect of microwave sintering method on the densification behavior. In this study, the heating rate of microwave sintering method was 121 °C per min. The rate could not be obtained by conventional sintering methods which generally involves heating rates between 5 and 10 °C/min. They found that employment of microwave sintering method decreased the required time of sintering process when the dwell time of conventional sintering method is considered. By the application of microwave sintering higher densities and smaller W grains were obtained at the same temperature when compared to conventional methods [38].

For spark plasma sintering (SPS) applications, Li et al. [39] investigated the utilization of spark plasma for sintering of 93W-5.6Ni-1.4Fe alloys. They found that SPS employed specimens had finer spherical W grains after sintering compared to ones sintered with conventional methods. Therefore, the binding strength of the sintered alloys could be improved up to 1580 MPa.

German and Bose [40] studied the effects of sintering atmosphere on density and mechanical properties. Utilization of vacuum led to enhanced densification due to accelerated densification rate and formation of entrapped gas free pores. In addition, when pure H_2 gas is employed through the sintering process, a secondary treatment is required to eliminate the embedded H_2 embrittlement. Fully densified structures could be obtained when vacuum and/or H_2 gas atmosphere are employed, whereas employment of only argon inhibited complete densification due to entrapped gas in pores.

Kiran et al. [41] investigated the effect of swaging and post heat treatment on mechanical properties of 90W-6Ni-2Fe-2-Co. Various swaging ratios and aging treatments were performed to better understand the observed results. They found that as the applied swaging ratio increased, the contiguity of W grains decreased and hardness values typically increased. They also found that, the strength of the specimens could reach higher than 1600 MPa by increasing swaging ratio.

When it comes to the fabrication concerns, two main problems are frequently encountered during heavy alloys fabrication; shape distortion and solid segregation. Actually, both of them are mostly based on the same fabrication variables. Suitable additive(s) selection and solid volume fraction-dihedral angle relation are given in Table 1.7 and Table 1.8, respectively.

Table 1.7 Guide for suitable additive element selection [29].

		Solid solubility in liquid	
		Low	High
Liquid solubility in solid	**Low**	Limited densification, rearrangement	Extensive densification
	High	Swelling, transient liquid	Mixed effect swelling & densification

Table 1.8 Shape distortion and densification behavior of LPS depending on solid volume fraction and dihedral angle [29-30].

	Low dihedral angle	High dihedral angle
Low solid fraction	-Rapid densification -Large distortion	-Slow densification -Little distortion
High solid fraction	-Intermediate densification -Intermediate distortion	-Slow densification -No distortion

When the Table 1.7 and Table 1.8 are considered, the desired densification behavior and little or no shape distortion can be obtained theoretically. However, they are not always achieved in practice due to the PM process variables and specimen characteristics. Not only the variables, but also the suitable additive selection should be investigated and performed carefully.

As can be seen in Table 1.7, desired high densified alloys can be obtained when the solid solubility in liquid is high and liquid solubility in solid is low.

W-Cu alloys can be given as an example for low liquid solubility in solid and low solid solubility in liquid condition, the densification parameter of Cu added WHAs is lower than Ni added WHAs. As already demonstrated in Figure 1.13, the slight increases in density of W-Cu alloys can be explained by the rearrangement step of LPS process. These alloys are called as Cu embedded W-Cu alloys. The alloys are generally employed when high strength, via W, and high electrical conductivity, by Cu matrix, are desired at the same time [24]. On the other hand, W-Ni alloys are suitable examples for extensive densification behavior where high solid solubility in liquid and low liquid solubility in solid are expected to obtain considerable shrinkage.

Selection of suitable additive elements are as important as other sintering parameters including applied temperature, time and atmosphere. Binary and ternary phase diagrams of selected additive(s) and base element should be investigated firstly.

As can be seen in Table 1.8, desired liquid phase sintering behavior, rapid densification and no shape distortion cannot be obtained at the same time. Actually, high solid fraction and low dihedral angle conditions generally occur during tungsten heavy alloys sintering. Lower sintering temperatures and longer dwell times can be used to obtain less deformed final products.

The wide density differences, up to 10 g/cm^3, between the liquid and solid W grains cause solid segregation in the compacted specimen. A segregation instance is illustrated in Figure 1.20.
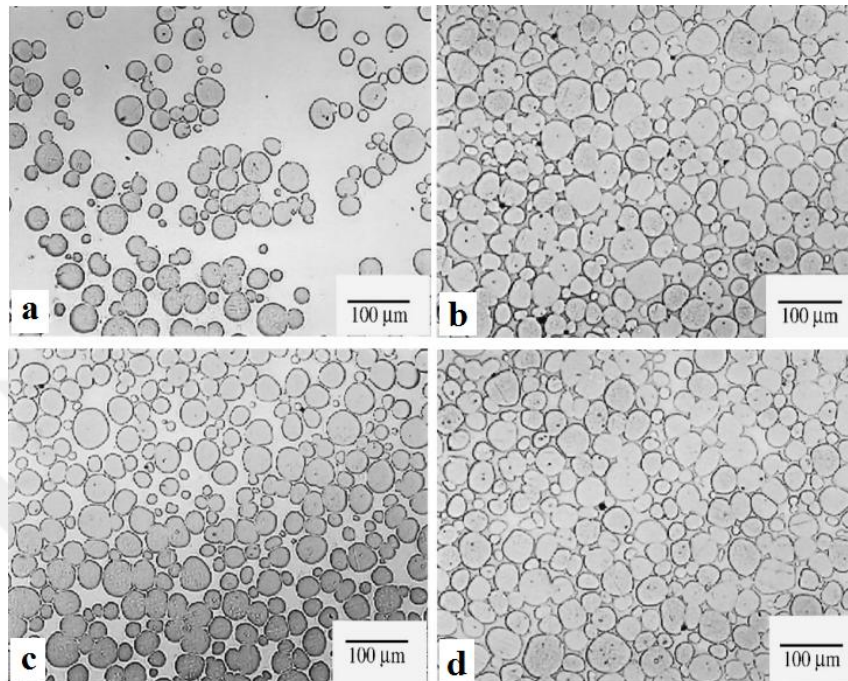
Figure 1.20 Segregation of W grains in liquid (a:78W top, b:78W bottom, c:93W top, d:93W bottom) [42].

As can be seen in Figure 1.20, the place of investigation method has a great influence on determined properties. Top of specimens demonstrates additive-rich behavior, while the bottom indicates W-rich properties. Therefore, a regional examination does not represent the general properties of studied alloys. Xu et. al. [42] investigated the mentioned production concerns. They indicated that the green porosity and tungsten content played a crucial role in sintered properties of fabricated specimens.

Shape distortion problem takes place when there is excessive liquid phase content and high sintering temperatures which both lead to low liquid viscosity. Moreover, contiguity of the grains is also a crucial parameter for shape distortion. The variations of dominant parameters are illustrated in Figure 1.21.
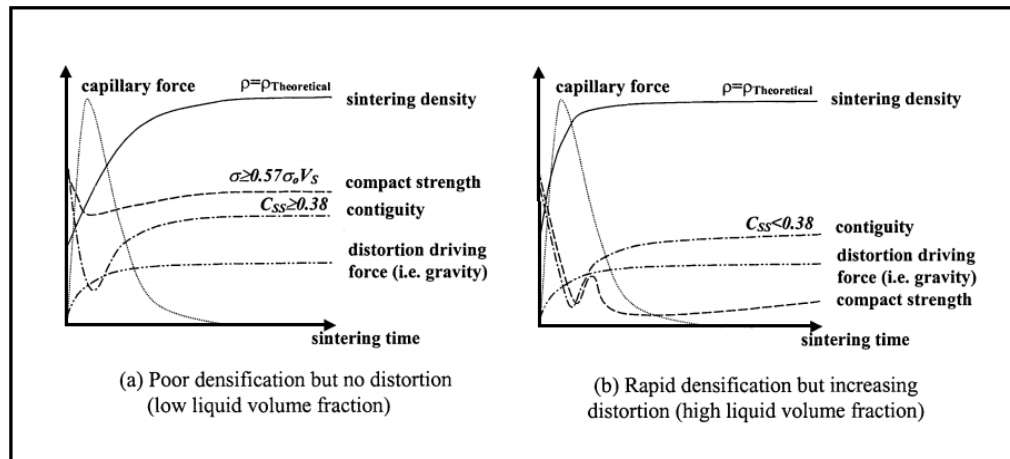
Figure 1.21 The variation of shape distortion parameters during sintering [43].

As can be seen in Figure 1.21, the initial shape of compact can be prevented in poor densification and low liquid volume fraction conditions, because it has higher than critical contiguity values. The contiguity variation is mainly relied on solid volume fraction and dihedral angle. As the dihedral angle increases, necessity of solid volume fraction decreases.

The neck formation in other words contiguity, takes place before the liquid melts. Controlled neck ratio can protect the rigidity of compact when additives melt.

The effect of gravitational force on shape distortion has been investigated in lots of studies. German et al. [44] investigated the effects of microgravity on sintered average grain size. They found that as the fraction of normal gravity decreased, the sintered specimens had relatively smaller average grain size. It was attributed to microstructural stresses, which led to formation of coarser grains.

German [45] also studied the effect of coordination number (CN) of studied compacts on shrinkage. The study demonstrated that value of CN has a great influence on densification tendency. Too low and high CN values have a negative effect on shrinkage ratio and/or rate, but medium distributions like from 5 to 8 are more effective for densification during solid state sintering treatments. Low CN leads to formation of coarsened pores which causes mass transport from pore surface to grain interior and vacancy transport from particle interior to pore surface.

Bollina and German [46] also investigated that the effects of heating rate on microstructure. They studied various heating rates from 1 °C/min to 15 °C/min. They found that heating rate had mostly similar effects on shape distortion and normalized grain size. However, the changes in shape distortion and normalized grain size were much more dominated by the sintering temperature. Normalized grain size can be measured via dividing actual grain size (G) by median grain size (G_M). In addition, as the applied heating rate increased, temperature of fastest shrinkage rate (%/min) also increases from 1460 to 1480 °C.

1.4 Aim of the Study

The study is aimed to investigate the sintering behavior of tungsten powder produced by electrochemical deoxidation method. The current tungsten powder production method has some production difficulties such as working with H_2 gas, necessity of external heat supply, long and complicated extraction steps, whereas novel approach for tungsten powder production by molten salt electrolysis process is simpler and safer. Owing to its benefits, it has a high commercializing potential, yet the sintering behavior of the produced powder has not been investigated up to now.

This thesis aimed to fill the gap mentioned above. For this aim, a series of sintering studies were performed by employing commercially available tungsten powder to obtain comparison data for electrochemically produced tungsten applications.

Furthermore, the effects of sintering variables such as sintering temperature, duration, atmosphere, powder composition, wt. % W content on densification behavior of both unalloyed and alloyed compacts were investigated.

CHAPTER 2

EXPERIMENTAL PROCEDURE

A series of sintering studies were performed with commercially available tungsten and electrochemically produced powders to investigate and compare the sintering behaviors. Electrochemically produced tungsten powder will be referred as W* and the commercial tungsten powder will be referred as W powder from this point on this thesis. The conducted studies can be divided into two main parts as solid state sintering (SSS) and liquid phase sintering (LPS) applications. The SSS experiments were conducted to investigate the unalloyed form densification behavior, whereas LPS experiments were employed to compare the densification behavior of both powders in liquid phase by adding transition metals Ni, Co and Fe as binder phase. The prepared alloys contained at least 90 wt.% W and/or W* powder and appropriate binder matrix phases, which were formed from various Ni/Co, Ni/Fe, Co/Fe and Ni/Co/Fe ratios. Conventional powder metallurgy (P/M) specimen preparation procedures were employed to obtain the desired alloys.

2.1 Alloy Preparation

2.1.1 Raw Materials

W* powder and commercially available elemental powders of W (Alfa Aesar, 10400), Ni, Co, Fe were employed to prepare various type WHAs and W*HAs through forming binary, ternary and quaternary alloys. Initial morphologies of used powders are illustrated in Figure 2.1. The main properties, including particle size range, particle shape, purity, fabrication method and source of powders are given in Table 2.1.

2.1.2 Selected Alloy Compositions and Process Parameters

The commercial W powder and its various heavy alloy combinations were prepared to investigate the influences of sintering variables on densification behavior and microstructural properties. These alloys were also used as a control group due to relatively easier estimation of sintering performance under altered variables.
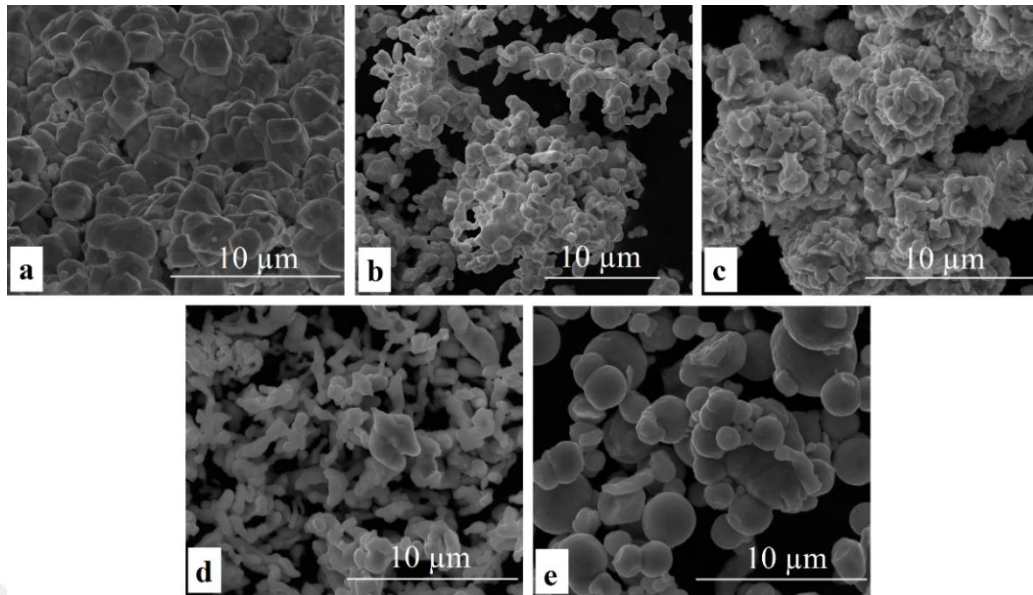
Figure 2.1 Initial morphologies of as-received and produced powders obtained
by SEM. (a-W, b-W*, c-Ni, d-Co, e-Fe)

Table 2.1 General properties of as-received and produced elemental powders.

Element	Particle Size Range (μm)	Shape	Purity (wt. %)	Fabrication Method	Source
W	1-5	Polygonal	99.9	Hydrogen reduction	Alfa Aesar 10400
W*	<1	Polygonal	98 <	Electrochemical reduction	Obtained [4–6]
Ni	3-7	Polygonal	99.9	Carbonyl	William Rowland Vale 123
Co	1.6	Polygonal	99.8	-	Alfa Aesar 10455
Fe	<10	Spherical	99.9+	Carbonyl	Alfa Aesar 00170

2 wt.% is mainly consisted from, Ca and its compounds, and stainless steel spoon (Fe, Cr, Ni, Mo)

The schematic explanation of prepared alloy codes in given Figure 2.2.

In addition, sintering behavior of W* powder was investigated for the same parameters and compared to that of W powder. In some of the experiments, W* powder was directly used after electrochemical reduction while in some others it was further subjected to purification and homogenization processes before sintering experiments. The untreated powder (W**) studies were practiced with unalloyed and 0W**4/1NC W**HAs sintered at 1500 and 1550 °C for 1 h.
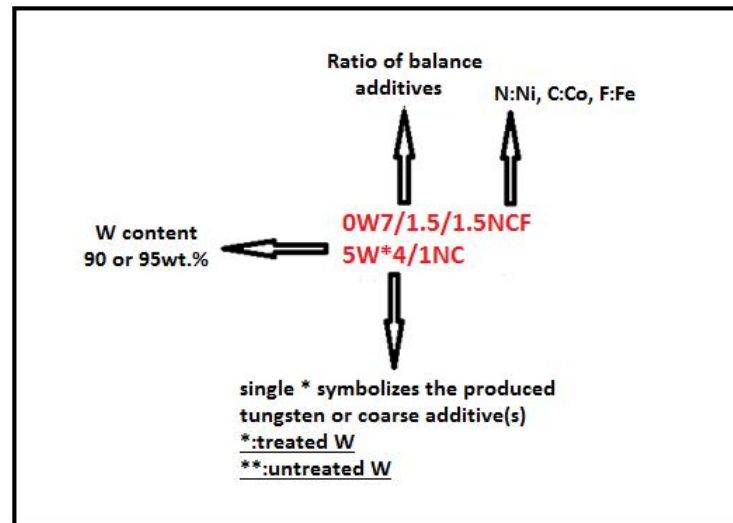
Figure 2.2 Schematic explanation of alloy codes.

Moreover, treated powder (W*) sintering studies were conducted with various type heavy alloy combinations. The treatments included calcium evaporation process (CEP) and ultrasonic homogenization process (UHP), which were performed to enhance the sintering behavior of electrochemically produced tungsten powder. CEP, is a pre-sintering treatment, performed to evaporate Ca dissolved in W as a result of the electrochemical reduction process. It included a heat treatment at temperatures up to 1200 °C under a vacuum of $1x10^{-6}$ atm. CEP performed heavy alloys, having a composition of 0W*4/1NC, were sintered at 1500 and 1550 °C for 1 h.

The second applied enhancement method was ultrasonic homogenization process (UHP), This process was conducted to improve the green density values of the W* powder under compression. The UHP study was performed with a ultrasonic processor (MSK USP 12 MTI Corporation) under 30 % maximum power of device for 5 min. The UHP applied powders were sintered at 1500 and 1550 °C for 1 h with unalloyed and different heavy alloy combinations, 0W*7/3NC, 0W*7/3NF, 0W*4/1NC, 0W*8/1NC and 5W*4/1NC.

The studied alloys can be divided into three parts according to alloying types. The effects of single additives on densification were studied with 10 wt.% Ni, Co or Fe. These WHAs were sintered at three different temperatures from 1450 to 1550 °C. Furthermore, Ni contained WHAs and W*HAs were investigated to compare the

sintering behavior and microstructural properties of the studied alloys. 90 and 95 wt.% W contained alloys were constituted with various Ni-Co, Ni-Fe and Ni-Co-Fe ratios. Finally Ni-free WHAs were also examined to better understand the effect of solubility on sintering behavior. Therefore, various combinations of Co-Fe added WHAs were sintered at different temperatures and durations. Schematic representations of the prepared WHAs and W*HAs are given in Figure 2.3 and Figure 2.4, respectively.
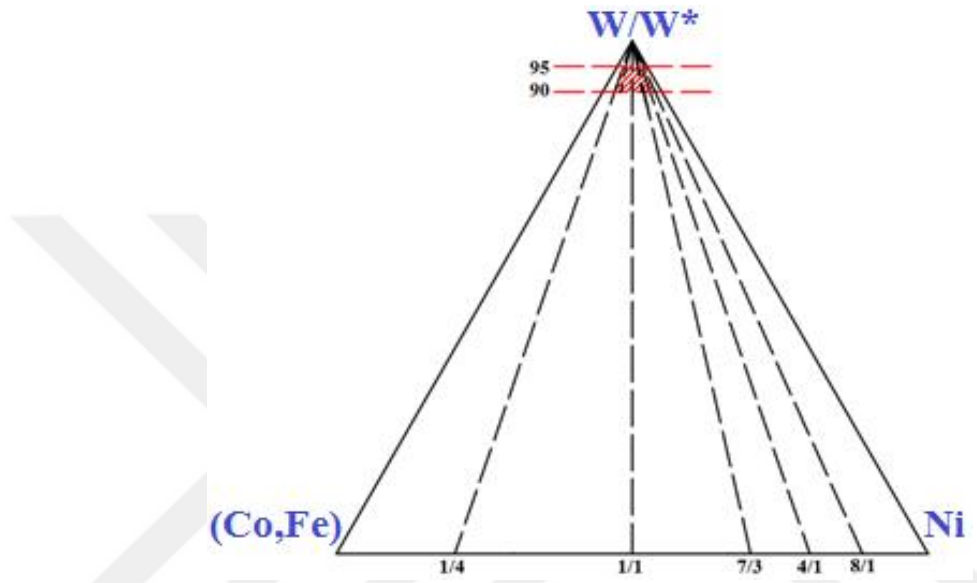
Figure 2.3 The triangle phase diagram of the W-rich Ni/Co, Ni/Fe and Ni/Co/Fe alloys studied.
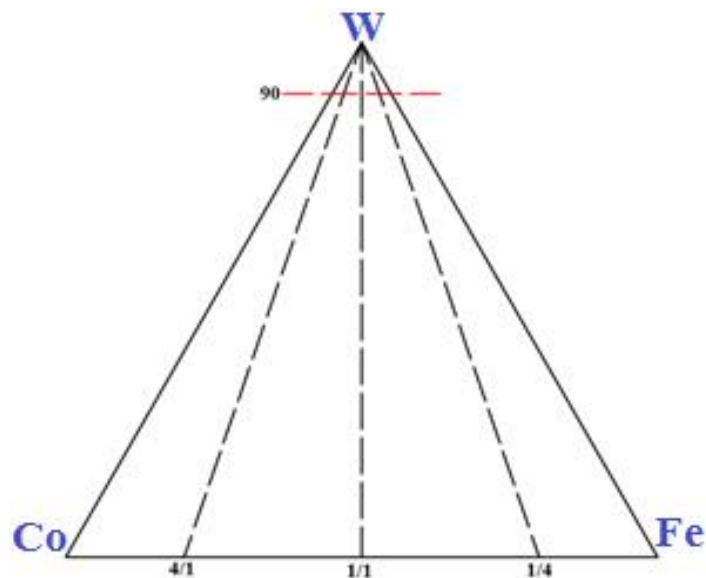
Figure 2.4 The triangle phase diagram of the studied W-rich W-Co-Fe alloys.

The alloys having a Ni/Co ratio of 8/1, 4/1, 7/3, 1/1 and 1/4 alloys were investigated with 90 and 95 wt.% W powder. The Ni/Fe ratio 8/1 and 7/3 alloys were also sintered to investigate the effect of secondary additive alternation on densification behavior and microstructural properties.

In addition, Ni-free WHAs with 90 wt.% W content and various Co-Fe ratios including 1/4, 1/1 and 4/1 were also prepared. Apart from these alloys, a quaternary alloy was investigated which had 0W7/1.5/1.5 NCF composition.

On the other hand, various combinations of W*HAs were prepared by CEP and UHP applied W* powder. 90 wt.% W* powder contained 7/3NC, 7/3NF, 4/1NC and 8/1NC alloys and 95 wt.% W* powder contained 4/1NC alloy were sintered in an atmosphere controlled high temperature furnace.

The studied specimens are listed in Table 2.2, together with the alloy code, mass ratios of investigated alloys and their theoretical densities.

2.1.3 Powder Blending and Compaction Procedures

The weight measurements of targeted WHAs and W*HAs compositions were performed by a precision balance (Mettler Toledo MS-304S) which has 0.1 mg accuracy. 5 g and 20 g of desired compositions were put into a polypropylene (PP) container. The mixing process was carried out by a laboratory-sized speed mixer instrument (DAC 150.1 FVZ) at 500 rpm for 30 min. The mixing process was performed with 5 minutes periods to decrease the generated heat from powder friction.

2 g and 3 g mixed powders were weighted and then pressed under 350 MPa for 2 min by a hand press (MSE LP_M2S10). In addition, 300 MPa and 400 MPa compression pressure for 2 minutes were also carried out to find out the influences of initial green density on densification behavior of selected alloys. On the other hand, 400 MPa for 5 min, 500 MPa for 2 min were also performed for W* powder employed W*HAs to enhance the initial relative density of green compacts.

Table 2.2 Composition and theoretical density of studied tungsten powders and their alloys.

Alloy code	W/W*	Ni	Co	Fe	Others	Mass ratio	Theoretical density
W	100	-	-	-	-	-	19.3
W*	98<	trace	-	<1	<1	-	19.3[a]
0W10N	90	10	-	-	-	-	17.28
0W10C	90	-	10	-	-	-	17.29
0W10F	90	-	-	10	-	-	16.85
0W1/4NC	90	2	8	-	-	1/4	17.29
0W1/1NC	90	5	5	-	-	1/1	17.29
0W7/3NC	90	7	3	-	-	7/3	17.29
0W7/1.5/1.5NCF	90	7	1.5	1.5	-	7/1.5/1.5	17.22
0W7/3NF	90	7	-	3	-	7/3	17.15
0W4/1NC	90	8	2	-	-	4/1	17.28
0W8/1NC	90	8.89	1.11	-	-	8/1	17.28
0W8/1NF	90	8.89	-	1.11	-	8/1	17.23
0W*7/3NC	90[a]	7	3	-	-	7/3	17.28[a]
0W*7/3NF	90[a]	7	-	3	-	7/3	17.15[a]
0W*4/1NC	90[a]	8	2	-	-	4/1	17.28[a]
0W**4/1NC	90[a]	8	2	-	-	4/1	17.28[a]
0W*8/1NC	90[a]	8.89	1.11	-	-	8/1	17.28[a]
0W4/1CF	90	-	8	2	-	4/1	17.20
0W1/1CF	90	-	5	5	-	1/1	17.06
0W1/4CF	90	-	2	8	-	1/4	16.93
5W1/4NC	95	1	4	-	-	1/4	18.24
5W1/1NC	95	2.5	2.5	-	-	1/1	18.24
5W7/3NC	95	3.5	1.5	-	-	7/3	18.24
5W4/1NC	95	4	1	-	-	4/1	18.24
5W8/1NC	95	4.44	0.56	-	-	8/1	18.24
5W*4/1NC	95[a]	4	1	-	-	4/1	18.24[a]

(a: Amount of impurity contents ignored)

2.1.4 Sintering Process

The prepared alloys were sintered at different sintering temperatures to investigate the effect of applied temperature on sintering behavior of studied alloys. Unalloyed W and W* powders were sintered at 1500 and 1550 °C for 1 hour under pure H_2 gas flow. Moreover, various types liquid phase sintering (LPS) treatments were studied using prepared WHAs and W*HAs.

Co-rich WHAs and Ni-free Co-Fe added WHAs were also sintered at 1550 °C for 90 and 120 minutes to increase relative density values. The heating-cooling profile of atmosphere controlled high temperature furnace is given in Figure 2.5.
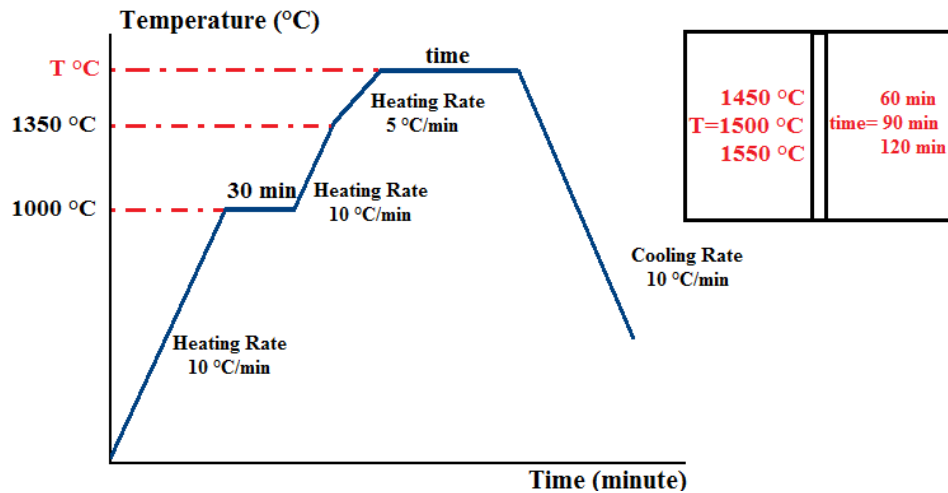
Figure 2.5 The performed heating-cooling profile of sintering experiments [37].

This profile was taken from a previous study [37] directly to obtain comparative data for the different parameters used in the present study.

The horizontal tube furnace used in the sintering experiments had a ±12 °C temperature uniformity and approximately 150 mm hot zone which was measured by an S type thermocouple. Before each sintering experiment, the furnace was vacuumed down to less than $1x10^{-6}$ atm by a PFEIFFER Hi-CUBE vacuum pump. Thereafter, the vacuumed furnace was filled quickly by Ar gas with 2 l/min gas flow to prevent penetration of oxygen through the chamber which was in a negative pressure. Pure H_2 gas at a flow rate of 0.2 l/min, or 50%Ar-50%H_2 mixture at a flow rate of 0.4 l/min were used during sintering experiments. The furnace was purged with the required atmosphere for half an hour before heating was started. The gas flow was maintained during the whole sintering process and cooling stage.

2.2 Experimental Setup

A self-designed atmosphere controlled sintering furnace was used in the experiments. The furnace was consisted of four parts: furnace and its controller, water cooling system, gas cylinders and mass flow controllers and vacuum pump system. Schematic representation of the furnace and its apparatus are illustrated in Figure 2.6.
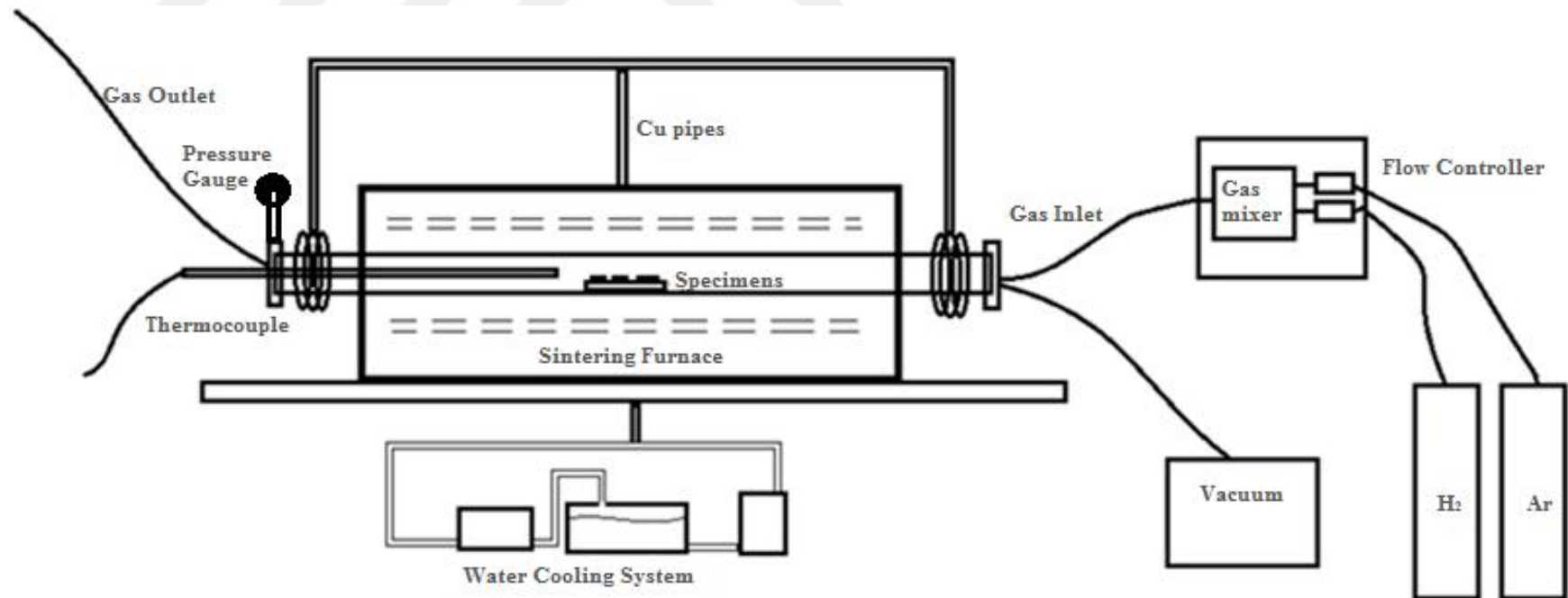
Figure 2.6 Designed high temperature furnace and its apparatus.

The determined gas flow rate and composition were adjusted by the gas controller unit which had both automatic and manual solenoid valves to stop the gas flow in case of hydrogen leakage. In order to determine any leakage, a hydrogen sensor (Macurco HD-11) was used.

Water cooling was employed for continuous cooling of Al_2O_3 tube edges to protect the sealing materials from high temperature.

The vacuum system was used to provide an oxygen free atmosphere for the sintering experiments. It was also used in the calcium evaporation process mentioned in section 2.1.2.

2.3 Characterization Techniques

Characterization methods can be collected under four main titles: microstructural examinations, compositional analyses, densification and micro/macro scale hardness measurements.

2.3.1 Microstructural Examination

Microstructural tests were performed to investigate the following objectives:

a. to find out and identify the phases and intermetallics formed,
b. to observe the effect of additive amounts on densification, grain morphology and average grain size (AGS),
c. to investigate the effect of sintering variables on grain size distribution
d. to observe shape distortion tendency and segregation of W particles in WHAs and W*HAs.

The conventional metallographic sample preparation method was employed for the sintered WHAs and W*HAs. Some of the selected alloys were sectioned by a low speed diamond saw (MTI SYJ-150) to investigate the vertical microstructural changes and possible W segregation due to gravitational force and wide density differences between the solid and liquid phases. The selected alloys were separately mounted into

bakelite using two different hot mounting presses, ATM Opal 460 and Pressi Mecapress 3.

Grinding procedure of the mounted specimens was performed by means of SiC papers from 320 to 1200 grit, using a metallographic sample preparation machine (Pressi Minitech 263). And then, they were polished with 6, 3 and 1 μm diamond particles suspended on a suitable cloth. In addition, final polishing step of specimens were done via 0.25 μm diamond particles contained suspension for approximately 20 minutes on an appropriate flocked polishing cloth. The polishing procedure of mounted alloys was conducted via metallographic sample preparation machine (Metkon Forcipol 2V).

The polished samples were etched with Murakami's solution which was prepared by mixing 2.5 g potassium ferricyanide ($K_3Fe(CN)_6$), 2.5 g NaOH and 25 ml distilled water (H_2O). The etching procedure of the prepared alloys was carried out by swabbing into the prepared etching solution from 5 to 20 seconds to obtain appropriate surface for microstructural examination. And then, the specimens were cleaned with water and alcohol, respectively. The wet surfaces of the samples were dried by applying hot air.

The microstructures of the sintered specimens were examined by optical microscope (NIKON Eclipse MA 100 inverted OM) and scanning electron microscopes (SEM). Secondary electron images (SEI) mode was employed to obtain topographical images from sintered alloys by a Nova NanoSEM 430, while backscattered electron imaging (BEI) mode was used to obtain compositional contrast by a Jeol 6400 JSM SEM. Furthermore, energy dispersive spectroscopy (EDS) analyses were performed to identify the binder phase composition of the selected alloys by EDAX TEAM EDS analysis system attached to FEI Nova NanoSEM 430. Line EDS measurements were conducted using EDAX TEAM EDS system with a secondary electron mode via FEI Nova NanoSEM 430.

The OM investigations of the sintered specimens were conducted with different magnifications ranging from 50 to 1000x. Microstructural images of each studied specimens are illustrated in Appendix B. Clemex camera and its software was employed to take microstructure images and determine the AGS, GSD of selected alloys.

Average grain size (AGS) measurements of the selected alloys were carried out by Jefferies (Planimetric) method according to ASTM E112 standard. In order to calculate the AGS of selected alloys, two equations were employed, which are given in Eq. 2.1 and 2.2, respectively.

$$N_A = f\left(N_{inside} + \frac{N_{intercept}}{2}\right) \tag{2.1}$$

$$\bar{A} = \frac{1}{N_A} \tag{2.2}$$

Where N_A is the number of total grains per square millimeter (mm) counted at 1x magnification, N_{inside} is counted complete grains in circle, $N_{intercept}$ is the number of grains intercepted by circle, f is Jefferies multiplier (8.0 for 200x) and $\bar{A}$ is the average grain area for each alloy. At least three AGS measurements were obtained for each alloy by drawing a circle, which has a 5000 mm^2 area.

GSD measurements were conducted by OM at 200x magnification. Randomly selected 100 grains were used to determine the grain size distribution of selected alloys. The effects of sintering variables on GSD; including temperature, W content and variation of Co and Fe with constant Ni ratio, were also investigated.

Binder phase area measurements of the selected alloys were done by ImageJ software. The contrast diversity between W grains and binder phase was employed during the measurements.

2.3.2 X-ray Diffraction and X-ray Fluorescence Analyses

X-ray fluorescence (XRF) analyses (Fisherscope X-ray XDV-SDD Optiplex 3020) were applied to determine possible impurities and their amount in W* powder obtained from scheelite ($CaWO_4$) by electrodeoxidation process. It was also used to investigate the compositional homogeneity of the alloys after compression and sintering.

X-ray diffraction (XRD) analyses were carried out to determine the phases formed between tungsten powders and their additives during sintering process. Cu Kα X-ray beam source at 40 kV was employed during examinations. The analyses were

performed at 2°/min scan rate between 10° to 90° 2θ angles by an X-ray diffractometer (Rigaku Miniflex 600). The phase identifications of the selected alloys were performed using a diffraction analysis program (PDXL).

2.3.3 Density Measurements

Firstly, the theoretical densities of studied specimens were calculated by the rule of mixtures as given in Eq. 2.3.

$$\frac{1}{\rho_{theo}} = \frac{W_{wf}}{\rho_w} + \frac{Ni_{wf}}{\rho_{Ni}} + \frac{Co_{wf}}{\rho_{Co}} + \frac{Fe_{wf}}{\rho_{Fe}} \qquad \textbf{(2.3)}$$

Initial green densities of the unalloyed and alloyed pellets were measured by dimensional methods, whereas sintered densities were measured using Archimedes' principle. A precision balance (Mettler Toledo MS-304S) which has 0.1 mg precision and a density calculation kit were used during this procedure. Firstly, dry weights of the samples were measured. And then the samples were boiled in distilled water for 2 h. The boiled specimens were measured for two different conditions; saturated mass and immersed weight using the density kit. These measurements were repeated three times and the calculated average dry weight, saturated mass and immersed weight of specimens were employed during green density measurements. The sintered densities of each specimens were also measured using these steps, but the samples were lightly ground before the measurement procedure to eliminate surface contaminants.

The green and sintered densities of the studied alloys were determined with the help of Eq. 2.4. given below:

$$\rho = \frac{m_{air}}{\left(m_{liquid-air} - m_{liquid}\right)} x \rho_{water} \qquad \textbf{(2.4)}$$

Where ρ is the calculated density (g/cm³), m_{air} is the dry weight, $m_{liquid-air}$ is the saturated mass, m_{liquid} is the wet weight and ρ_{water} is the density of distilled water.

Green and sintered relative densities can be obtained by dividing the calculated density of green compact and/or sintered body to the theoretical density which was determined by Eq. 2.3.

Densification parameter (Ψ), can be calculated using fractional initial and sintered densities of the specimens. The formula is given in Eq. 2.5.

$$\Psi = \frac{f - f_0}{1 - f_0} \tag{2.5}$$

Where Ψ is the densification parameter, f is the fractional sintered density and f_0 is the fractional initial density.

Moreover, the shape distortion behaviors of some selected alloys were investigated to compare dimensional changes of fired alloys by normalized height and/or normalized radius formula which is given in Eq. 2.6.

$$Normalized\ height(or\ radius) = \frac{sintered\ height\ or\ radius}{initial\ height\ or\ radius} \tag{2.6}$$

2.3.4 Micro and Macro Hardness Tests

The hardness measurements were performed by two different hardness testing methods. The microhardness tests were practiced with Vickers diamond indenter by SHIMADZU HMV-G micro Vickers hardness tester. Microscale general hardness results of studied specimens were measured under 9.807 N load for 6 seconds holding time, whereas the binder phase hardness values were measured under 0.049 N load for 6 seconds. At least five measurements were taken from each specimen. On the other hand, macro scale hardness values of selected heavy alloys were performed by spheroconical diamond. Rockwell A hardness (HRA) results of sintered alloys were measured using Qness Q750 macrohardness tester.

CHAPTER 3

RESULTS AND DISCUSSION

3.1 Comparison of Sintering Behaviors of W and W* Powders

3.1.1 Densification Parameters and Relative Densities

The measured % relative density results of the W and W* powders and their alloys are compared in Table 3.1.

Table 3.1 Relative densities (%RD) of the sintered WHAs, W*HAs and W**HAs.

Alloy code	Relative density (%)				
	Sintering temperature and dwell time (°C/min)				
	1450/60	1500/60	1550/60	1550/90	1550/120
W	-	66.4	70.7	-	-
W*	-	83.7	85.3	-	-
W**	-	76.3	77.2	-	-
0W10N	95.1	97.3	98.7	99.0	-
0W10C	68.1	70.9	82.2	83.9	-
0W10F	67.5	71.3	80.8	82.3	-
0W1/4NC	80.0	86.8	92.5	93.7	94.3
0W1/1NC	98.4	99.3	99.9	-	-
0W7/3NC	97.2	98.7	99.6	-	-
0W7/1.5/1.5NCF	97.4	98.8	99.8	-	-
0W7/3NF	97.0	98.6	99.7	-	-
0W4/1NC	97.5	98.9	99.7	-	-
0W8/1NC	97.3	99.2	99.9	-	-
0W8/1NF	97.9	98.7	99.4	-	-
0W*7/3NC	-	86.4	90.5	-	-
0W*7/3NF	-	85.2	-	-	-
0W*4/1NC	-	78.2/80.8	85.6/87.5	-	-
0W**4/1NC	-	63.2	66.0	-	-
0W*8/1NC	-	90.3	-	-	-
0W1/4CF	-	80.1	86.1	86.4	87.1
0W1/1CF	-	81.6	82.3	86.6	87.5
0W4/1CF	-	78.5	83.3	84.6	85.8
5W1/4NC	80.8	86.8	92.9	94.2	94.6
5W1/1NC	94.2	99.2	99.6	-	-
5W7/3NC	95.6	98.8	99.3	-	-
5W4/1NC	96.0	98.7	99.4	-	-
5W8/1NC	95.5	98.3	99.6	-	-
5W*4/1NC	-	-	92.2	-	-

The measured green densities, relative green densities and sintered densities are also given in Appendix A, which are necessary for densification parameters (DP(Ψ)) determinations. DP(Ψ) results of the W, untreated (W**) and treated (W*) powders are given in Figure 3.1 with single additive WHAs.
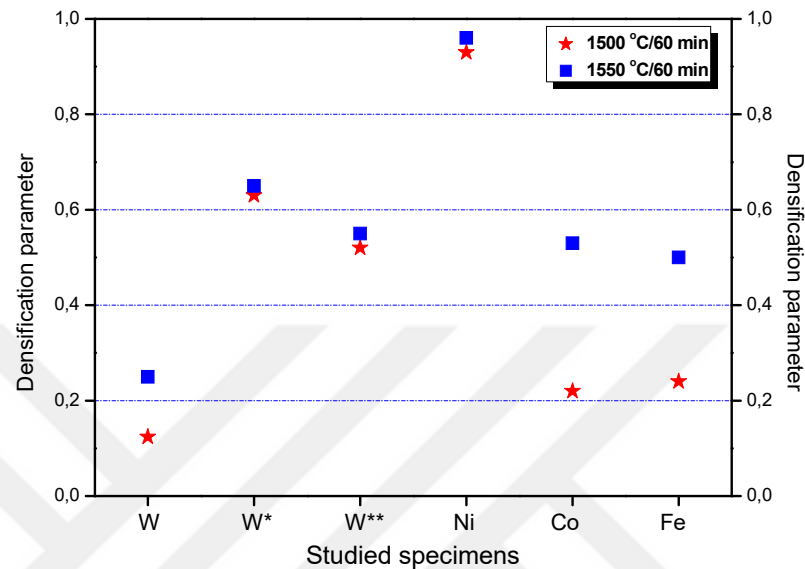
Figure 3.1 DP(Ψ) results of the pure W, W*, W** powders and single additive WHAs.

As can be seen in Figure 3.1, as the sintering temperature increased, the densification tendency of the studied specimens also increased. The temperature variation has a slight effect on DP(Ψ) values of the W, W*, W** and Ni added WHAs, whereas Co and Fe added WHAs exhibited relatively high densification parameter variations with altered temperature. It may be attributed to relatively lower DP(Ψ) values of the Co and Fe added WHAs, especially at 1500 °C, when compared to Ni added WHAs.

As for DP(Ψ) values of the unalloyed compacts, W* and W** powders have relative higher DP(Ψ) values than W powder. It can be resulted from their impurity content. The contaminations might have enhanced the densification tendency of W* and W** powders by providing activated sintering conditions and/or a trace amount of liquid phase formation between the grains. The microstructure image of W** powder, sintered at 1550 °C for 1 h, is given in Figure 3.2.
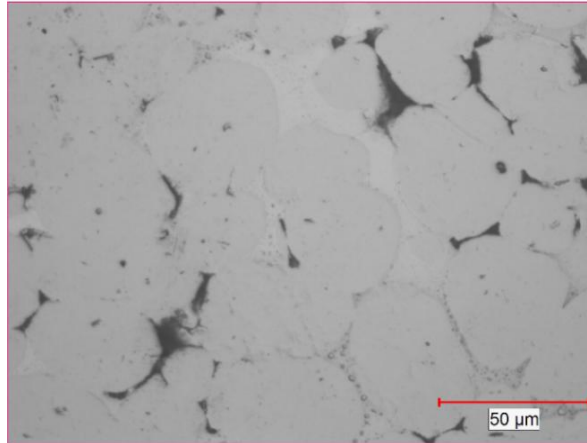
Figure 3.2 Microstructure of the sintered W** powder (1550 °C for 1 h, 500x).

Formed liquid phase can be seen in Figure 3.2 between the grains. This phenomenon was not observed through the whole structure. It was limited to some specific locations where the impurity content may reach to sufficient concentrations for liquid phase formation with low melting point elements. Microstructures of the other studied alloys are provided in Appendix B.

The applied sintering temperature, W content and alloying elements and their weight concentrations are also important factors for DP(Ψ) values of prepared the WHAs. Calculated DP(Ψ) values for the 90 wt.% W and 95 wt.% W contained alloys are illustrated in Figure 3.3 and Figure 3.4, respectively.
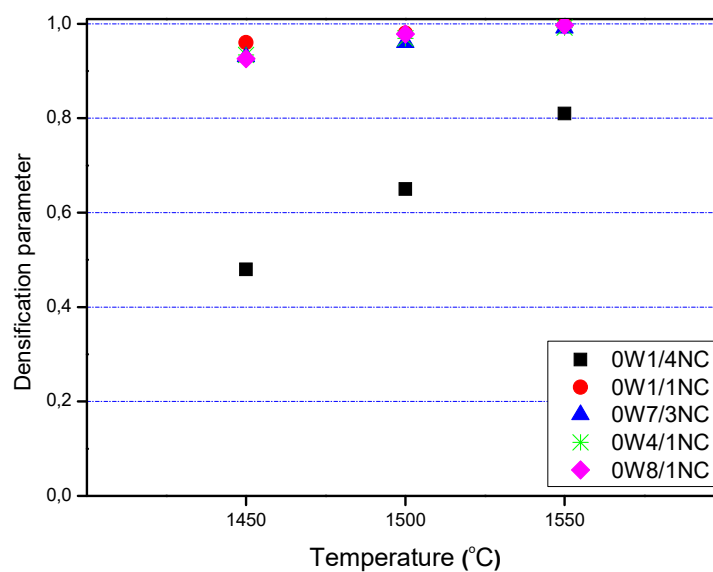
Figure 3.3 DP(Ψ) results of the 90 wt.% W contained WHAs, sintered for 1 h.
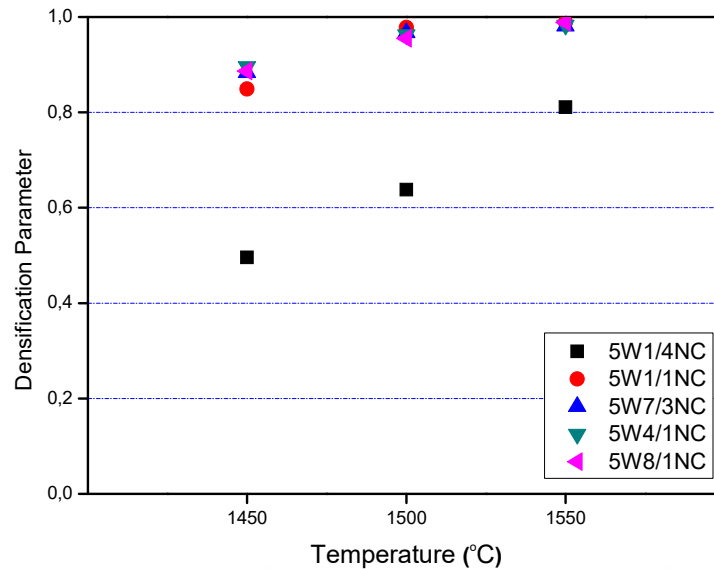
Figure 3.4 DP(Ψ) results of the 95 wt.% W contained WHAs, sintered for 1 h.

As can be seen in Figure 3.3 and Figure 3.4, except from Co-rich alloys, all studied alloys had a considerable amount densification tendency. In addition, as the sintering temperature increased, DP(Ψ) values of studied alloys also increased due to accelerated atomic motion. However, Co-rich heavy alloys indicated relatively lower densification behavior than Ni-rich WHAs. It is predicted that Co may cause relatively lower liquid path formation between the tungsten grains by forming solid intermetallic phases [47].

It was seen that the DP(Ψ) values of the WHAs also increased slightly for the Co-rich WHAs as the W content increased. The effects of Ni/Co ratio, W content and sintering temperature on densification behavior of 90 and 95 wt.% W containing alloys are illustrated in Figure 3.5 and Figure 3.6, respectively.

As can be seen in Figure 3.5 and Figure 3.6, except from Co-rich heavy alloys and 95 wt.% W contained alloys sintered at 1450 °C for 1 hour, all specimens indicated considerable densification tendency.

Co-rich heavy alloys, which were insufficiently densified at 1450 °C, were also sintered at 1550 °C for 90 and 120 min. The effect of W content and dwell time on Co-rich heavy alloys' densification are illustrated in Figure 3.7.
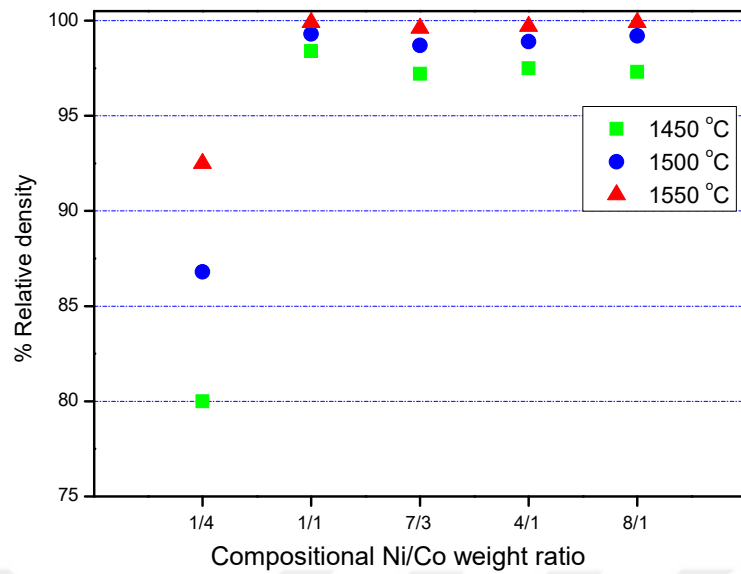
Figure 3.5 Relative density variation of the 90 wt.% W contained heavy alloys, sintered for 1 h.
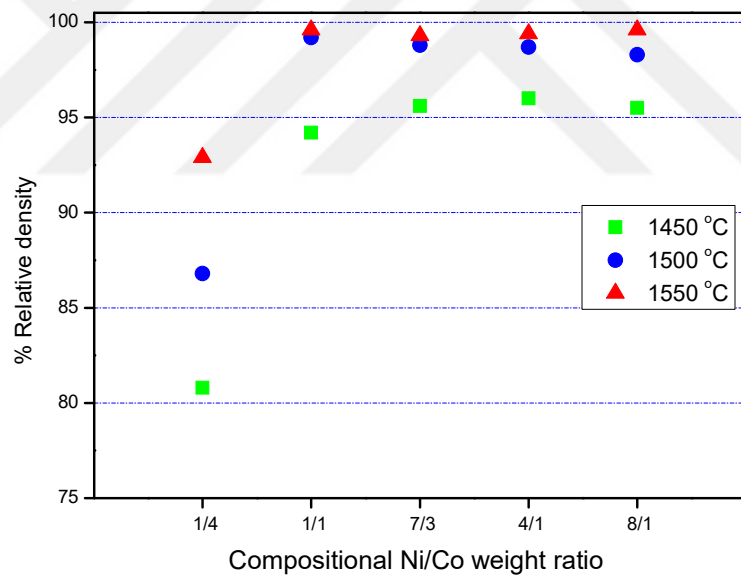
Figure 3.6 Relative density variation of the 95 wt.% W contained heavy alloys, sintered for 1 h.

As can be seen in Figure 3.7, the relative densities of the sintered Co-rich heavy alloys are strongly influenced by sintering variables. Increased sintering temperature caused considerably higher densification, whereas, the effect of W content was less significant.
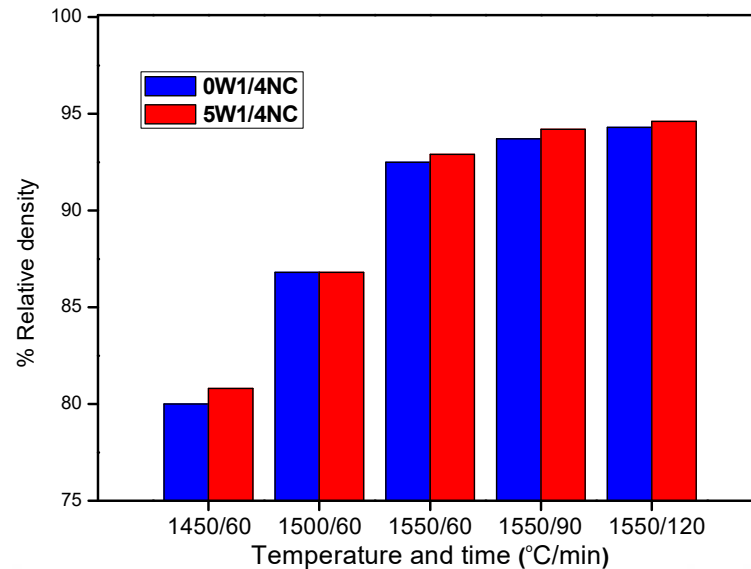
Figure 3.7 The effect of W content and sintering temperature on relative densities of the Co-rich heavy alloys.

Since the 90 wt.% W contained WHAs have relatively higher amounts of binder phase volume, the distances between W grains increased and hence, this binder phase decreases densification values of the prepared WHAs [37].

3.1.2 Microstructural Examinations

Optical microscope images of the all unalloyed and alloyed specimens are given Appendix B. Moreover, secondary (SEI) and back scattered (BEI) electron images were taken to observe the variations of final microstructure with sintering variables.

The microstructures of Ni-rich heavy alloys had almost spherical and pure W grains and uniform binder phase. The microstructures of 90 wt.% W contained heavy alloys are illustrated in Figure 3.8.

As can be seen in Figure 3.8, Co-rich and 1/1 Ni/Co ratio added heavy alloys had a considerably different microstructure when compared to other sintered alloys. Furthermore, the microstructures were not affected much from altered W content, which is demonstrated in Figure 3.9. Except from sintering at 1450 °C, spherical W grain shape and two binder phase contained microstructure could be observed at 1/1 ratio Ni and Co added alloys.
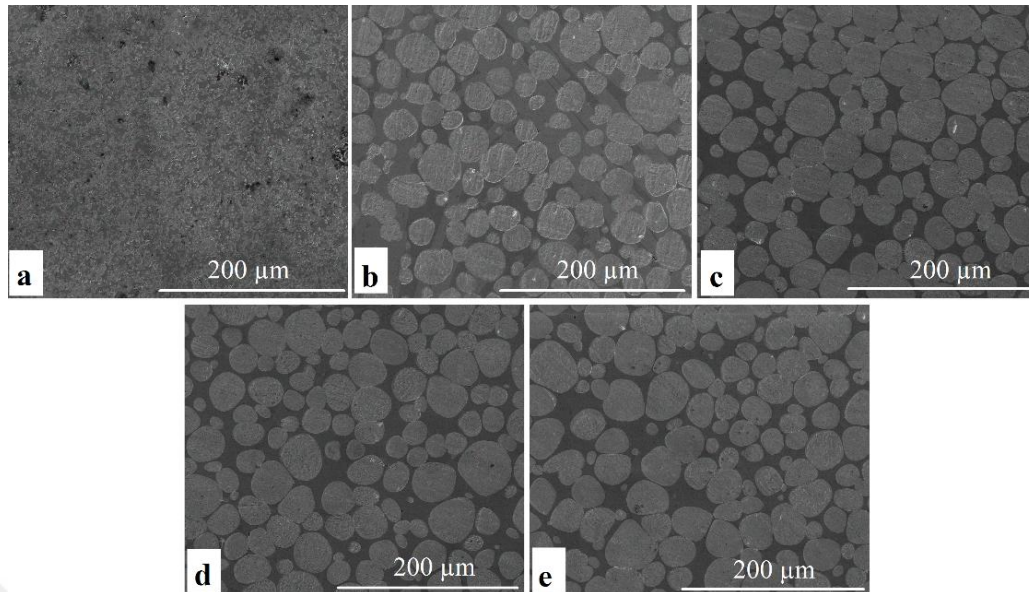
Figure 3.8 Typical, SEI mode, micrographs of the 90 wt.% W contained WHAs, sintered at 1550 °C (a:0W1/4NC, b:0W1/1NC, c:0W7/3NC, d:0W4/1NC, e:0W8/1NC).

Co-rich WHAs could not reach adequate relative density ratios as already demonstrated in Figure 3.5 and Figure 3.6. Therefore, they are not suitable for WHAs applications due to high porosity amount which decreases the mechanical properties, in particular tensile strength and toughness values [24]. When Co-W phase diagram [47] given in Appendix C is considered, the expected liquid phase formation could not be observed in applied sintered conditions. As mentioned phase diagram, which is given in Appendix C, demonstrates that the sintering temperature should be increased approximately 1690 °C to obtain liquid phase, but 2-3 wt.% Ni addition decreases the temperature between 1500-1550 °C. Therefore, it can be suggested that the selected Ni/Co ratio should be equal or higher than 3/7 ratio.

W* or W** powder employed heavy alloys had quite different microstructures as illustrated in Figure 3.10. As can be seen in Figure 3.10, densification ability of W* powders are quite sufficient. When the sintered grain structures are considered, they have similar microstructures with fully densified WHAs prepared via commercial W powder. Formation of spherical grains is attributed to sintering conditions and the properties of W* powder, which were suitable to obtain desired densification.
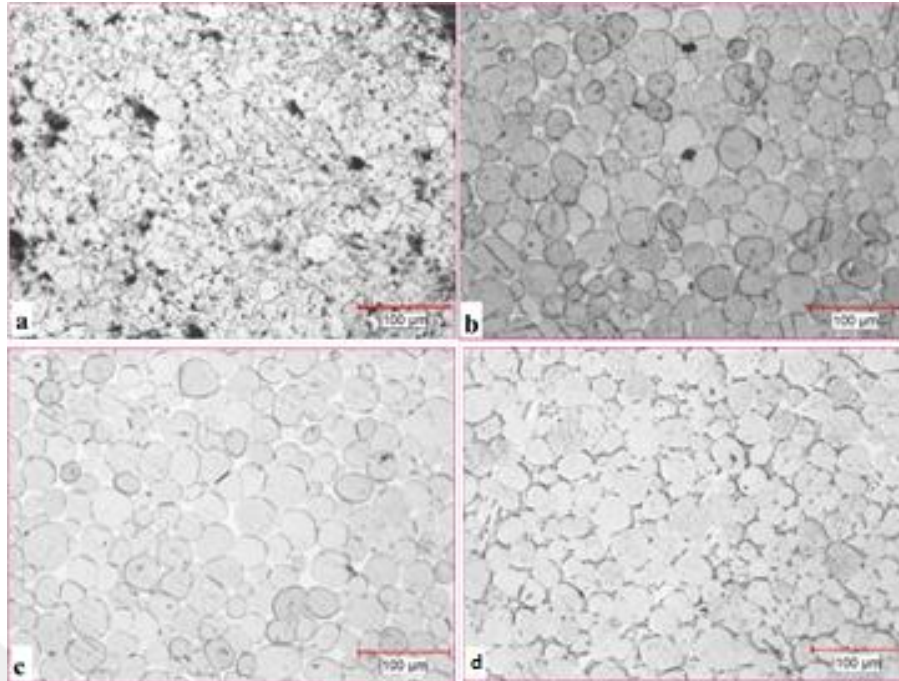
Figure 3.9 Microstructures of the sintered 0W1/1NC (a, b, c) and 5W1/1NC (d)
heavy alloys, (a:1450 ⁰C, b:1500 ⁰C, c and d 1550 ⁰C for 1 h., 200x).
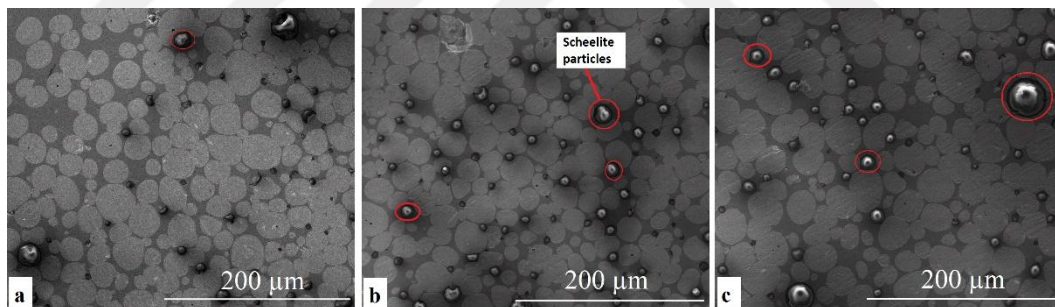
Figure 3.10 Microstructures of the W* or W** employed heavy alloys
(a:0W*41/NC, b:0W**4/1NC, sintered at 1500 °C, c:0W**4/1NC, sintered at
1550 °C).

However, larger and smaller size scheelite ($CaWO_4$) particles were observed in the
microstructures, as can be seen in Figure 3.10. They were located in the liquid phase
and coarsened under Ostwald-ripening mechanism during sintering treatment to
decrease surface free energy.

Microstructure images of 95 wt.% commercially available W contained heavy alloys are illustrated in Figure 3.11 and Figure 3.12, which were taken by back-scattered electron image (BEI) and secondary electron image (SEI) mode, respectively.
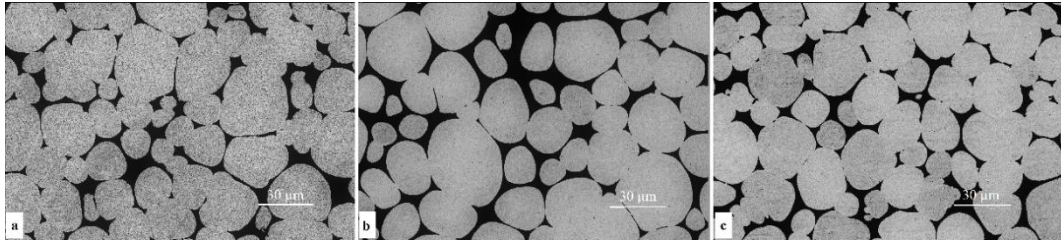
Figure 3.11 Microstructures of the 95 wt.% W contained WHAs (a:5W7/3NC, b:5W4/1NC, c:5W8/1NC), sintered at 1550 °C for 1 h., taken by BEI mode.
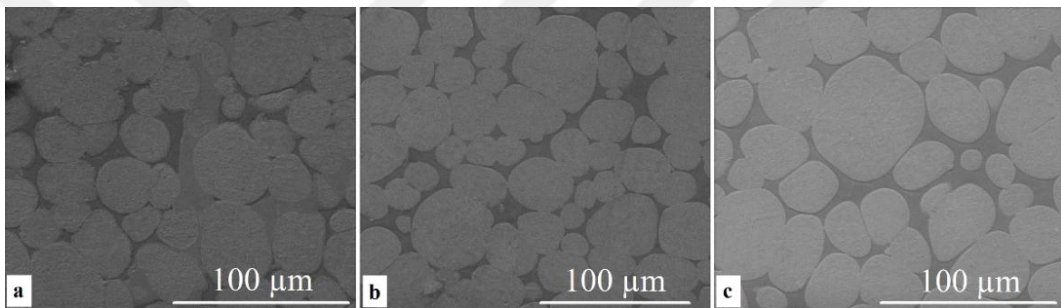
Figure 3.12 Microstructures of the 95 wt.% contained WHAs, (a:5W1/1NC, b:5W7/3NC, c:5W4/1NC), sintered at 1550 °C for 1 h., taken by SEI mode.

Formed microstructures are controlled by lots of parameters, including sintering temperatures, prepared mixture composition, and tungsten content [24]. Especially, sintering temperature and W content are two important factors. The effects of sintering temperature and W content on the final microstructures are illustrated in Figure 3.13. As can be seen in Figure 3.13, as the sintering temperature increased, the liquid can dissolve more W atoms, and hence the atomic motion was enhanced. Therefore, spheroidal final shape could be obtained. The phenomenon takes place to decrease the total system energy by the coalescence of smaller particles to form bigger particles. In addition, increased wt.% of W led to formation of contact flattened grain surface at 5W4/1NC heavy alloys. The transportation path might assist the tendency to achieve flattened grain surfaces from concave and/or convex particle curves.
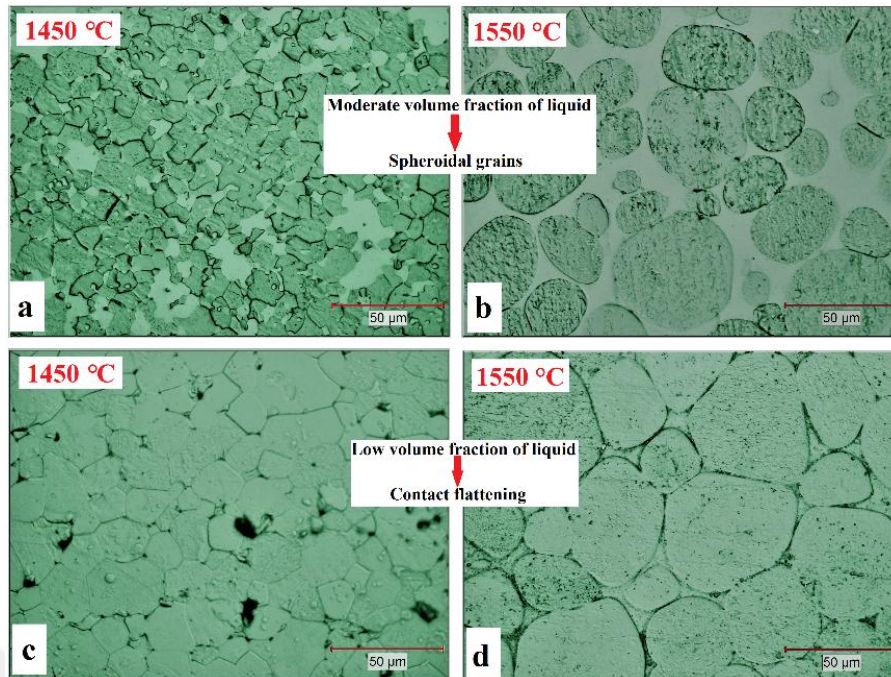
Figure 3.13 The effect of sintering temperature and W content on the microstructures (a and b from 0W4/1NC, c and d from 5W4/1NC).

3.1.3 Micro and Macro Hardness Tests

Two different hardness measurement methods were employed during mechanical property investigations. Micro scale hardness tests were performed to determine the hardness of binder phase and low densified alloys, whereas macro hardness tests were conducted to observe macro scale hardness variations. The measured hardness results of selected alloys are given Appendix D.

The effects of sintering temperature, W content, W type, alloying elements and their ratios on hardness were studied with various sintered compositions. The relation of the altered Ni/Co ratio and hardness is illustrated in Figure 3.14. As can be seen in Figure 3.14, Co-rich heavy alloys had the highest hardness values. As the Ni ratio increased, the hardness of 95 wt.% W contained alloys decreased, except from 8/1 Ni/Co added alloy. Although the other Ni/Co ratio employed alloys had relatively homogeneous hardness distribution, 1/1 and 7/3 Ni/Co added alloys demonstrated instabilities during measurements. It can be explained with reference to Ni-rich and Co-rich regional composition changes.
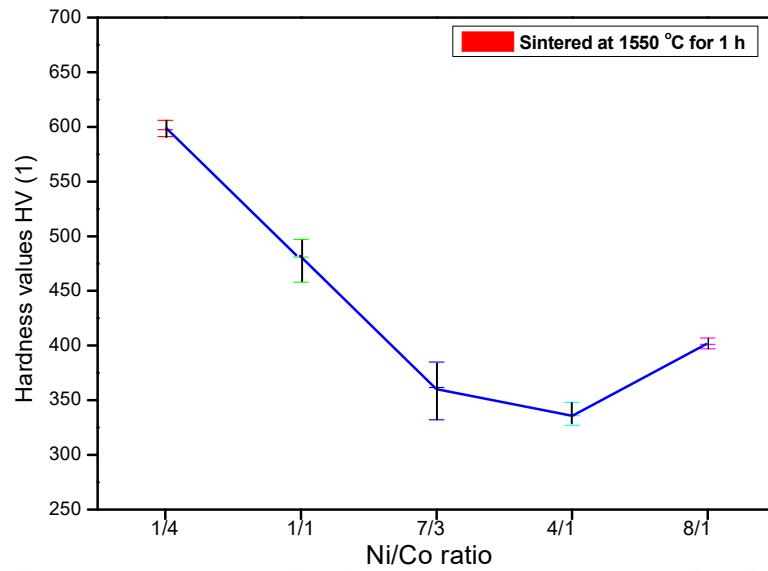
Figure 3.14 Hardness variations of the 95 wt.% W contained WHAs.

The effect of Ni/Co ratio on dissolved W wt.% in binder phase and microhardness values are illustrated in Figure 3.15.
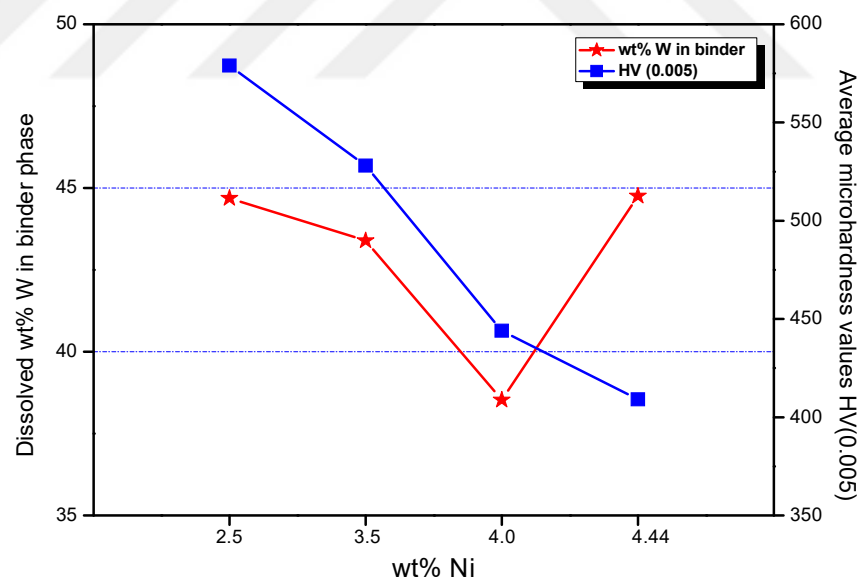
Figure 3.15 The effect of the Ni wt.% on W solubility and microhardness variation of 95 wt.% W contained heavy alloys, sintered at 1550 °C for 1 h.

As can be seen Figure 3.15, the average microhardness value of binder phases decreased with increasing wt.% of Ni. They demonstrate similar changes with W

solubility in binder, except from 0W8/1NC alloy. However, regular W solubility variation could not be observed in altered Ni content due to several interior and exterior factors, including especially sintering temperature, compositional variation, green density gradients [24].

Two-binder phase contained 0W1/1NC and 5W1/1NC alloys had wide composition and hardness differences. HV (0.005) microhardness test method applied microstructure image of 5W1/1NC is illustrated in Figure 3.16.
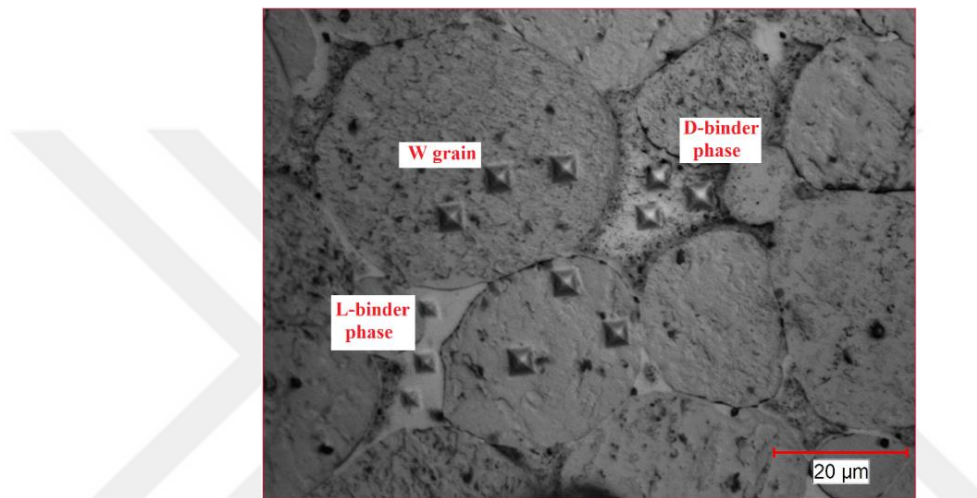
Figure 3.16 Regional hardness variations of the 5W1/1NC alloy, sintered at 1550 °C for 1 h.

Size of indentation may assist to compare the hardness variation in both binder phases and W grains. The light region seen in Figure 3.16 has approximately 75 wt.% dissolved W in binder phase and its hardness values change between 1200 and 2500 HV(0.005), whereas the dark region has nearly 40 wt.% dissolved W and its hardness results change between 444 and 672 HV(0.005) hardness variation. Minimum, maximum and average hardness results of selected alloys can be seen in Appendix D. Point EDS results of these binder phases are given in Figure 3.17.

In addition, the effects of W content and sintering temperature on hardness alternation of 0W1/1NC and 5W1/1NC alloys are demonstrated in Figure 3.18.
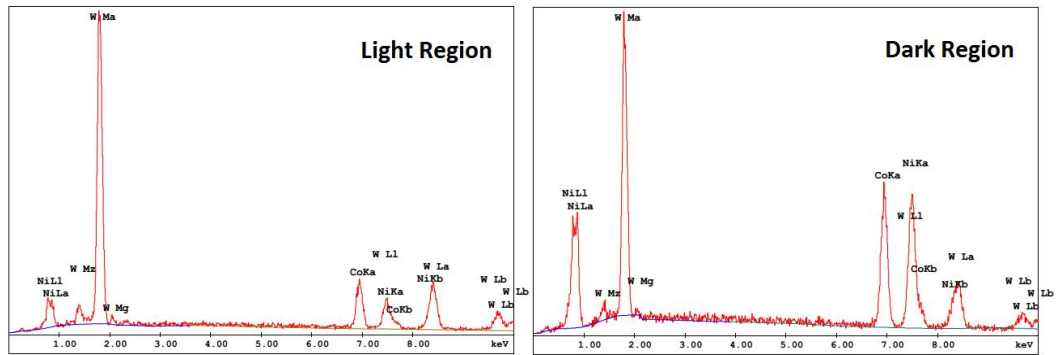
Figure 3.17 Point EDS results of the 5W1/1NC heavy alloy, sintered at 1550 °C for 1 h.
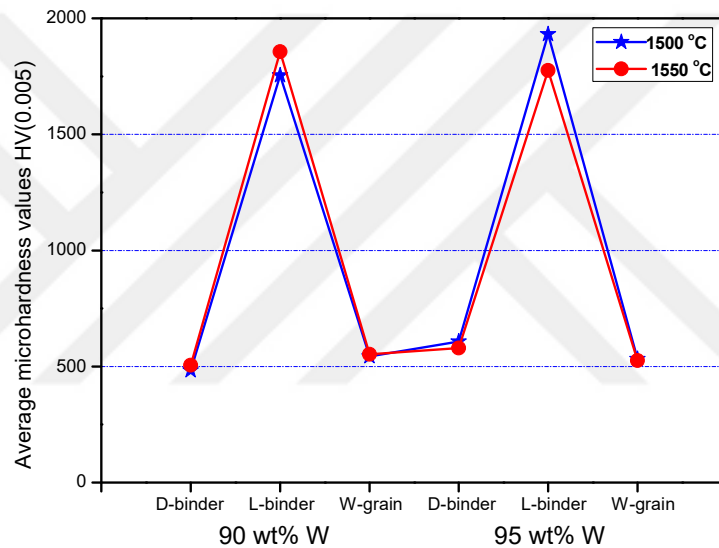
Figure 3.18 The effect of sintering temperature and W content on the hardness alternation of two-binder phase contained heavy alloys.

As can be seen in Figure 3.18, variation of W content and applied sintering temperature slightly influence the hardness of 1/1 Ni/Co added alloys. The variations are most probably resulted from dissolved W differences and W-Ni and/or W-Co intermetallic phase formation [24,37].

On the other hand, employment of the Ni and different suitable additive have great influence on sintered hardness values. In this context, the effects of Co and Fe alternation and W content on hardness values were investigated and the results are demonstrated in Figure 3.19.
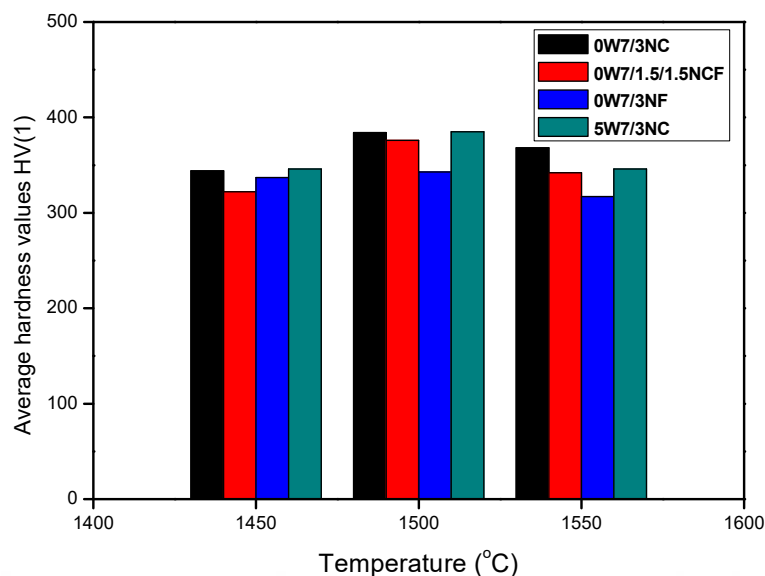
Figure 3.19 The effects of the Co and Fe alternation and W content on hardness.

As illustrated in Figure 3.19, employment of Fe powder instead of Co causes a decrease in hardness. In addition, increased W content influenced the sintered hardness. The differences are attributed to decrease in dissolved W in binder phase and relatively lower intermetallic phase formation in 5W7/3NC, compared to 90 wt.% WHAs.

The effects of employed tungsten powder type and sintering temperature on hardness are illustrated in Figure 3.20. As can be seen in Figure 3.20, except from 7/3 Ni/Co which was sintered at 1550 °C, both heavy alloy types demonstrated similar hardness variation with altered composition. In addition, WHAs had higher hardness than W*HAs at 1500 °C treatment, whereas W* powder employed heavy alloys had higher hardness values than WHAs at 1550 °C treatment. This can be explained with reference to insufficiently densified W*HAs. As the temperature increased, they could obtain more densified structures and their mechanical properties were improved. In addition, the impurities present in W* powder resulted from the production procedure might have caused the increment.

The effects of various Ni/Co ratios and Fe powder employment instead of Co on hardness variation were investigated via macro scale hardness measurements. The HRA results of 90 wt.% commercial W contained WHAs are illustrated in Figure 3.21.
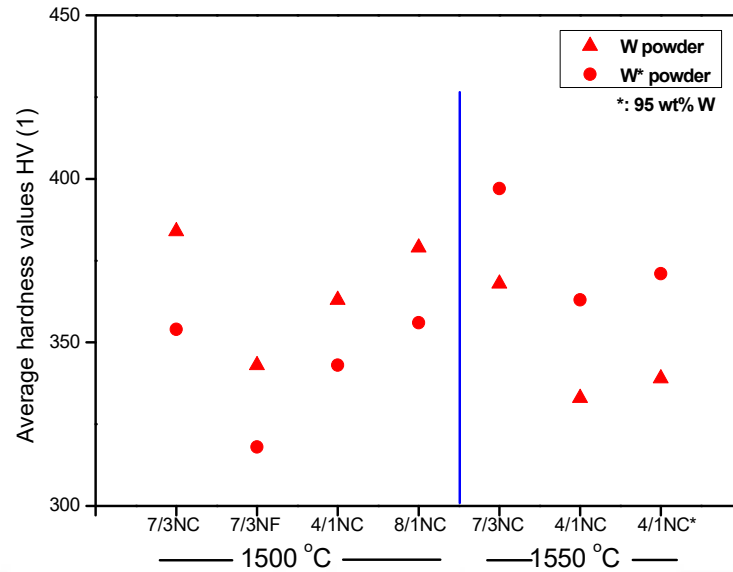
Figure 3.20 Average hardness results of the WHAs and W*HAs.
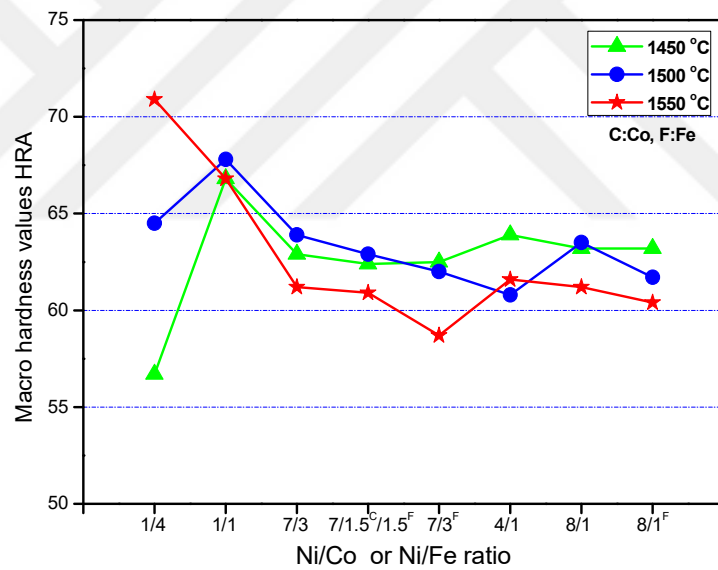
Figure 3.21 The effect of Ni/Co and Ni/Fe ratio on the hardness variations.

As can be seen in Figure 3.21, increased temperature and Ni/Co ratio did not have stable influence on hardness values. Co-rich and 1/1 Ni/Co added alloys have higher hardness values. The lowest hardness value of Co-rich alloy might have resulted from inadequately densified structure. As the sintering temperature increased, the alloy could reach the highest hardness value of all heavy alloys which is indicated in Figure 3.21.

Even though they could not demonstrate considerable densification behavior, Co-rich heavy alloys have relatively higher hardness values than Ni-rich alloys. In addition, they can sustain their hardness values at macro scale hardness measurement despite possessing high amount of porosity.

This is attributed to dissolved wt.% of W in binder phase. Point EDS composition results of each distinguishable binder phases are given Appendix E.

As the sintering temperature increased, the size of W grains increased. The increased grain size leads to spherical tungsten grain formation in binder phase and decrease in contiguity between the W grains [48]. The effect of diminished contiguity could not be distinguished in micro scale investigation. However, the macro scale hardness method can help to identify this phenomenon. Tungsten grains which had a decreased contiguity could not resist the applied loading and moved to the loading direction. Therefore, lower hardness values were observed during macro scale hardness tests.

The hardness values of studied alloys are mainly relied on formed phases between W/W* and added transition metals. XRD analyses were performed to understand the reason why Co-rich and 1/1 Ni/Co ratio heavy alloys have relatively higher hardness values than Ni-rich heavy alloys. The results are demonstrated in Figure 3.22.
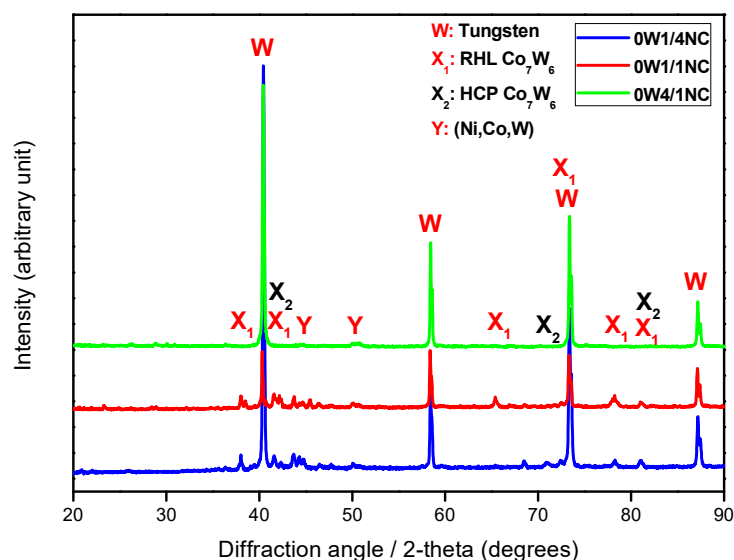
Figure 3.22 XRD analysis results of the 90 wt.% W contained WHAs, sintered at 1550 °C, for 1 h.

As can be seen in Figure 3.22, in Co-rich heavy alloys high amount of Co_7W_6 intermetallic phase was formed, which might be the reason for the increased hardness values. The phase had two different crystal structures, namely metastable hexagonal close-packed (HCP) and rhombohedral lattice (RHL) [49].

Even though 1/4 Ni/Co ratio contained heavy alloys possessed approximately 15-20% porosity, they could reach higher hardness values than WHAs, which are produced and employed in industrial, ordnance applications.

3.1.4 Average Grain Size and Grain Size Distribution Measurement Studies

Planimetric method was employed during average grain size (AGS) measurements. The calculated results for selected alloys are given in Appendix F. The effects of wt.% Ni content with altered sintering temperature are demonstrated in Figure 3.23.
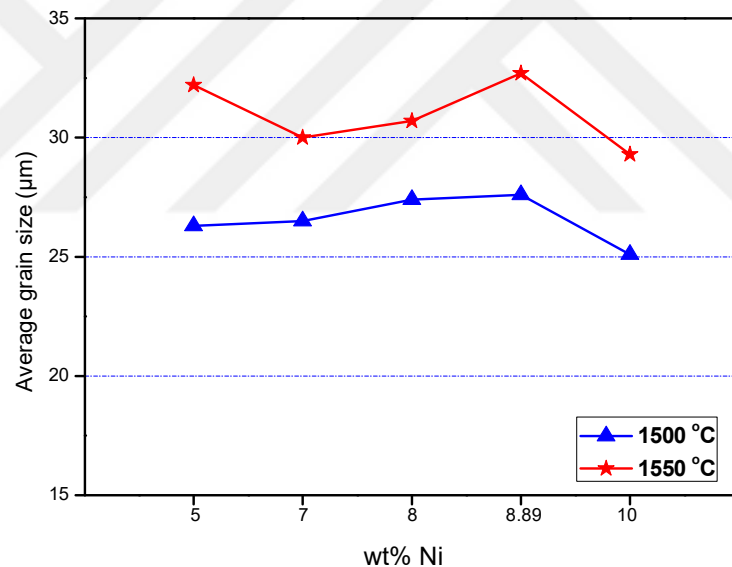
Figure 3.23 The effect of Ni amount on the average grain size of the 90 wt.% W contained alloys at different sintering temperatures.

As can be seen in Figure 3.23, as the sintering temperature increased, AGS of the studied alloys typically increased due to having more mobile atoms which also enhanced the mass transport in liquid. Moreover, as the amount of Ni increased, the average grain size of 90 wt.% W contained alloys mostly had a tendency to increase at both sintering temperatures. However, Co-free Ni added alloys had a relatively

lower AGS. This can be explained with density and AGS relation. 10 wt.% Ni added alloys had relatively lower AGSs and they also had low densified structures as given already in Table 3.1. Since densification is a mass transport mechanism which takes place from the interior of the particle to surface, grain growth phenomenon occurs inevitably [50].

Decreasing in total system energy and formation of more densified structures are strongly relied on this coarsening mechanism. The density and AGS relation can be seen clearly in Figure 3.24.
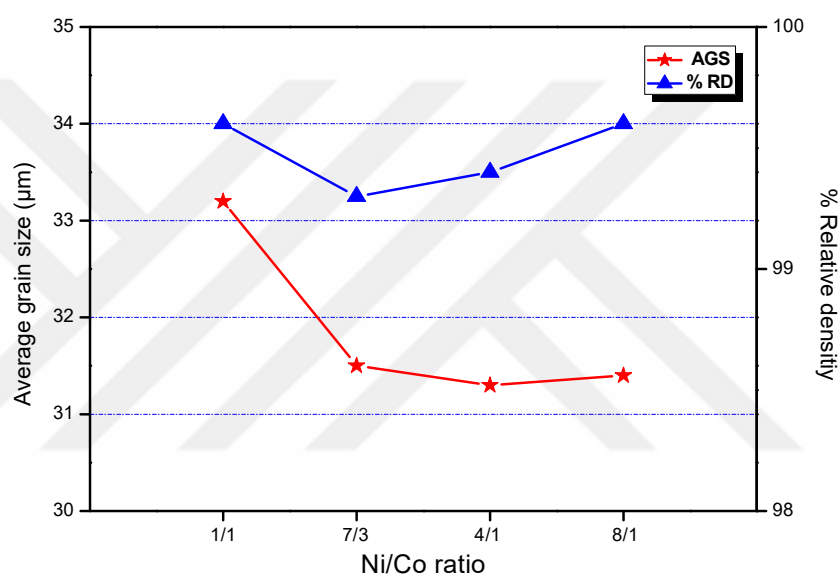
Figure 3.24 Grain size and relative density relation of the 95 wt.% W contained heavy alloys, sintered at 1550 °C for 1 h.

As illustrated in Figure 3.24, relative density and AGS of studied alloys generally increased with increased Ni amount except from 1/1 Ni/Co mass ratio, which had two binder matrix phases. Formation of relatively bigger AGSs and more densified sintered samples can be explained with the two binder matrix phases which had different W dissolving capacity.

The AGS variations of both W and W* powders with composition are demonstrated in Figure 3.25. As illustrated in Figure 3.25, W* powder employed heavy alloys had relative small AGSs with different Ni/Co and Ni/Fe ratios. It is attributed to following situations.
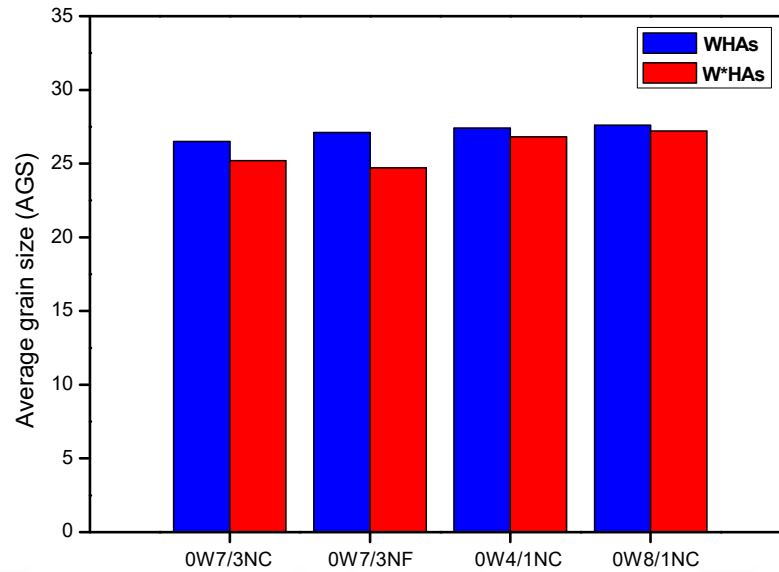
Figure 3.25 The effect of employed tungsten type on the average grain size of the heavy alloys, sintered at 1500 °C for 1 h.

Firstly, the initial grain size of W* powder was relatively lower than commercial W powder. Secondly, the grain boundary motion was believed to be prevented by $CaWO_4$ grains which were found in W* powder as a result of the processing procedure. The Ostwald ripening mechanism was observed not only for W* but also for $CaWO_4$ particles. Undissolved $CaWO_4$ was pushed through the grain growth direction and gathered in the liquid phase. Furthermore, the dissolved and/or precipitated contamination could have retarded the dissolved W atom motion in liquid leading to relatively smaller AGS formation.

Grain size distributions of the selected alloys were measured to determine the effects of sintering temperature, employed tungsten type, additive type and additive ratio on GSD. The homogeneity of the structure has a significant influence on mechanical properties.

The effect of sintering temperature was investigated with single additive heavy alloys. Grain size range vs. number of W grains graph is illustrated in Figure 3.26. As can be seen in Figure 3.26, increased sintering temperature typically augmented the grain growth tendency of the studied alloy. It is attributed to enhanced solid solubility and atomic motion.
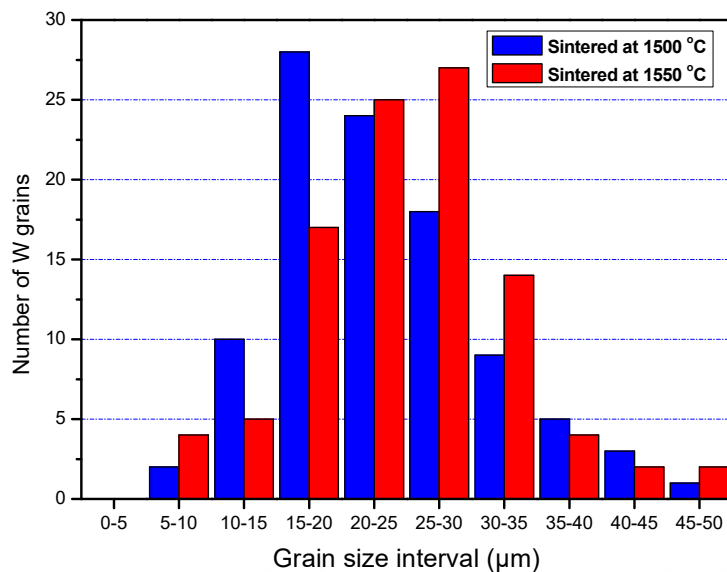
Figure 3.26 Grain size distribution of the Ni added 0W10N heavy alloys.

Therefore, more effective Ostwald-ripening mechanism took place during sintering. Although the mean grain size of 0W10N alloy, sintered at 1500 °C for 1 h, was 25.1 μm, 50 °C temperature increase lead to approximately 10 % growth of mean grain size and hence, it could reach up to 29.3 μm average diameter.

The effect of the Co and Fe alternation were also investigated to observe the grain size distribution. The measured grain size intervals are illustrated in Figure 3.27.

As can be seen in Figure 3.27, Co employed heavy alloys lead to coarser grain formation. 0W7/3NC alloy possessed coarser W grains which could reach up to 60-65 μm diameter. It was attributed to improved solid solubility in liquid [51] and decreased liquid volume. The last parameter decreases the distance between W grains, which facilitated the mass transport mechanisms [24].

The effects of tungsten content and employed tungsten powder type on grain size distribution are demonstrated in Figure 3.28 and Figure 3.29, respectively.

As can be seen in Figure 3.28, 95 wt.% W contained heavy alloy has higher grain growth tendency than 0W7/3NC. It can be explained with decreased distance between W grains.
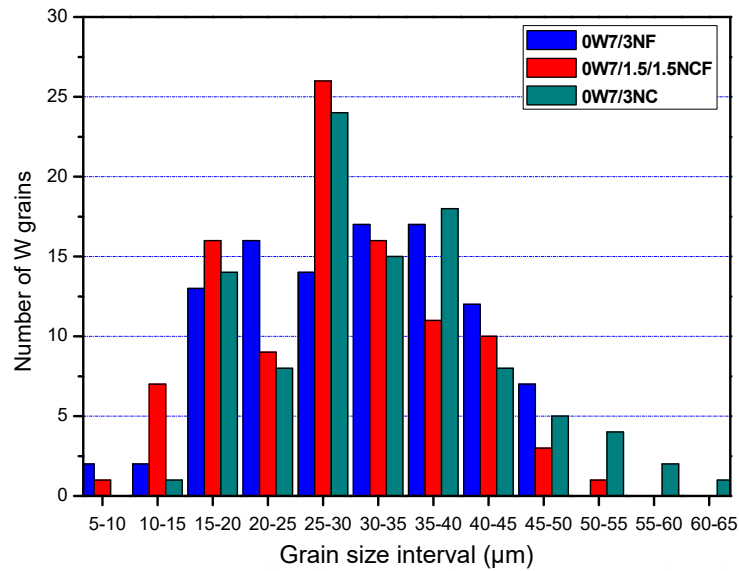
Figure 3.27 The effect of Co-Fe shifting on grain size distribution, sintered at 1550 °C for 1h.
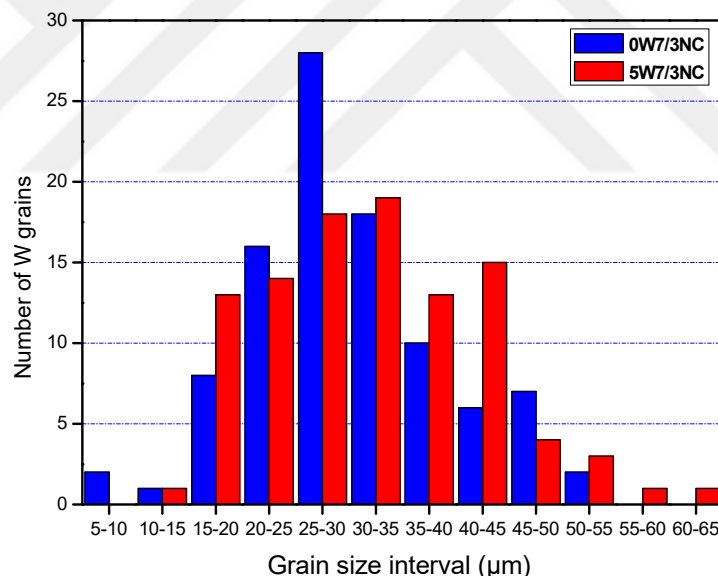
Figure 3.28 The effect of W content on grain size distribution, sintered at 1550 °C for 1 h.

As for Figure 3.29, W powder employed heavy alloy indicated relatively homogeneous grain size distribution. In addition, its average grain size was relatively coarser than 5W*4/1NC alloy.
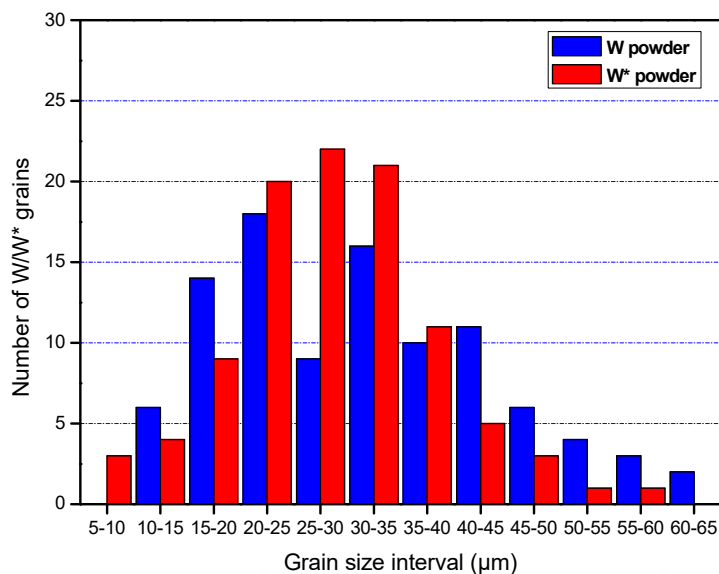
Figure 3.29 Employed tungsten powder type and grain size distribution relation of the 5W4/1NC and 5W*4/1NC alloys, sintered at 1550 °C for 1h.

Both situations can be explained with high amount of liquid phase formation in 5*W4/1NC alloy. The high liquid volume decelerated the grain growth rate by increasing the distance between solution and precipitation regions. Furthermore, the GSD variation can be resulted from initial particle size differences. W* powder had a smaller initial particle size than W powder.

3.1.5 Dissolved W or W* Powder in Binder Phase

Compositions of selected binder phases were determined with point EDS analyses. The investigations are aimed to set a correlation between solubility and densification as well as micro and macro hardness results. Performed EDS analyses are given in Appendix E. Furthermore, line EDS analyses were also applied to investigate the composition variation between two W grains. One of the line analysis and corresponding composition are demonstrated in Figure 3.30.

As can be seen in Figure 3.30 , two-phase binder matrix contained 0W1/1NC alloy indicated wide dissolved W variation between its binder phases. The dark region had approximately the same dissolved W in binder like Ni-rich heavy alloys; whereas, the light region could dissolve about 75 wt.% W in binder like Co-rich and Co-Fe added heavy alloys.
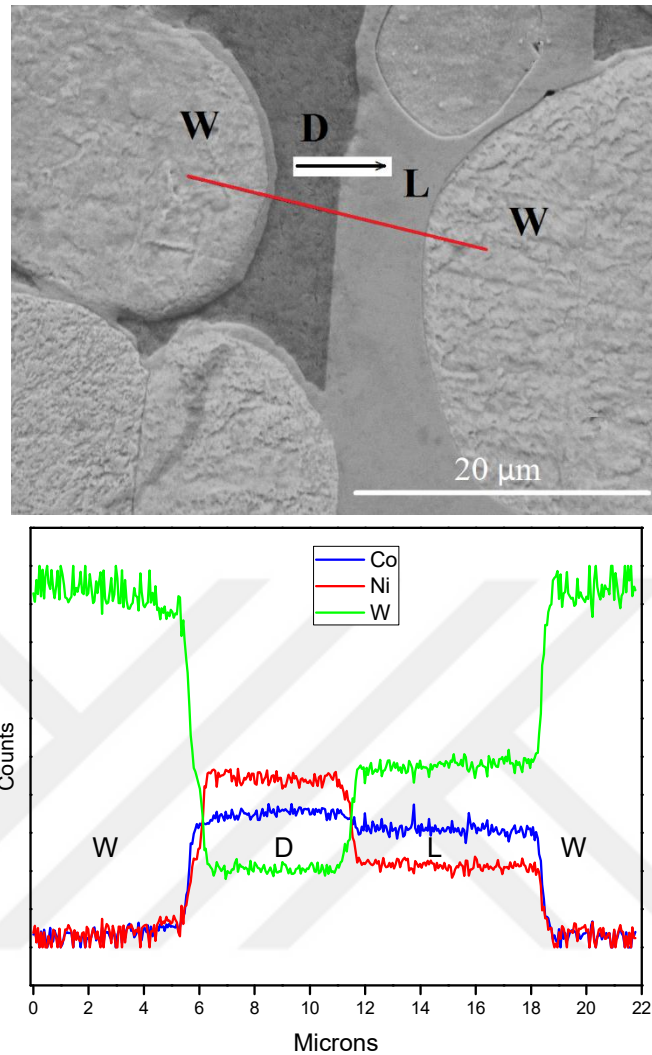
Figure 3.30 Line EDS measurement of the 5W1/1NC, sintered at 1550 °C for 1 h (W:W grain, D:Dark region, L:W-rich light region).

The compositional variations of these three different phases are schematically indicated by ternary phase diagram of W-Ni-Co alloy which is given in Figure 3.31. As can be seen in Figure 3.31, sintered 5W1/1NC alloy consisted of three different regions: pure W grains, light and dark color regions. As the sintering temperature increased, the dissolved W in both phases also increased. The EDS results of three regions are given in Table 3.2. This two-phase binder matrix was observed in both 0W1/1NC and 5W1/1NC heavy alloys which sintered at 1500 °C and 1550 °C for 1 h. Compositional contrast image of 0W1/1NC alloy is given in Figure 3.32. Density differences, in other words, dissolved W distribution and W grains can be distinguished clearly.
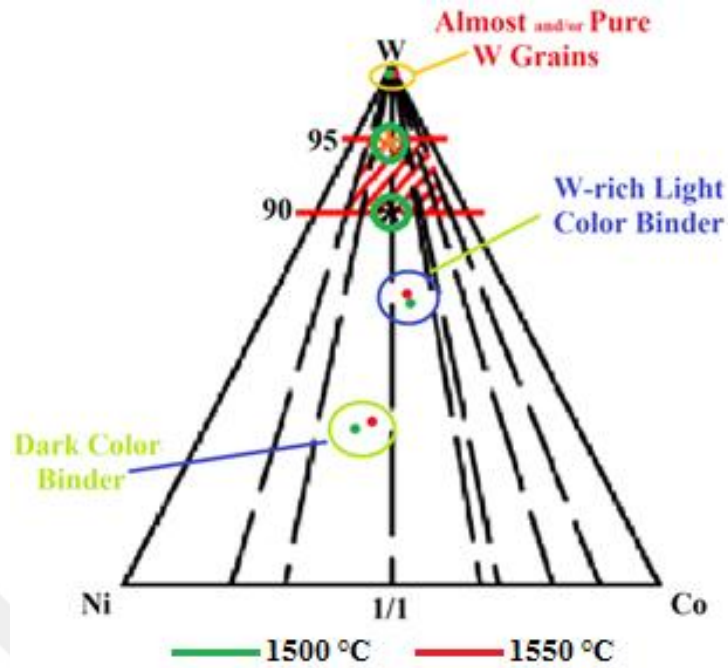
Figure 3.31 Schematic appearance of regional and general compositional variation of the 5W1/1NC alloy.

Table 3.2 EDS analysis results of the 0W1/1NC and 5W1/1NC at different sintering temperature.

		Temperature (°C)					
		1500			**1550**		
Composition	**Phase**	**W (wt.%)**	**Ni (wt.%)**	**Co (wt.%)**	**W (wt.%)**	**Ni (wt.%)**	**Co (wt.%)**
0W1/1NC	Dark	41.38	34.46	24.16	43.64	32.71	23.65
	Light	73.16	11.21	15.63	74.08	10.73	15.19
5W1/1NC	Dark	42.67	34.42	22.91	44.69	29.32	25.99
	Light	73,52	10.75	15.73	74.27	10.43	15.30
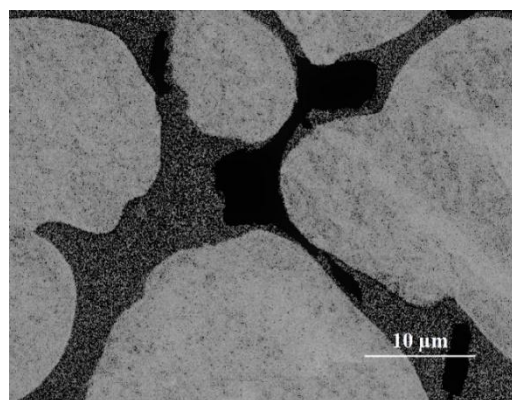
Figure 3.32 Microstructure of the two-binder phase contained 0W1/1NC heavy alloys sintered at 1550 °C for 1 h, taken by BEI mode.

As can be seen in Table 3.2, light binder phase consisted of mainly rhombohedral Co_7W_6 intermetallic phase [47]. In addition, the phase contained approximately 10 wt.% Ni. It was probably the result of substitutional diffusion between Ni and Co. On the other hand, the dark phase was composed γ solid solution which had face-centered cubic Ni-Co-W phase [47].

Another line EDS measurement was performed to investigate the compositional homogeneity of the sintered sample. Since pre-sintering parameters have a great influence on the sintering behavior, single binder matrix phase contained 5W4/1NC alloy was also examined with line EDS analysis method. The analysis line and its constituents are illustrated in Figure 3.33. As can be seen in Figure 3.33, the compositional variation of 5W4/1 alloy was considerable uniform. Therefore, it can be concluded that mixing procedure was highly effective to obtain targeted compositions.

When Appendix E and two-binder phase results are considered, the amount of solid solubility in liquid phase is slightly influenced with altered sintering temperature and time. However, the employed additive elements and their ratios had a great effect on solubility, and hence, densification behavior.

In this context, various Ni/X ratio (X:Co, Fe) were studied. The effect of Co and Fe variation, increased Ni ratio, W content and sintering temperature on W solubility in liquid are demonstrated in Figure 3.34. As can be seen in Figure 3.34, employment of Co instead of elemental Fe increased the W solubility in the formed liquid phase. It can be explained with electron concentration concept [52]. Transition metals, possessing d electron subshells, demonstrate more effective W solubility. Co is closer to mentioned subshell groups (Ni, Pd and Pt) than Fe. In addition, when the binder phase composition of the 0W7/3NF and 0W8/1NF heavy alloys compared, the increased Ni ratio also augmented the amount of dissolved W in matrix phase.

On the other hand, increased W content and sintering temperature did not indicate a regular correlation with W solubility. Since using high sintering temperature causes grain coarsening, it should not be preferred at sintering treatments.
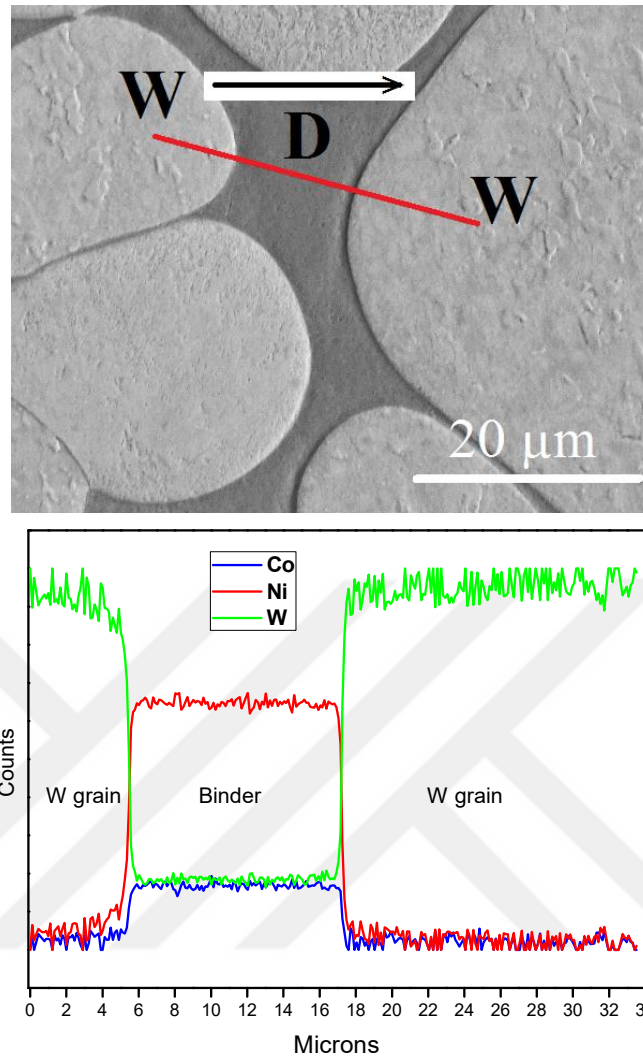
Figure 3.33 Compositional variation of the 5W4/1NC heavy alloy, sintered at 1550 °C for 1 h.

The effects of employed tungsten types on dissolved tungsten in binder phase were also studied. The impurities of W* powder were ignored to obtain more appropriate data for comparison. The Ca, Cr, Mo Fe for Ni/Co alloys were intentionally removed from the result lists if they were detected in trace amounts during the point EDS analysis. The effects of powder fabrication method and initial powder characteristics such as particle shape, particle size and purity, on solubility are demonstrated in Figure 3.35 with various Ni/Co and Ni/ Fe ratios. As can be seen in Figure 3.35, except from 7/3NF, W powder employed heavy alloys demonstrated relatively higher dissolved W in their binder phase. This is attributed to particle shape and particle size distribution of W* powder.
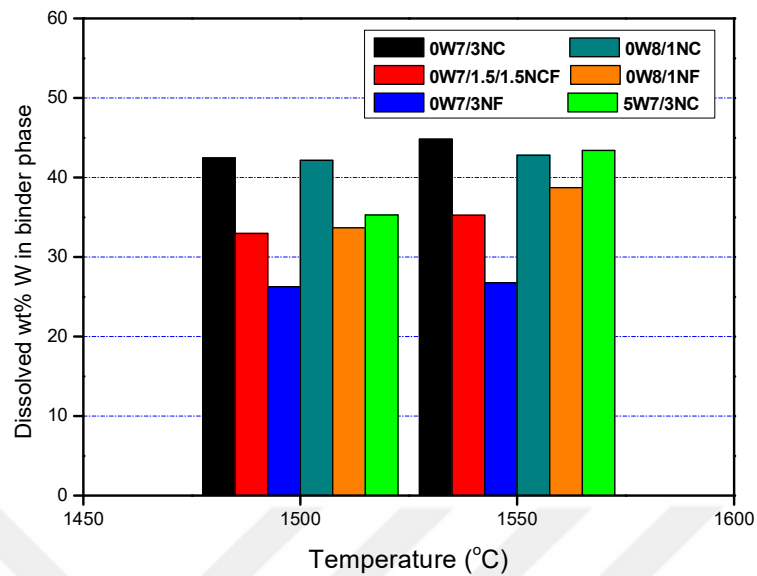
Figure 3.34 The effect of altered parameters on dissolved wt.% of W, sintered
for 1 h.

The size distribution of the W* powder was relatively homogeneous than commercial
powder which has 1-5 µm size variation. As the size differences increase, the solubility
tendency of small W powder also increases due to enhanced higher energy.
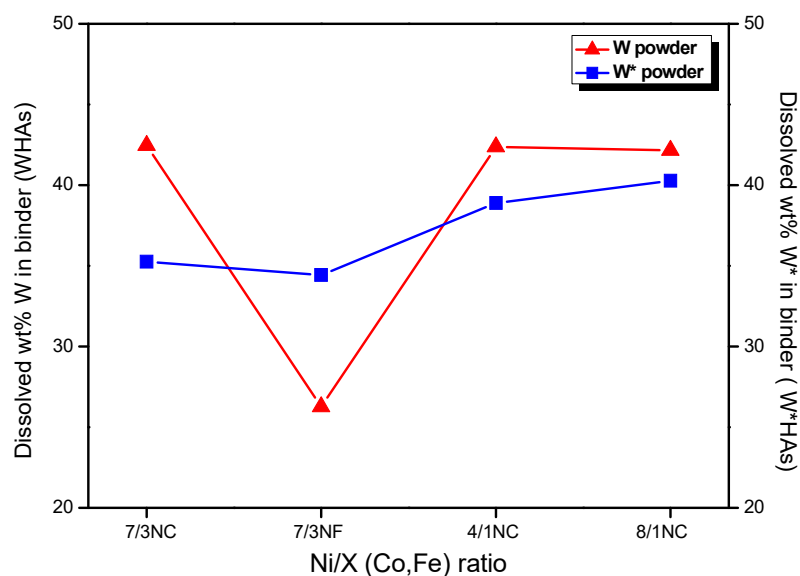
Figure 3.35 Dissolved wt.% of W and W* in binder matrix phase, sintered at
1500 °C for 1 h.

Therefore, more dissolved W could be observed in binder phase of the investigated WHAs. The impurity contents of the W* powder was also an important parameter for the decreasing. The impurities might have decreased the dissolving capacity of the liquid phase by forming compounds with Ni, Co and/or Fe. Especially when the amount of free Ni decreased in formed liquid phase, expected tungsten solubility, transportation and precipitation may not be provided during sintering treatments.

In brief, the binary and ternary interactions of studied alloys and W solubility in employed additives play a crucial role in determining the amount of dissolved W wt.% in binder matrix phase. The variation of dissolved W amount and other constituents, which are not demonstrated here, can be seen in Appendix E.

3.1.6 Binder Phase Area Measurements

Binder phase area (%) of studied alloys is a crucial parameter to understand the underlying causes of sintered density, final grain shape and size as well as shape distortion phenomenon.

Suitable BEI, SEI and OM images were employed during measurements. At least seven measurements were taken from each selected specimen; two from the top, and three from the interior and two from the bottom. Binder phase area of selected alloys were measured via ImageJ software. The microstructure images were uploaded to the software and the color threshold adjusted to obtained two different colored regions, and hence binder phase areas could be calculated. Measured minimum, maximum and average values are given Appendix F.

Images from % binder phase and % CaWO4 area calculation are given in Figure 3.36 and Figure 3.37, respectively.

Binder phase area percent of selected WHAs are illustrated in Figure 3.38. As the sintering temperature increased from 1500 to 1550 °C, binder phase area also typically increased due to enhanced solubility and higher diffusion rate. Both of them enhance the solution and re-precipitation mechanism during sintering. Therefore, relatively coarser W grains formed in binder phase matrix.
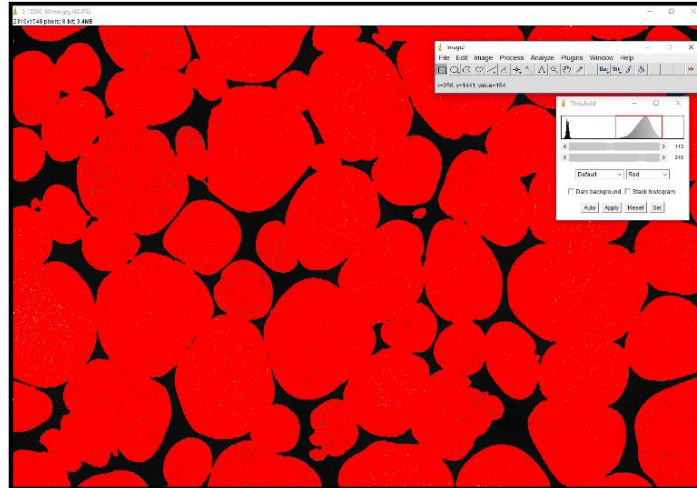
Figure 3.36 An image from % binder phase area calculation procedure (ImageJ).
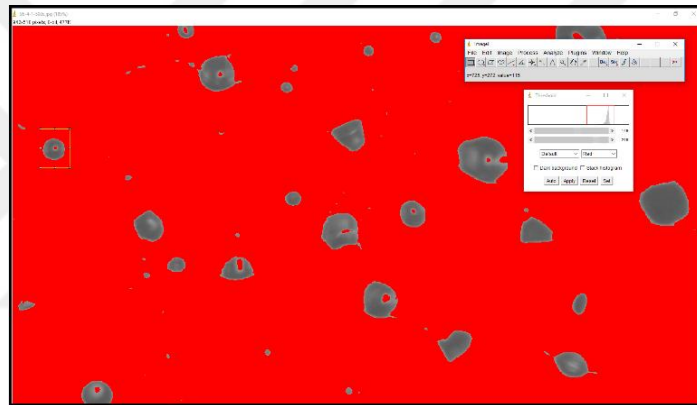
Figure 3.37 An image from % CaWO$_4$ area measurement procedure (ImageJ).

Employment of Fe instead of Co, lead to higher binder area formation. It can be explained via theoretical density differences between the powders.

Effect of Ni amount on binder phase area variation is illustrated in Figure 3.39. As can be seen in Figure 3.39, binder phase area of investigated alloys increased with an increase in Ni amount. It can be explained with reference to high tungsten solubility tendency in Ni-rich binder phase.

The % binder phase area variation of selected WHAs and W*HAs are demonstrated in Figure 3.40.
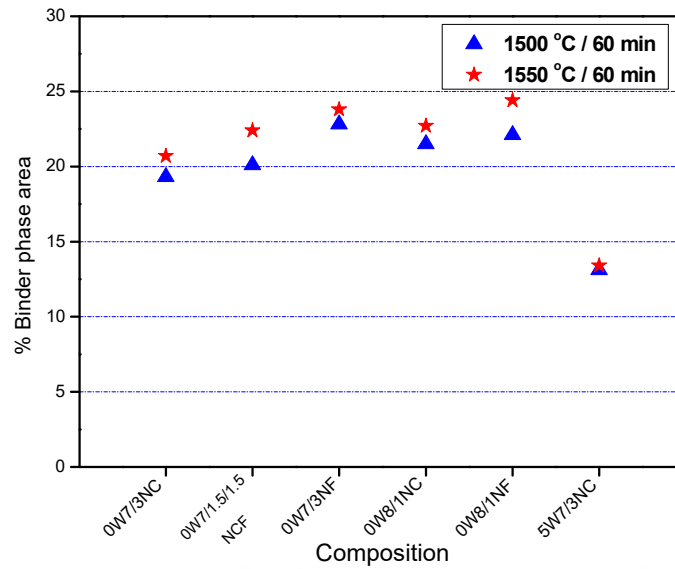
Figure 3.38 Variation of binder phase area of the WHAs with W content, different alloying elements and sintering temperatures.
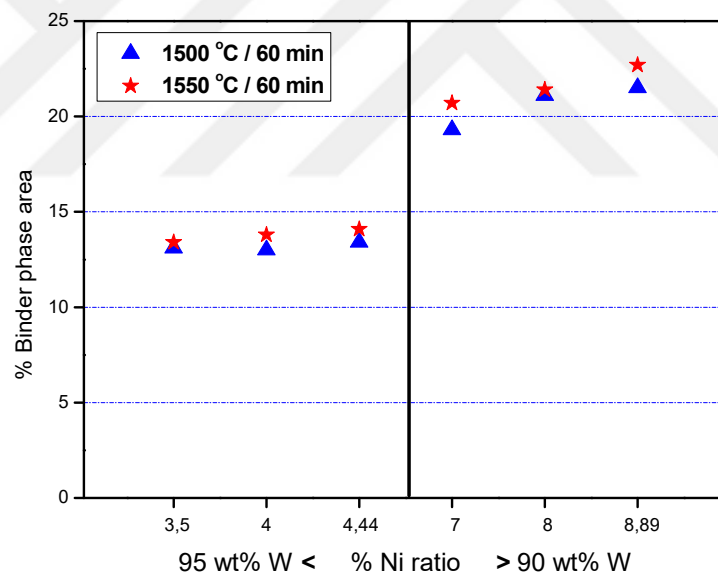
Figure 3.39 The effect of the Ni amount at different W contents and sintering temperatures on binder phase area.

As can be seen in Figure 3.40, W* powder employed heavy alloys had higher binder phase area than WHAs. The phenomenon is attributed the impurity content of W* powder.
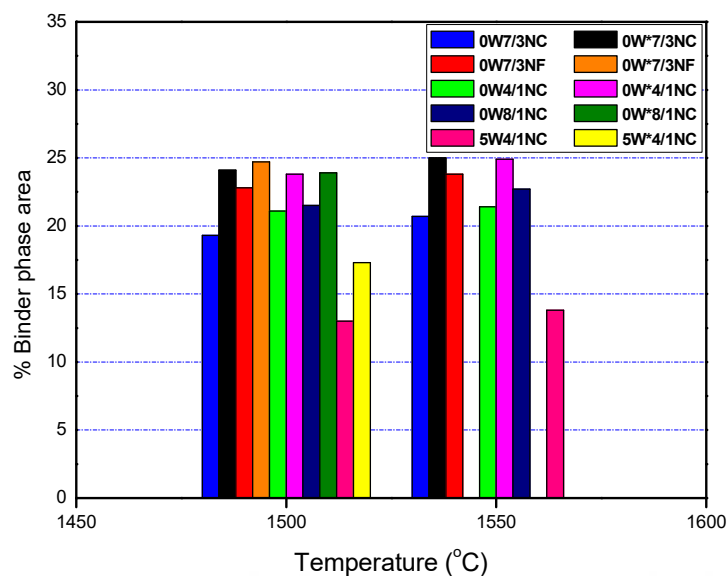
Figure 3.40 % Binder phase area variation of the WHAs and W*HAs.

Since tungsten can only dissolve negligible amounts of, the studied elements in its structure, the impurities merged into formed liquid phase, so the volume of the liquid phase increased [24].

In addition, $CaWO_4$ particles present in W* powder was important for the binder phase area measurements, which demonstrated wide $CaWO_4$ area variation in cross direction of diameter. They could reach up to 6 % of total measured area at top of the specimens. However, as the measured region decreased from top to bottom, % $CaWO_4$ area of W*HAs also decreased due to its density, 5.9-6.1 g/cm^3 [8]. The phenomenon can be explained with density differences between the scheelite particles and binder phase which has approximately 9-10 g/cm^3 density [53]. Therefore, scheelite particles typically were floating in liquid phase at sintering conditions.

When the wt.% Ni and wt.% W content were employed as variables, the effects of measurement region on binder phase area are illustrated in Figure 3.41. As can be seen in Figure 3.41, solid segregation was observed in studied alloys. Top of the specimens had approximately 87-88 wt.% W containing microstructure; whereas, bottom of the specimens had nearly 91-92 wt.% W included sintered microstructure for 90 wt.% W contained WHAs.
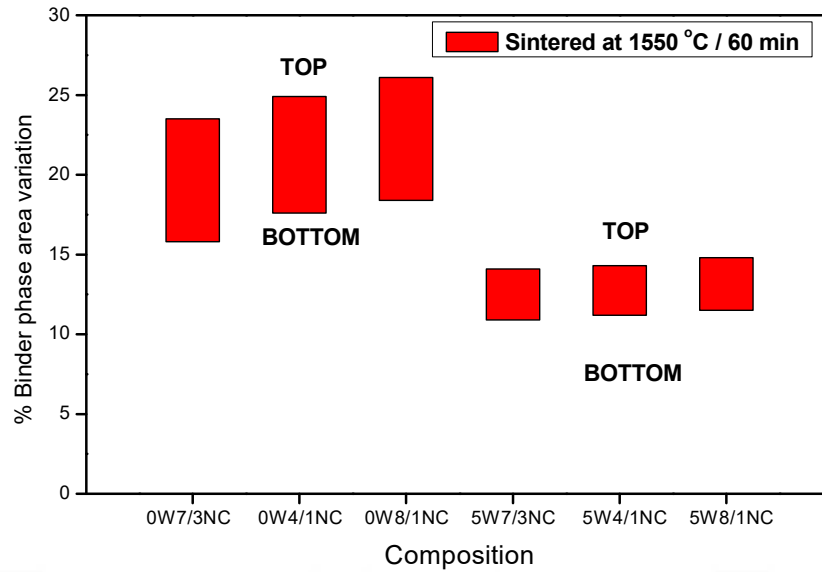
Figure 3.41 The effects of the wt.% Ni and wt.% W content on regional binder area variation.

Even though the difference was relatively lower, similar behavior was also observed in 95 wt.% W contained alloys. An OM image, taken from 0W7/1.5/1.5NCF heavy alloy, showing the segregation is illustrated in Figure 3.42.
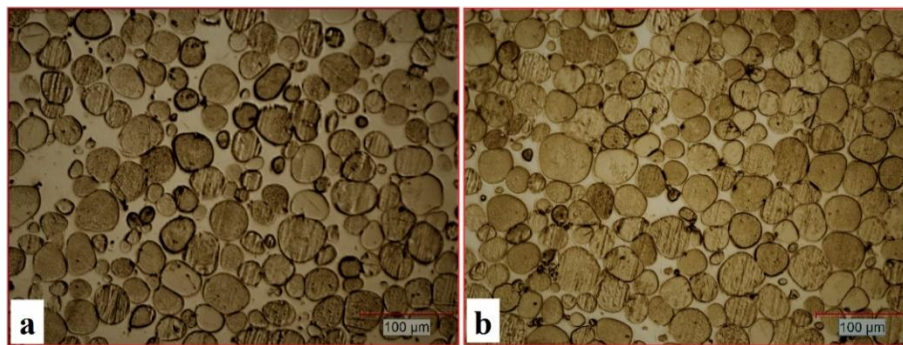
Figure 3.42 Solid segregation of W grains in 0W7/1.5/1.5NCF heavy alloy, sintered at 1550 °C for 1 h (a:top, b:bottom).

W*HAs had higher binder phase content as mentioned above. The binder phase volume is an important parameter for final microstructure and shape distortion. In addition, possible unexpected phase formation in W*HAs should be investigated.

Within this framework, XRD analyses were performed to demonstrate phases and compare their binder phase content. The XRD analysis results of 0W7/3NC and 0W*7/3NC are indicated in Figure 3.43.
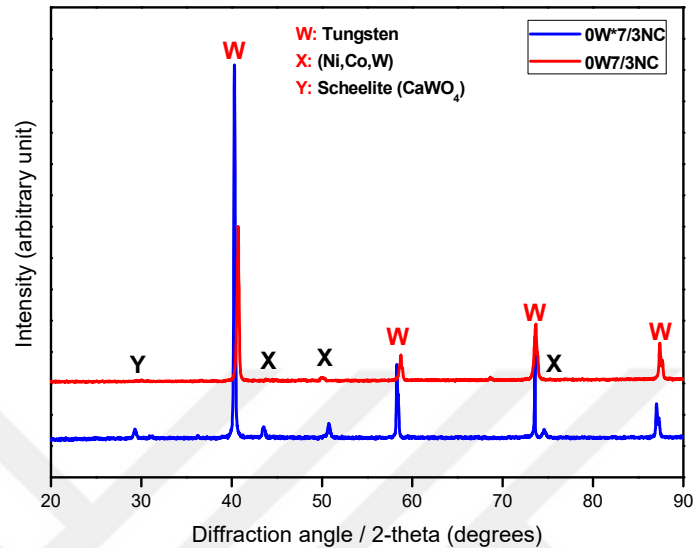
Figure 3.43 XRD analysis results of 90 wt.% W and W* powder contained heavy alloys, sintered at 1500 °C for 1 hour.

As can be seen in Figure 3.43, when the length of main tungsten peaks are considered, binder matrix phase ratio in W*HAs is higher than WHAs. Therefore, mentioned lower AGS and higher binder phase area were inevitably occurred in sintered W*HAs. Measured binder phase percentage results of each studied composition is given Appendix G.

3.1.7 Shape Distortion Investigation Studies

Various WHAs and W*HAs were investigated to understand the shape distortion behavior of selected alloys. Both tungsten powders, W content, Ni/X (Co,Fe) variation and sintering temperature were used as variables. Green and sintered dimensions of alloys were measured by a hook model digital caliper ($\pm$ 0.001 mm precision). And then, normalized height (h/h_o) and radius (r/r_o) were calculated according to Eq. 2.6.

The images of various sintered WHAs and W*HAs are illustrated in Figure 3.44.
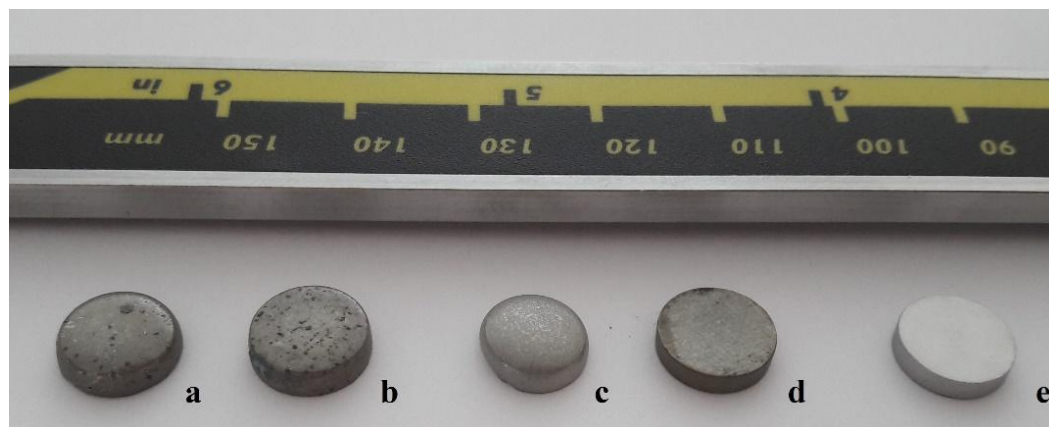
Figure 3.44 Images of the sintered WHAs and W*HAs (a:0W*7/3NC,
b:0W*7/3NF, c:0W7/3NC, d:0W7/3NF 1500 °C / 60 min, e:5W7/3NC 1550 °C
/ 60 min).

As can be seen in Figure 3.44, samples a and b, which were prepared by W* powders
could not be prevented their initial green compact shape due to higher liquid content
than W powder employed WHAs. The data can be seen in Appendix F. Although
some shape deformation (0W7/3NC) was observed in sample c, sample d (0W7/3NF)
could preserve its initial shape at the same sintering conditions (seen in Figure 3.44).
This was attributed to enhanced tungsten solubility in liquid phase by the addition of
Co instead of Fe [32]. The strength of W-W solid skeleton, formed at initial stage of
LPS, decreased lower than critical W-W contiguity value (C_{SS}<0.38) [43]. Therefore,
0W7/3NC alloy could not protect its prepared shape. However, 95 wt.% W contained
5W7/3NC alloys could preserve their initial shape even at 1550 °C. The calculated
normalized height and radius variation of selected alloys are illustrated in Figure 3.45.

As can be seen in Figure 3.45, W powder employed WHAs had approximately 0.8 as
the normalized height and radius, which also demonstrated about 20 % shrinkage.
However, 0W7/3NC and 0W*7/3NC alloys indicated shrinkage and swelling behavior
at the same time. It was referred to employment of H_2 gas in sintering treatments which
sometimes may cause swelling at vertical direction [54].
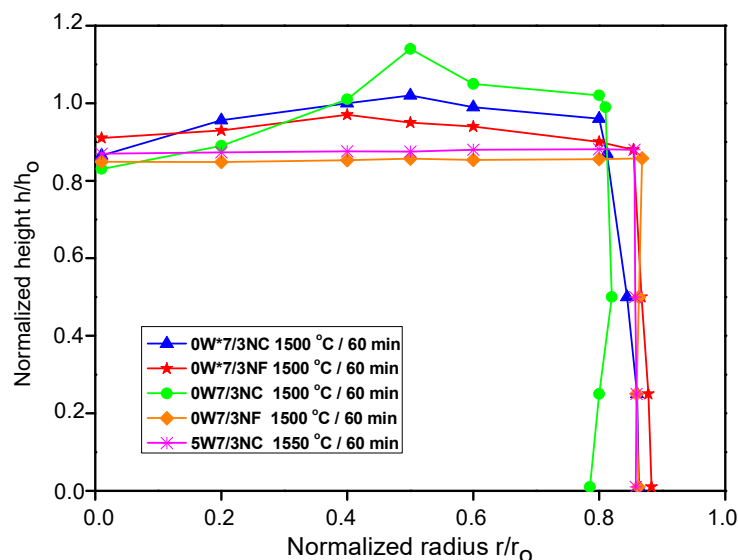
Figure 3.45 The effects of the W content, additive type on shape distortion.

3.2 Further Studies with W Powders

The studies are aimed to obtain further data to better understand the sintering behavior of commercial tungsten powder. The conducted studies can be collected under three main titles which are single additive employed WHAs, Ni-free Co-Fe heavy alloys and studied other sintering variables such as applied compression pressure, sintering atmosphere, etc. The results of conducted studies are represented in following titles.

3.2.1 Single Additive Employed Heavy Alloys Studies

Transition metals such as Ni, Co, Fe and other are mostly used activated sintering treatments [55], but single form of this powder have not been widely used in LPS. The conducted single additive studies were aimed to investigate the effects of Ni, Co and Fe addition on densification behavior and hardness.

Densification parameters of studied 90 wt.% W contained alloys were already illustrated in Figure 3.1. As can be seen the figure, Ni is most effective additive in all treatments. Ni added compacts could reach higher than 90 % relative density (RD) at 1450 °C sintering treatment, whereas Co or Fe added compacts could not reach higher than 90 % RD even at 1550 °C for 90 min. It is attributed to solid solubility properties

of these elements and binary phase diagram of W and additive metal. The phase diagrams of W-Ni, W-Co and W-Fe are given Appendix C.

The effects of employed additive on relative density and hardness are demonstrated in Figure 3.46.
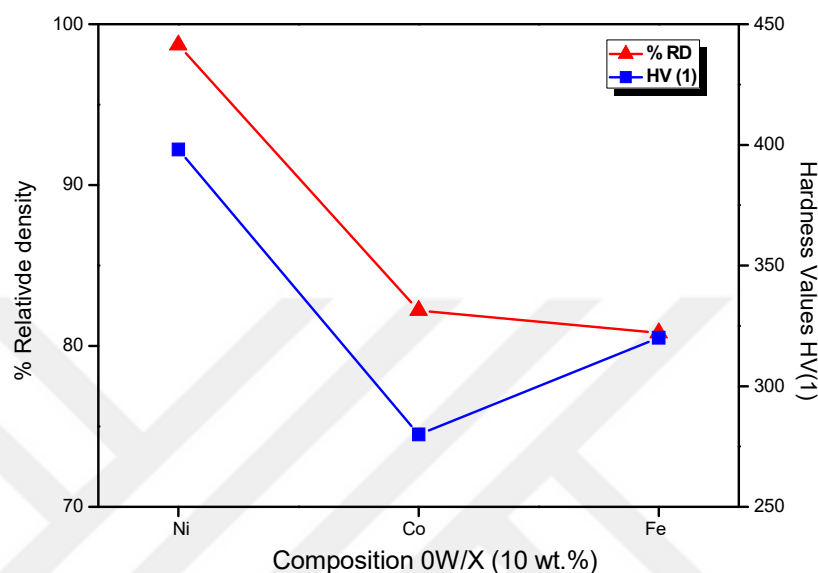
Figure 3.46 Relative density and hardness variation of the WHAs dependent on altered additives, sintered at 1550 °C for 1 h.

As can be seen in Figure 3.46, employment of Ni not only leads to high densified specimens, but also provides the harder sintered pellet. The densification differences can be explained with wt.% W in binder phase.

Elemental Ni can dissolve approximately 40 wt.% W in its structure, but Co and Fe can dissolve 35 wt.% and 33 wt.%, respectively [56]. The dissolved wt.% W in Co and Fe indicates sharp reduction with decreased sintering temperature, but Ni-W phase diagram has relatively low decreasing in solubility with descending temperature.

On the other hand, Co and Fe added alloys formed an intermetallic phase, which has Co_7W_6 and Fe_7W_6 formula. The point EDS results, given in Appendix E, demonstrate that the formed intermetallic phases contain approximately 73-75 wt.% W in their structure. Although they have higher dissolved W, they could not densify like Ni added alloys due to formed solid phase during sintering temperature. When the binary phase

diagram of Co-W and Fe-W are considered, 10 wt.% Co added Co-W alloys should be sintered higher than 1680 °C to obtain enhanced transportation path between tungsten grains [57]. In addition, 10 wt.% Fe contained Fe-W alloys should be sintered at least 1750 °C to form liquid phase [58].

As for Ni-W alloys, the mixed Ni-W compacts could demonstrate higher densification tendency than Co and Fe added alloys. It can be explained with binary phase diagram of Ni-W which can be seen Appendix C. Owing to its high W solubility, it could provide more effective activated sintering behavior during sintering processes which performed at 1450 °C, whereas the alloys, which sintered at 1500 and 1550 °C, formed liquid phase. Therefore, elemental Ni powder could enhance the densification rate of compacts with accelerated transportation condition. As can be seen the mentioned binary phase diagram, 1495 °C is sufficient to form liquid phase in theory [57], but the process is generally performed at 10-30 °C above the melting temperature.

3.2.2 Ni-free Co-Fe Added Heavy Alloys Studies

Various Co/Fe ratio added heavy alloys were prepared to investigate the effect of solubility and altered powder metallurgy parameters such as compression pressure, sintering temperature and dwell time on densification behavior and hardness variation. Measured relative density and hardness values of prepared heavy alloys are given in Table 3.3 and Figure 3.47, respectively.

Table 3.3 The effect of the Co/Fe ratio variation on % relative densities.

Alloy code	Temperature (°C) / Time (min)							
	1500/60			1550/60			1550/90	1550/120
	300 MPa	350 MPa	400 MPa	300 MPa	350 MPa	400 MPa	350 MPa	350 MPa
	% Relative density							
0W1/4CF	78.8	80.1	82.3	83.7	86.1	86.6	86.4	87.1
0W1/1CF	79.7	81.6	83.7	81.6	82.3	82.9	86.6	87.5
0W4/1CF	77.8	78.5	80.9	82.5	83.3	84.1	84.6	85.8
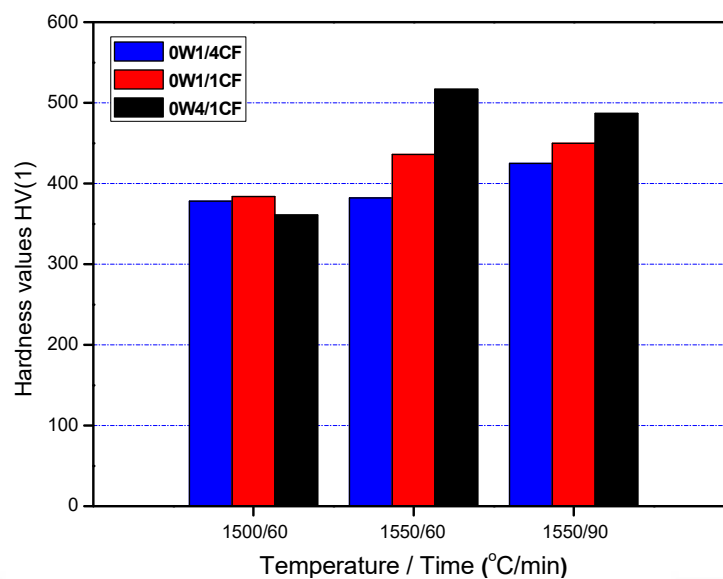
Figure 3.47 Sintering temperature and dwell time effect on HV (1) results.

As can be seen in Table 3.3 and Figure 3.47, the relative density and hardness values of fired alloys are demonstrated low correlation with altered sintering temperature and time.

The densification values of studied Co-Fe alloys are relatively more vulnerable to the sintering temperature and applied pressure changes, but dwell time, especially in Co-rich and Fe-rich heavy alloy combinations. Hardness values of studied alloys are demonstrated relatively more closer results at 1500 °C, but the increased sintering temperature caused to sharp hardness variation depend on Co-Fe ratio. Co-rich alloys have high hardness according to Fe-rich alloys after 1550 °C sintering process. In order to understand the reason of this variation, XRD analyses of selected alloys were conducted. The XRD analysis results are illustrated in Figure 3.48 and Figure 3.49, consecutively.

Rhombohedral Co_7W_6 $(Fe,Co)_7W_6$ phase formation was observed in XRD results of Co-Fe added heavy alloys which sintered at 1500 °C as well as 1550 °C [49]. As the temperature increased, weight ratio of formed total Co_7W_6 and Fe_7W_6 phase also increased.
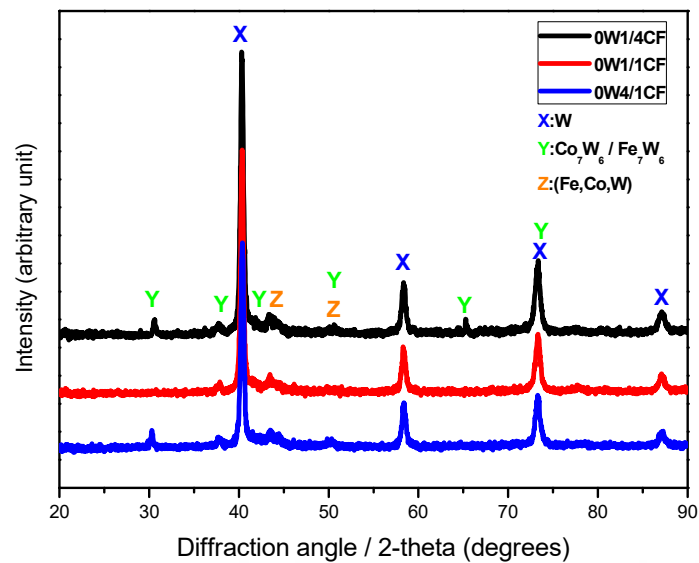
Figure 3.48 X-ray diffraction patterns of the Co-Fe added alloys (at 1500 °C).
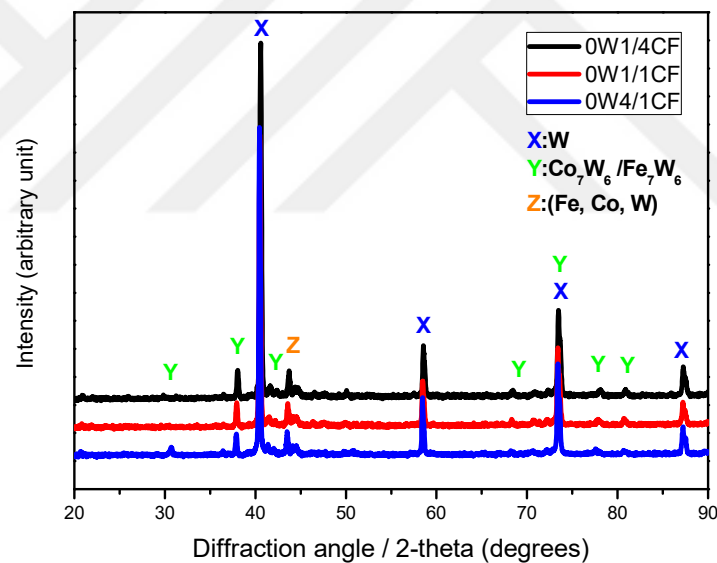
Figure 3.49 X-ray diffraction patterns of the Co-Fe added alloys (at 1550 °C).

Furthermore, irregular and coarse Widmansttaten platelets of binder microstructure caused to high hardness increment in spite of insufficiently densified structure of studied alloys [57].

On the other hand, as mentioned earlier in single additive added WHAs studies, Co and Fe employment in WHA applications demonstrated some disadvantages such as solid state sintering behavior [47], high wt.% W contained intermetallic phase

formation [49], sharp W solubility changes with decreased temperature [57]. In addition, their corrosion resistance is fairly lower than Ni-employed WHAs. It is attributed to formation of elemental Fe and (Fe-Co-W) solid solution which also decreases the oxidation resistance of studied heavy alloys.

3.2.3 Effects of Sintering Variables

Altered compression pressure, sintering atmosphere and additive particle size were studied in various combination of WHAs. 300, 350 and 400 MPa pressure were applied to investigate the variation of compact density with altered compression pressure. Therefore, a correlation between initial green density and sintered density was also presented in selected heavy alloys. In addition, insoluble and reductant gas mixture was also used in sintering treatment to demonstrate the influences of sintering atmosphere on sintering behavior. In this context, 50 % Ar added Ar-H_2 gas mixture was employed which had 0.4 l/min flow rate. Furthermore, coarse nickel (Ni*) powder was also employed to investigate the effect of additive particle size on densification tendency. It has 20-45 μm particle size range, 99% purity and its supplier code is GTV mbH 80.56.1. The initial particle size of Ni* powder is ten times bigger than W powder. Size difference between employed coarse Ni* powder and W powder is demonstrated in Figure 3.50. The sintering treatments of prepared pellets were performed at three different sintering temperatures from 1450 to 1550 °C for 1 h.
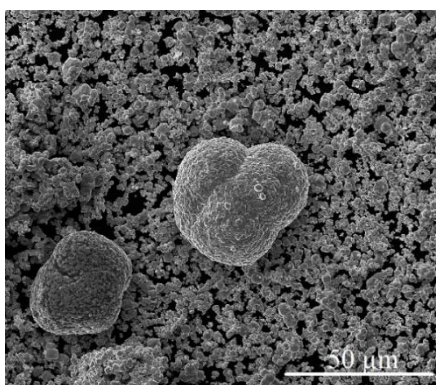
Figure 3.50 SEM images of the relatively fine W powder and coarse Ni* powder.

The effect of altered nickel particle size and applied compression pressure on green and/or sintered densities are given in Table 3.4.

Table 3.4 Effect of the altered nickel particle size and compression pressure on green density and/or sintered density.

Alloy code	Applied compression pressure (MPa)									400/5min	500	Practiced sintering temperature (°C)								
	300			350			400					1450			1500			1550		
	1	2	3	1	2	3	1	2	3			300	350	400	300	350	400	300	350	400
	Green densities (%)											Relative densities (%)								
0W4/1NC	60.7	61.1	61.3	62.5	64.2	63.1	62.7	64.2	63.7	-	-	96.6	97.5	97.2	98.4	98.9	98.8	99.4	99.7	99.6
0W4/1N*C	60.8	61.4	61.5	61.7	62.5	62.3	63.4	64.6	62.9	-	-	90.5	90.9	90.1	94.4	94.5	93.9	95.7	96.8	96.3
0W8/1NC	59.9	60.2	60.7	63.1	62.5	62.5	62.9	63.7	63.3	-	-	96.1	97.3	97.4	98.8	99.2	99.0	99.6	99.9	99.3
0W8/1N*C	60.3	60.7	59.9	60.9	62.5	61.4	64.1	62.7	63.6	-	-	93.1	92.5	92.2	94.8	95.3	94.8	96.4	97.3	95.7
0W8/1NF	60.3	61.4	60.8	60.3	58.6	59.7	63.2	64.2	63.5	-	-	96.6	97.9	97.1	98.1	98.7	98.3	99.4	99.4	99.5
0W8/1N*F	60.8	60.2	61.8	61.4	60.3	62.2	62.8	63.0	63.4	-	-	91.7	92.1	92.2	95.1	95.5	95.6	97.3	96.6	97.1
0W*4/1NC	-	-	-	-	42.8	-	-	43.6		47.9	51.2	-	-	-	65.3[a]	63.2	71.1[b]	-	66.0	-

N*: coarse nickel powder, a: W* powder compressed under 400 MPa for 5 min and sintered at 1500 °C, b: W* powder compressed under 500 MPa for 2 min sintered at 1500 °C. 1-1450 °C, 2-1500 °C and 3-1550 °C.

As can be seen in Table 3.4, except from W* powder employed heavy alloys, altered additive particle size was demonstrated great influence on densification tendency. It might be resulted from poor compositional homogeneity and taken place insufficient rearrangement phenomenon during earlier stage of liquid phase sintering. It is attributed to SSS and LPS regions took place at the same time, which is demonstrated in Figure 3.51.
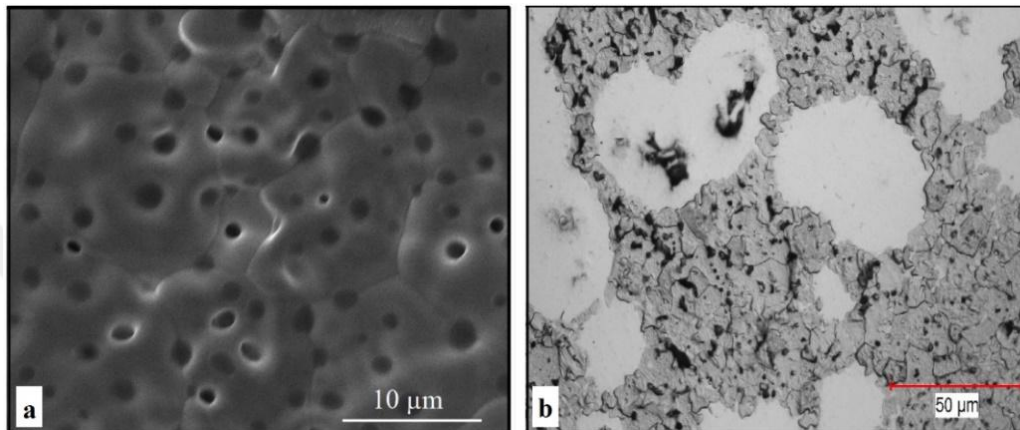
Figure 3.51 SSS and LPS regions in 0W4/1N*C alloy microstructure, sintered at 1450 °C for 1 h. (a: SSS taken by SEM, b: SSS and LPS taken by OM).

In addition, as can be seen from the densification results, coarse nickel powder added heavy alloys have lower density values than fine nickel powder added alloys. On the other hand, there were not direct correlation observed between green density and sintered density of studied alloys. It might be resulted from approximate initial green densities. In addition, some of interior and exterior parameters such as mixing homogeneity, uniform density variation of green compact, accuracy of weight measurements.

Microstructures of relatively fine and coarse nickel powder added 0W8/1NC and 0W8/1N*C alloys are indicated in Figure 3.52. As can be seen in Figure 3.52, Ni-rich binder phase distribution demonstrate wide variation in both alloys. The distribution caused limited and regional mass transportation via formed liquid phase. Therefore, insufficient densification behavior in coarse additive employed alloys are inevitable.
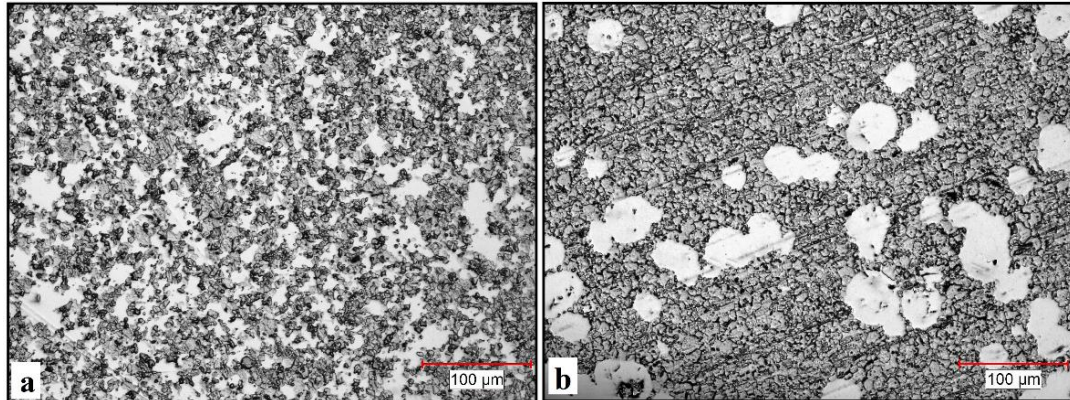
Figure 3.52 OM images of the 0W8/1NC and 0W8/1N*C, sintered at 1450 °C
for 1 h, (a:0W8/1NC, b:0W8/1N*C).

As for altered sintering atmosphere condition, 0W4/1NC, 0W8/1NC and 5W4/1NC heavy alloys were sintered under two different sintering atmosphere conditions. The results are demonstrated in Figure 3.53.
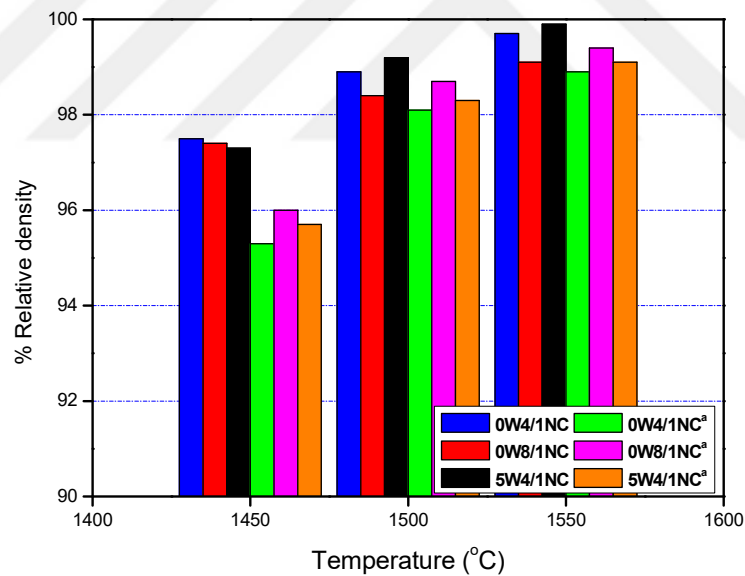
Figure 3.53 Effect of the insoluble gas employment on densification behavior
(a:Ar and H_2 mixed sintering atmosphere condition), sintered for 1 h.

As can be seen in Figure 3.53, Ar-contained sintering atmosphere demonstrates relatively slight influences on densification. However, as the sintering temperature decreased, the density differences between both sintering atmospheres increase. It can be explained via applied sintering temperature which was insufficient to obtain liquid

phase during sintering at 1450 °C. As mentioned earlier, activated sintering conditions took place at this sintering temperature, whereas enhanced mass transport paths were obtained at 1500 and 1550 °C applications. The formed liquid phase accelerated the pore elimination via relatively better pore motion from interior to surface and high pore filling tendency. The both parameters are mainly resulted from capillary force of melted additives. However the filled pores could not be annihilated during late sintering stages because of little but effective entrapped gas formation [40]. In addition, as can be seen in the figure, low sintering temperature caused to approximately 1% decreasing in relative density, while the sintering temperature increased the decreasing indicated variation about 0.5 %.

3.3 Further Studies with W* Powders

The conducted studies are aimed to enhance the sintering behavior of W* powder via designed pre-sintering treatments. In addition, when the sintered microstructures are considered, % relative density accuracy of W*HAs should be calculated again to obtain more suitable density data.

3.3.1 Phase and Impurity Analyses and Enhancement Studies

Since W** powder employed 0W**4/1NC alloys could not reach expected densification values, the underlying reasons of low densification tendency were investigated via a series of examination procedure such as XRD, XRF, EDS analyses and macro and micro structural investigation. The specimen was sectioned via low speed diamond saw (MTI SYJ-150). Macrostructure investigations were performed by using a digital microscope (Nikon Shuttle PixE). Image of the sectioned 0W**4/1NC specimen is illustrated in Figure 3.54. As can be seen in Figure 3.54, lots of pores and/or gaps were observed at the sectioned surface. The bigger pores might be resulted from the factors including relatively hard agglomerated powders, low coordination number of particles and elemental Ca evaporation from the pellet. The hard agglomerated powder characteristic was observed not only produced form but also mixed form with suitable additive(s). The hard agglomerated powder showed low densification tendency under compression pressure due to difficult to break the formed physical bonds.

Figure 3.54 Image of the sectioned W**HAs prepared from W** powder,
sintered at 1500 °C for 1 h.

In addition, insufficiently compressed pellets had considerably low coordination number (CN). The number is crucial parameter for densification, as the CN decreases, the green compact demonstrates coarsening tendency [45]. It can be explained with the mass transport mechanism. The mass moves from pore surface to grain interior, whereas the vacancy moves from interior to surface. On the contrary, the mass should migrate from interior to surface to obtain densified pellet [26]. The applied compression pressure was increased up to 500 MPa for 2 min to eliminate the both issues.

On the other hand, a pre-sintering treatment was designed to evaporate the elemental Ca, which contained in W** powder. The temperature and atmosphere pressure variations were investigated by using Equilib-Web (FactWeb) which is a web based thermochemical software and compound databases program. The conducted treatment parameters are illustrated in Figure 3.55.

Although the W** powder had dark color, its color transform to light grey color just like W powder. The altered powder color is demonstrated in Figure 3.56. Furthermore, compositional variation of each powder was examined with XRF, for elemental analysis, and XRD, for phase analysis. The XRD results of W** powder, W* powder and W powder are indicated in Figure 3.57.
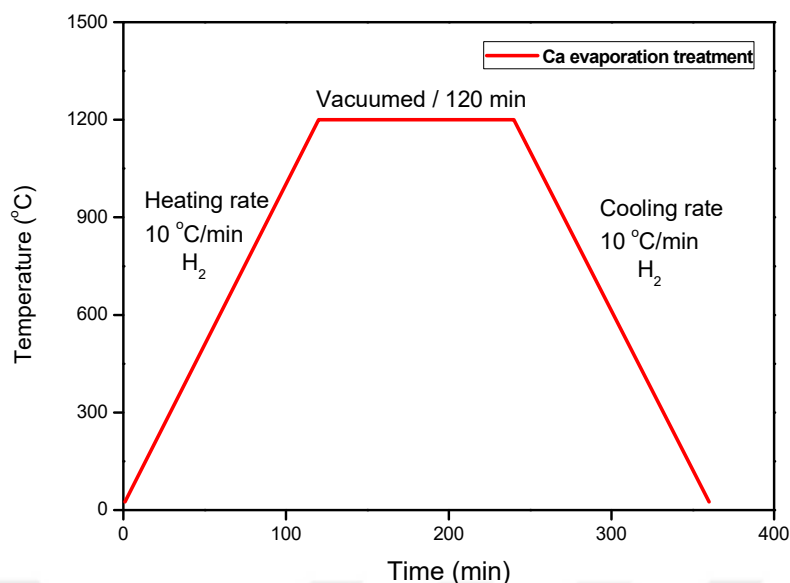
Figure 3.55 Temperature-time profile of calcium evaporation process (CEP).

Figure 3.56 Colors of the employed tungsten powders (a:W** powder, b:W* powder, c:W powder).

As can be seen in Figure 3.57, the untreated tungsten powder indicates a slight diffraction peak which shows similarity with scheelite and/or calcium bearing compounds theta angle, but the peak decreased in treated tungsten powder measurement. It is attributed to present of elemental Ca. In addition, scheelite is also present at produced tungsten. The presence of elemental Ca was also demonstrated via altered wt.% Ca in results which obtained from point EDS and XRF.

When it comes to impurity type and ratio, as mentioned earlier, produced tungsten powders had some impurities, but they were ignored during density measurements because of hard to obtain net composition and impurity content.
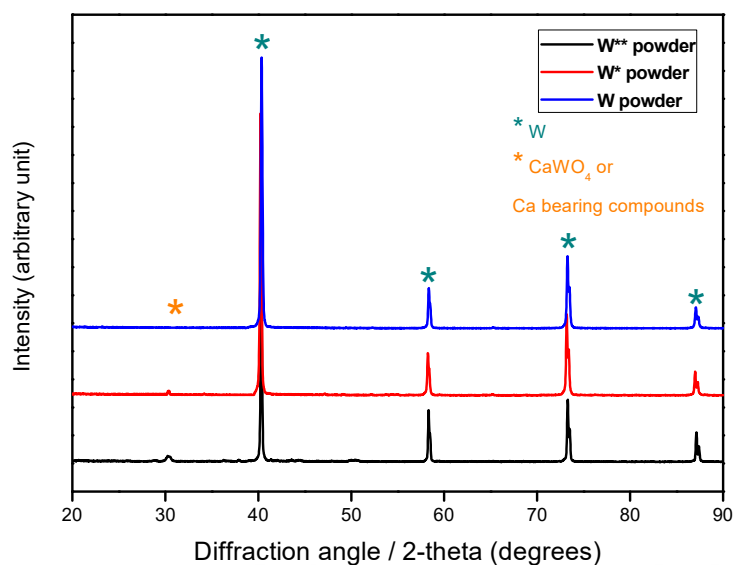
Figure 3.57 XRD analysis results of the employed tungsten powders.

Elemental Ca impurities most probably resulted from poor cleaning procedure with dilute HCl solution, whereas Ca compounds, scheelite, are derived from the incompletely took place molten salt electrolysis process.Moreover, Fe, Cr, trace amount Ni and Mo were detected during XRF and EDS analysis which resulted from dissolved stainless steel spoon. At least ten XRF measurements were taken from each produced tungsten powders.

The improved density results of studied W*HAs should have been determined to better understand the sintering behavior of W* powder. Chemical composition examination of W** and W* powders were conducted via EDAX TEAM EDS analysis system and Fisherscope X-ray XDV-SDD OptiPlex 3020 XRF device. Compositional variation of both produced tungsten powders are given in Table 3.5.

Table 3.5 XRF analysis results of the W* and W** powders.

Tungsten type	Initial W composition (wt.%)						Theoretical Density (g/cm³)
	W	Ca	Fe	Cr	Ni/Mo	Others	
W**	Balance	1.0-10.7	< 1.2	< 0.5	< 0.2/< 0.5	-	8.51-16.81
W*	Balance	< 0.6	< 0.6	< 0.3	< 0.1/< 0.3	-	17.76-19.3

% Relative density results of W*HAs are considerably lower than WHAs. However, when the microstructures of W*HAs are considered, they have almost completely densified structural appearances. Furthermore, the hardness values of W* powder employed W*HAs have roughly the same hardness results like WHAs. The improved % relative densities are given in Table 3.6.

Table 3.6 Improved relative densities of the W*HAs.

Alloy code	Relative density (%)		Alloy code	Relative density (%)	
	1500 °C / 1 h	1550 °C /1 h		1500 °C / 1 h	1550 °C /1 h
0W*7/3NC	86.4	90.5	0W*7/3NC	95.3	98.8
0W*7/3NF	85.2	-	0W*7/3NF	93.9	-
0W*4/1NC	78.2/80.8	85.6/87.5	0W*4/1NC	86.2/89.1	94.4/96.5
0W**4/1NC	63.2	66.0	0W**4/1NC	79.7	81.6
0W*8/1NC	90.3	-	0W*8/1NC	98.2	-
5W*4/1NC	-	92.2	5W*4/1NC	-	99.2

All in all, it is thought that insufficiently densified green compacts are seemed main reason for low densification tendency. The insufficiently densified structures are seemed as the most important reason to insufficient densification. In addition, the low densified green compact has low CN. The CN value plays an important role in determining of pore shrinkage and swelling tendency [59].

CHAPTER 4

CONCLUSIONS AND FUTURE WORKS

4.1 Conclusions

Sintering behavior of synthesized W* powder, obtained from electrodeoxidation of $CaWO_4$, was studied and compared with a W powder in terms of density, microstructural and mechanical properties for several selected alloys. From the evaluated properties including densification behavior, grain size measurements, hardness values, etc. major conclusions drawn are as follows:

Measured relative densities of the W*HAs could not reach to expected values compared to WHAs. Even though they indicated wide relative density variation between 60 % and 95 %, the properties such as microstructure, hardness and dissolved W in binder phase, had similar characteristics with fully densified WHAs. When the impurity level of W* powder was considered in the theoretical density calculations, most of the W*HAs could easily reach to higher than 98 % relative density.

Due to formation of high amount of liquid phase during sintering of W*HAs, shape distortion took place. The phenomenon was resulted from demolished solid skeleton, in other words, tungsten contiguity between W* grains. Moreover, it was observed in sintering studies of 90 wt.% W contained WHAs at 1550 °C for 1 h. However, the remarkable shape distortion could not be observed in Co-rich and Ni-free heavy alloys even at 1550 °C for 2 h sintering treatment. It can be said that densification value of specimens, volume of liquid phase, additive type and ratio, W content and applied sintering process are closely related with the shape distortion phenomenon.

The solubility capacity changes with decreased temperature is important parameter to obtain fully densified WHAs. Ni added alloys could easily reach close to theoretical density values at 1500 °C for 1 h, whereas Co-Fe added alloys could not be fully densified despite being sintered at 1550 °C for 2 h. On the other hand, oxidation and corrosion resistance of these alloys were lower than Ni added alloys due to formation

of free Fe and Co in addition to Fe_7W_6 and Co_7W_6 intermetallic phases. The free Fe most probably caused to decrease in oxidation resistance of W based heavy alloys.

Dissolved W content in binder phase and matrix hardness variation generally demonstrated direct correlation. As the dissolved W ratio in binder increased, hardness value of the binder phase also increased.

Two binder phase included heavy alloys not only had high dissolved W variation between each binder phase but also indicated sharp hardness variation. Relatively darker region had approximately 500 HV(0.005) average hardness value, whereas lighter region, Co-rich and about 75 wt.% W contained, had higher hardness values changing between 1350 and 2400 HV(0.005).

W* powder exhibited better densification behavior than W powder. It was attributed to insufficiently purified W* powder which had impurities derived from the production process. The impurities lead to formation of activated and/or liquid phase sintering condition during sintering treatment.

EDS and XRD analyses demonstrated that Co and Fe had high W dissolving ability, approximately 75 wt. % W by forming Co_7W_6 and Fe_7W_6. However, densification behavior of Co-Fe added alloys were relatively lower than Ni added alloys due to lack of liquid transportation path between the W particles/grains.

The mixed and pure H_2 atmosphere employed sintering studies indicated that Ar included atmosphere had a slightly negative effect on densification performance of studied alloys due to entrapped gas formation in pores. This gas could not be dissolved and thrown out by melted binder phase.

Average grain size (AGS) measurement results showed that increased temperature and time lead to tendency of higher grain size formation, whereas the increased liquid phase ratio had a negative influence on formation bigger grains as well as densification behavior. Therefore, high liquid contained W*HAs had lower AGS compared to WHAs which were sintered at the same sintering conditions. It might have been also resulted from the smaller particle size of W* powder.

Dissolved W amount in binder phase was affected from most of sintering variables. But a regular correlation between dissolved W in binder phase and the studied variables; like sintering temperature, employed additives and their ratios, was not observed.

Although Co-Fe added alloys had relatively low densification values, they had considerably high hardness values when compared to Ni-added heavy alloys. The hardness values were similar to Ni-added heavy alloy after 1500 °C for 1 h sintering treatment, but the hardness results sharply increased up to 520 HV (1).

4.2 Future Works

The electrochemical extraction process should be reconsidered to eliminate the contamination of W* powder. The electrochemical reduction process should be prolonged to ensure complete reduction and some post-purification methods can be applied to obtain a purer product.

The amounts of impurities of W* powder can be extensively characterized and taken into account in the preparation of heavy alloy compositions. By this way, excess liquid phase formation during W* powder sintering can be eliminated.

Performed research for Co-Fe alloys demonstrated that these alloys would be good candidates for not only high density but also high wear resistance. Increasing the sintering temperature and dwell time may be performed to obtain fully densified Co-Fe added alloys to better understand their properties.

REFERENCES

[1]   Chen, G., Fray, D. & Farthing, T., "WO 99/646381999-World Patent", 1999.

[2]   Bhagat R., Jackson, M., Inman, D. & Dashwood, R., "The Production of Ti–Mo Alloys from Mixed Oxide Precursors via the FFC Cambridge Process", Journal of the Electrochemical Society, 155, 6, 63-69, 2008.

[3]   Bhagat, R., Jackson, M., Inman, D. & Dashwood, R., "The Production of Ti–W Alloys from Mixed Oxide Precursors via the FFC Cambridge Process", Journal of the Electrochemical Society, 156, 1, 1–7, 2009.

[4]   Erdoğan, M., & Karakaya, İ., "Production of Tungsten and Tungsten Alloys from Tungsten Bearing Compounds by Electrochemical Methods", Turkish Patent Institute, TR-2007 07197 B, 2007.

[5]   Erdoğan, M. & Karakaya, İ., "Production of Tungsten and Tungsten Alloys from Tungsten Bearing Compounds by Electrochemical Methods", Russian Patent Institute, 2463387, 2012.

[6]   Erdoğan, M. & Karakaya, İ., "Production of Tungsten and Tungsten Alloys from Tungsten Bearing Compounds by Electrochemical Methods", Canadian Patent Institute, 2-703–400, 2012.

[7]   "Tungsten Applications | International Tungsten Industry Association (ITIA)." [Online]. Available: http://www.itia.info/applications.html. [Accessed: 26-May-2017].

[8]   Lassner E. & Schubert, W-D., "Tungsten (Properties, Chemistry, Technology of the Element, Alloys, and Chemical Compounds)", Plenum Publishers, New York, 1998.

[9]   Kimball, S. M., "Mineral Commodities Summaries", U.S. Geological Survey, 180-181, 2016.

[10]   T.C. Başbakanlık DPT, "Eight Five Year Development Plan 2001-2005", 2001.

[11]   "Price Book." [Online]. Available: https://www.metalbulletin.com/.[Accessed: 28-May-2017].

[12]   Pitfield, P. & Brown, T., "Tungsten Commodity Profile", British Geological Survey, 33, 2011.

[13]   Mullendore, J. A., "Tungsten: Its Manufacture, Properties, and Application", ASTM, Florida, 82–105, 1984.

[14]   Asare, K. O., "Solution Chemistry of Tungsten Leaching Systems", Journal of Electronic Materials, 21, 1, 555–564, 1982.

[15]   Rosenqvist, T.,"Thermochemical Data for Metallurgists", Tapir, Norway, 1970.

[16]   "DoITPoMS - TLP Library Ellingham Diagrams-The interactive Ellingham diagram", [Online].Available: https://www.doitpoms.ac.uk/tlplib/ellingham_diagrams/interactive. php. [Accessed: 28-May-2017].

[17]   Erdoğan, M., "Recovery of Tungsten from Tungsten Bearing Compounds", Ph.D. Thesis, Middle East Technical University, Graduate School of Natural and Applied Sciences, Ankara-Turkey, 2013.

[18]   Chen, G., Fray, D. & Farthing, T., "Direct Electrochemical Reduction of Titanium Dioxide to Titanium in Molten Calcium Chloride", Nature, 407, 6802, 361–364, 2000.

[19]   Gordo, E., Chen, G. Z. & Fray, D. J., "Toward Optimisation of Electrolytic Reduction of Solid Chromium Oxide to Chromium Powder in Molten Chloride Salts", Electrochimica Acta, 49, 13, 2195–2208, 2004.

[20]   "CaCl$_2$-NaCl Phase Diagram-FACTWEB", [Online]. Available:http://www.crct.polymtl.ca/ factweb.php. [Accessed: 28-May-2017].

[21]   Özdemir, F., Erdoğan, M., Elmadağlı, M. & Karakaya, İ., "Production of Tungsten by Pulse Current Reduction of CaWO$_4$", in Rare Metal Technology, Springer International Publishing, 151–158, 2016.

[22]   Erdoğan, M. & Karakaya, İ., "On the Electrochemical Reduction Mechanism of CaWO$_4$ to W Powder", Metallurgical and Materials Transactions B, 43, 4, 667-670, 2012.

[23]   German, R. M., "Powder Metallurgy Science", Metal Powder Industries Federation, New Jersey, 1984.

[24]   German, R. M., "Sintering from Empirical Observations to Scientific Principles", Elsevier Butterworth-Heinemann, Massachusetts, 2014.

[25]   Upadhyaya, G. S., "Powder Metallurgy Technology", Cambridge International Science Publishing, Cambridge, 2002.

[26]   Kang, S. L., "Sintering Densification, Grain Growth and Microstructure", Elsevier Butterworth-Heinemann, Oxford, 2005.

[27]   Fang, Z. Z., "Sintering of Advanced Materials", Woodhead Publishing, Cambridge, 2010.

[28]   Zovas, P. E., German, R. M., Hwang, K. S. & Li, C. J., "Activated and Liquid Phase Sintering-Progress and Problems", Journal of the Minerals, Metals & Materials Society, 35, 1, 28–33, 1983.

[29]   German, R. M., Suri, P. & Park, S. J., "Review: Liquid Phase Sintering", Journal of Materials Science, 44, 1, 1–39, 2009.

[30] Yi, W., German, R. M. & Lu, P. K., "Shape Distortion and Dimensional Precision in Tungsten Heavy Alloy Liquid Phase Sintering", 15th International Plansee Seminar, 1, 761–779, 2001.

[31] Savitskii, A., "Liquid-Phase Sintering of the Systems with Interacting Components", Advanced Science and Technology of Sintering, 19–28, 1999.

[32] Kiran, U. R., Panchal, A., Sankaranarayana, M., Nageswara Rao, G. V. S. & Nandy, T. K., "Effect of Alloying Addition and Microstructural Parameters on Mechanical Properties of 93% Tungsten Heavy Alloys", Materials Science and Engineering A, 640, 82–90, 2015.

[33] Park, H. D., Baik, W. H. Kang, S. L & Yoon, D. Y., "The Effect of Mo Addition on the Liquid-Phase Sintering of W Heavy Alloy", Metallurgical and Materials Transactions A (Physical Metallurgy and Materials Science), 27A, 10, 3120–3125, 1996.

[34] Hsu, C. S. & Lin, S. T., "Effect of Molybdenum on Grain Growth of W-Mo-Ni-Fe Heavy Alloys", Journal of Materials Science, 38, 7, 1543–1549, 2003.

[35] Kemp, P. B. & German, R. M., "Mechanical Properties of Molybdenum Alloyed Liquid Phase- Sintered Tungsten-Based Composites", Metallurgical and Materials Transactions A, 135, August, 2187–2189, 1995.

[36] Liu, W., Ma, Y. & Huang, B., "Influence of Minor Elements Additions on Microstructure and Properties of 93W-4.9Ni-2.1Fe Alloys", Bulletin Materials Science, 31, 1–6, 2008.

[37] Dinçer, O., "Liquid Phase Sintering of Tungsten-Nickel-Cobalt Heavy Alloys", M. Sc. Thesis, Middle East Technical University, Graduate School of Natural and Applied Sciences, Ankara-Turkey, 2014.

[38] Mondal, A., Upadhyaya, A. & Agrawal, D., "Effect of Heating Mode and Sintering Temperature on the Consolidation of 90W-7Ni-3Fe Alloys", Journal of Alloys and Compounds, 509, 2, 301–310, 2011.

[39] Li, Y., Hu, K., Li, X., Ai, X. & Qu, S., "Fine-Grained 93W-5.6Ni-1.4Fe Heavy Alloys with Enhanced Performance Prepared by Spark Plasma Sintering", Materials Science Engineering A, 573, 245–252, 2013.

[40] Bose, A. & German, R. M., "Sintering Atmosphere Effects on Tensile Properties of Heavy Alloys", Metallurgical Transactions A, 19, 10, 2467–2476, 1988.

[41] Kiran, U. R., Rao, A. S., Sankaranarayana, M. & Nandy, T. K., "Swaging and Heat Treatment Studies on Sintered 90W-6Ni-2Fe-2Co Tungsten Heavy Alloy", International Journal of Refractory Metals and Hard Materials, 33, 113–121, 2012.

[42] Xu, X., Upadhyaya, A., German, R. M. & Iacocca, R. G., "The Effect of Porosity on Distortion of Liquid Phase Sintered Tungsten Heavy Alloys", International Journal of Refractory Metals and Hard Materials, 17, 369–379, 1999.

[43] Liu, J. & German, R. M., "Densification and Shape Distortion in Liquid-Phase Sintering", Metallurgical & Materials Transactions A, 30, 3211–3217, 1999.

[44] German, R. M., Liu, Y. & Griffo, A., "Gravitational Effects on Grain Coarsening During Liquid Phase Sintering", Metal Powder Report, 52, 11, 38–39, 1997.

[45] German, R. M., "Coordination Number Changes During Powder Densification", Powder Technology, 253, 368–376, 2014.

[46] Bollina, R. & German, R. M., "Heating Rate Effects on Microstructural Properties of Liquid Phase Sintered Tungsten Heavy Alloys," International Journal of Refractory Metals and Hard Materials, 22, 2–3, 117–127, 2004.

[47] Gupta, K. P., "The Co-Ni-W (cobalt-nickel-tungsten) System," Journal of Phase Equilibria, 21, 4, 396–401, 2000.

[48] Ryu, H. J., Hong, S. H., Lee, S. & Baek, W. H., "Microstructural Control of and Mechanical Properties of Mechanically Alloyed Tungsten Heavy Alloys", Metals and Materials, 5, 2, 185–191, 1999.

[49] Bolokang, A. S., Phasha, M. J. & Motaung, D. E., "Ball Milling and Annealing of Co-50 at% W Powders", International Journal of Nonferrous Metallurgy, 2, 41–46, 2013.

[50] Shi, J. L., "Relation Between Coarsening and Densification in Solid-state Sintering of Ceramics: Experimental Test on Superfine Zirconia Powder Compacts", Journal of Materials Research, 14, 4, 1389–1397, 2011.

[51] Kiran, U. R., Venkat, S., Rishikesh, B., Iyer, V. K., Sankaranarayana, M. & Nandy, T. K., "Effect of Tungsten Content on Microstructure and Mechanical Properties of Swaged Tungsten Heavy Alloys", Materials Science Engineering A, 582, 389–396, 2013.

[52] German, R. M. & Munir, Z. A., "Enhanced Low-Temperature Sintering of Tungsten", Metallurgical Transactions A, 7, 12, 1873–1877, 1976.

[53] Bollina, R., Suri, P., Park, Sj. & German, R. M., "Micro Structural Evolution of a 93 wt% Tungsten Heavy Alloy : A Quenching Study to Understand the Evolution of Contiguity, Connectivity with Sintering Temperature and Time", Journal of Powder Metallurgy & Mining, 4, 1, 1–5, 2015.

[54] German, R. M., Bose, A., & Mani, S. S., "Sintering Time and Atmosphere Influences on the Microstructure and Mechanical Properties of Tungsten Heavy Alloys", Metallurgical Transactions A, 23, 1, 211–219, 1992.

[55] Li, C. & German, R. M., "The Properties of Tungsten Processed by Chemically Activated Sintering", Metallurgical Transactions A, 14, 10, 2031–2041, 1983.

[56] Srikanth, V. & Upadhyaya, G. S., "Sintered Properties of W-Cr-Ni Heavy Alloys", Journal of Less Common Metals, 120, 2, 213–224, 1985.

[57] Davis, J. R., ASM Specialty Handbook: Nickel, Cobalt, and Their Alloys, ASM International, 2000.

[58] Predel, B., "Fe-W (Iron-Tungsten)", Heidelberg, Springer Berlin, 1-4, 1995.

[59] German, R. M., "Coarsening in Sintering: Grain Shape Distribution, Grain Size Distribution, and Grain Growth Kinetics in Solid-Pore Systems", Critical Reviews in Solid State Materials Sciences, 35, 4, 263–305, 2010.

APPENDICES

Appendix A: Measured Density Results of Studied Alloys.

Appendix B: Optical Microscope Images of Studied Alloys.

Appendix C: Related Phase Diagrams.

Appendix D: Micro and Macro Scale Hardness Measurements.

Appendix E: Dissolved wt% W in Binder Matrix Phase.

Appendix F: Average Grain Size Measurements.

Appendix G: % Binder Phase Area Measurements.

Appendix A – Measured Density Results of Studied Alloys

Table A.1 Green density results of compressed compacts.

Alloy code	Calculated densities of green compacts (g/cm³)				
	Temperature / Time (°C/min)				
	1450/60	1500/60	1550/60	1550/90	1550/120
W	-	11.9	11.7	-	-
W*	-	10.8	11.1	-	-
W**	-	9.8	9.6	-	-
0W10N	10.6	10.7	10.6	10.7	-
0W10C	10.7	10.8	10.7	10.8	-
0W10F	10.4	10.5	10.4	10.6	-
0W1/4NC	10.6	10.7	10.5	10.7	10.6
0W1/1NC	10.5	10.7	10.4	-	-
0W7/3NC	10.6	10.8	10.7	-	-
0W7/1.5/1.5NCF	10.5	10.7	10.6	-	-
0W7/3NF	10.7	10.5	10.1	-	-
0W4/1NC	10.8	11.1	10.9	-	-
0W8/1NC	10.9	10.8	10.8	-	-
0W8/1NF	10.4	10.1	10.3	-	-
0W*7/3NC	-	9.2	9.5	-	-
0W*7/3NF	-	9.1	-	-	-
0W*4/1NC	-	9.2/9.2	9.5/9.4	-	-
0W**4/1NC	-	7.4	7.6	-	-
0W*8/1NC	-	9.9	-	-	-
0W1/4CF	-	10.7	10.9	10.7	10.5
0W1/1CF	-	10.8	11.0	10.7	10.6
0W4/1CF	-	11.1	10.7	10.9	11.0
5W1/4NC	11.3	11.6	11.4	11.2	11.6
5W1/1NC	11.2	11.4	11.6	-	-
5W7/3NC	11.4	11.6	11.5	-	-
5W4/1NC	11.2	11.7	11.6	-	-
5W8/1NC	11.0	11.3	11.5	-	-
5W*4/1NC	-	-	10.1	-	-

Table A.2 Relative density (%RD) results of compressed green compacts.

Alloy code	% Relative densities of green compacts (g/cm³)				
	Temperature / Time (°C/min)				
	1450/60	1500/60	1550/60	1550/90	1550/120
W	-	61.6	60.6	-	-
W*	-	56.0	57.5	-	-
W**	-	50.8	49.7	-	-
0W10N	61.3	61.9	61.3	61.9	-
0W10C	61.9	62.5	61.9	62.5	-
0W10F	61.7	62.3	61.7	62.9	-
0W1/4NC	61.3	61.9	60.7	61.9	61.3
0W1/1NC	60.7	61.9	60.1	-	-
0W7/3NC	61.3	62.5	61.9	-	-
0W7/1.5/1.5NCF	61.0	62.1	61.5	-	-
0W7/3NF	62.4	61.2	58.9	-	-
0W4/1NC	62.5	64.2	63.1	-	-
0W8/1NC	63.1	62.5	62.5	-	-
0W8/1NF	60.3	58.6	59.7	-	-
0W*7/3NC	-	53.2	55.0	-	-
0W*7/3NF	-	53.1	-	-	-
0W*4/1NC	-	53.2/53.2	55.0/54.4	-	-
0W**4/1NC	-	42.8	44.0	-	-
0W*8/1NC	-	57.3	-	-	-
0W1/4CF	-	63.2	64.4	63.2	62.0
0W1/1CF	-	63.3	64.5	62.7	62.1
0W4/1CF	-	64.6	62.2	63.4	64.0
5W1/4NC	61.9	63.6	62.5	61.4	63.6
5W1/1NC	61.4	62.5	63.6	-	-
5W7/3NC	62.5	63.6	63.0	-	-
5W4/1NC	61.4	64.1	63.6	-	-
5W8/1NC	60.3	61.9	63.0	-	-
5W*4/1NC	-	-	55.4	-	-

Table A.3 Densities of sintered specimens.

Alloy code	Sintered densities (g/cm³)				
	Temperature / Time (°C/min)				
	1450/60	**1500/60**	**1550/60**	**1550/90**	**1550/120**
W	-	12.82	13.64	-	-
W*	-	16.15	16.46	-	-
W**	-	14.73	14.91	-	-
0W10N	16.43	16.81	17.05	17.11	-
0W10C	11.77	12.26	14.21	14.51	-
0W10F	11.37	12.01	13.62	13.87	-
0W1/4NC	13.81	15.0	16.0	16.2	16.3
0W1/1NC	17.00	17.16	17.26	-	-
0W7/3NC	16.80	17.05	17.22	-	-
0W7/1.5/1.5NCF	16.77	17.01	17.18	-	-
0W7/3NF	16.64	16.92	17.10	-	-
0W4/1NC	16.85	17.09	17.23	-	-
0W8/1NC	16.81	17.14	17.26	-	-
0W8/1NF	16.88	17.02	17.14	-	-
0W*7/3NC	-	14.93	15.64	-	-
0W*7/3NF	-	14.61	-	-	-
0W*4/1NC	-	13.51/13.96	14.80/15.12	-	-
0W**4/1NC	-	10.92	11.41	-	-
0W*8/1NC	-	15.6	-	-	-
0W1/4CF	-	13.56	14.58	14.63	14.75
0W1/1CF	-	13.92	14.04	14.77	14.93
0W4/1CF	-	13.49	14.32	14.54	14.75
5W1/4NC	14.74	15.84	16.95	17.19	17.25
5W1/1NC	17.18	18.09	18.17	-	-
5W7/3NC	17.44	18.02	18.11	-	-
5W4/1NC	17.51	18.00	18.13	-	-
5W8/1NC	17.42	17.93	18.17	-	-
5W*4/1NC	-	-	16.82	-	-

Table A.4 Densification parameters (Ψ) results of investigated specimens.

Alloy code	Sintered densities (g/cm³)				
	Temperature / Time (°C/min)				
	1450/60	1500/60	1550/60	1550/90	1550/120
W	-	0.124	0.25	-	-
W*	-	0.63	0.65	-	-
W**	-	0.52	0.55	-	-
0W10N	0.87	0.93	0.96	0.97	-
0W10C	0.16	0.22	0.53	0.57	-
0W10F	0.15	0.24	0.50	0.52	-
0W1/4NC	0.48	0.65	0.81	0.84	0.85
0W1/1NC	0.96	0.98	0.997	-	-
0W7/3NC	0.93	0.96	0.991	-	-
0W7/1.5/1.5NCF	0.933	0.968	0.994	-	-
0W7/3NF	0.92	0.965	0.993	-	-
0W4/1NC	0.934	0.969	0.992	-	-
0W8/1NC	0.926	0.978	0.997	-	-
0W8/1NF	0.947	0.969	0.985	-	-
0W*7/3NC	-	0.709	0.789	-	-
0W*7/3NF	-	0.684	-	-	-
0W*4/1NC	-	0.533/0.589	0.68/0.726	-	-
0W**4/1NC	-	0.356	0.39	-	-
0W*8/1NC	-	0.772	-	-	-
0W1/4CF	-	0.459	0.61	0.631	0.661
0W1/1CF	-	0.498	0.502	0.64	0.67
0W4/1CF	-	0.392	0.558	0.579	0.606
5W1/4NC	0.496	0.638	0.811	0.85	0.851
5W1/1NC	0.849	0.978	0.989	-	-
5W7/3NC	0.883	0.967	0.981	-	-
5W4/1NC	0.896	0.963	0.983	-	-
5W8/1NC	.8867	0.955	0.989	-	-
5W*4/1NC	-	-	0.825	-	-

Appendix B – Optical Microscope Images of Studied Alloys
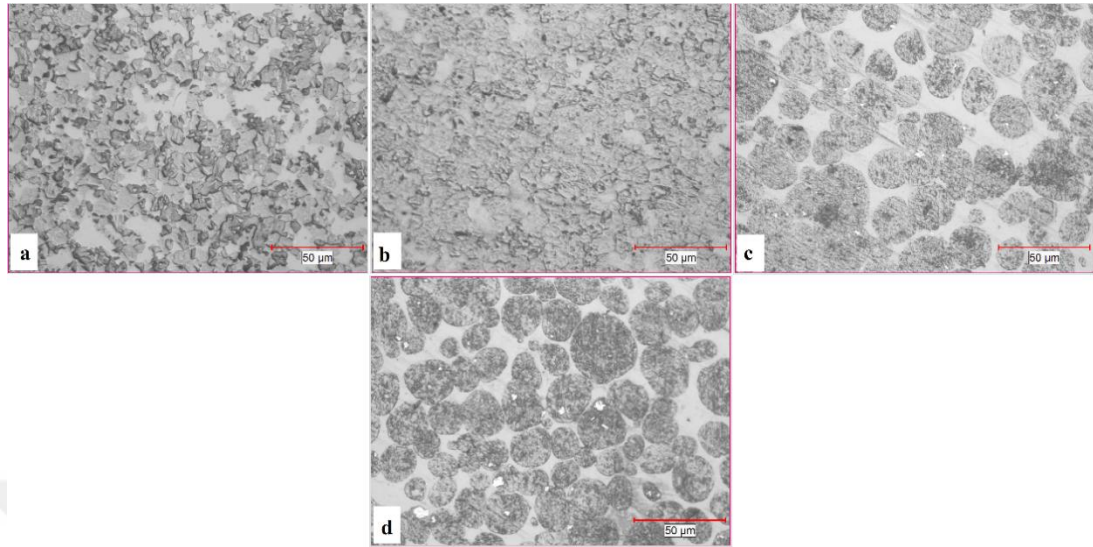
Figure B.1 Microstructure images of the 0W10N alloys obtained by (OM)
(a:1450 °C, b:1500 °C, c:1550 °C d:1550 °C/90 min, 500x).
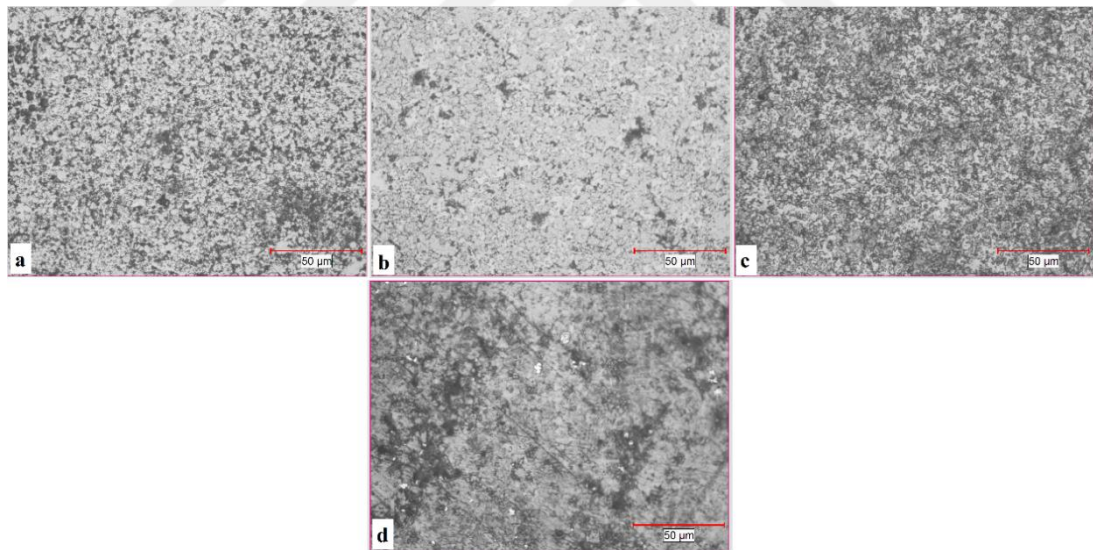
Figure B.2 Microstructure images of the 0W10C alloys obtained by (OM)
(a:1450 °C, b:1500 °C, c:1550 °C d:1550 °C/90 min, 500x).
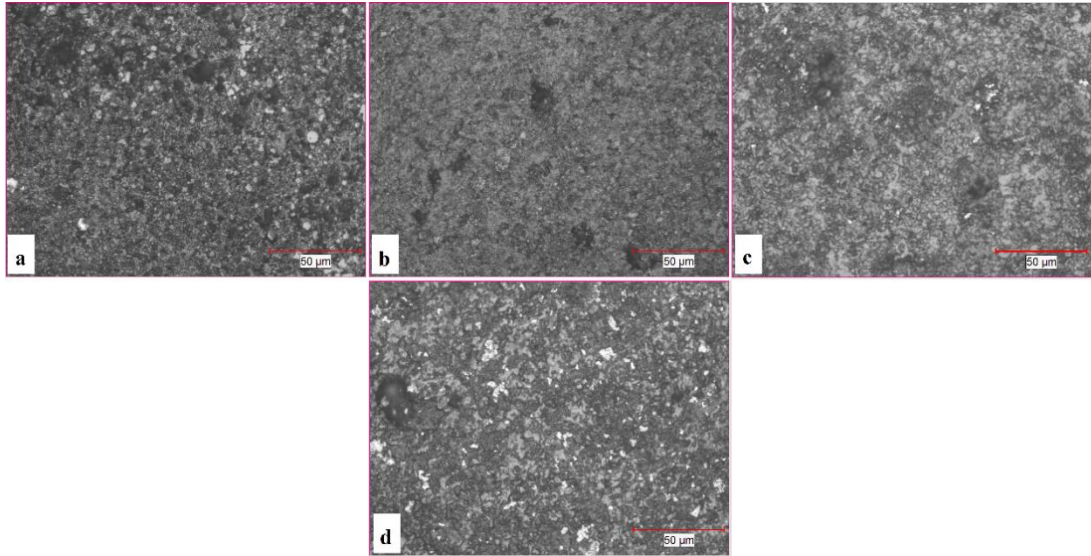
Figure B.3 Microstructure images of the 0W10F alloys obtained by (OM)
(a:1450 °C, b:1500 °C, c:1550 °C d:1550 °C/90 min, 500x).
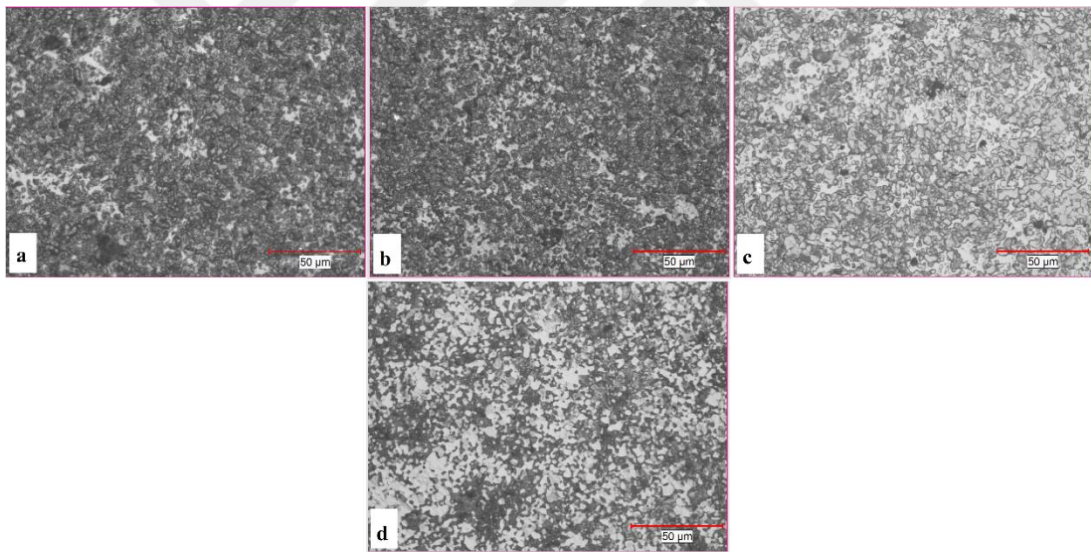
Figure B.4 Microstructure images of the 0W1/4CF alloys obtained by (OM)
(a:1500 °C, b:1550 °C, c:1550 °C/90 min d:1550 °C/120 min, 500x).
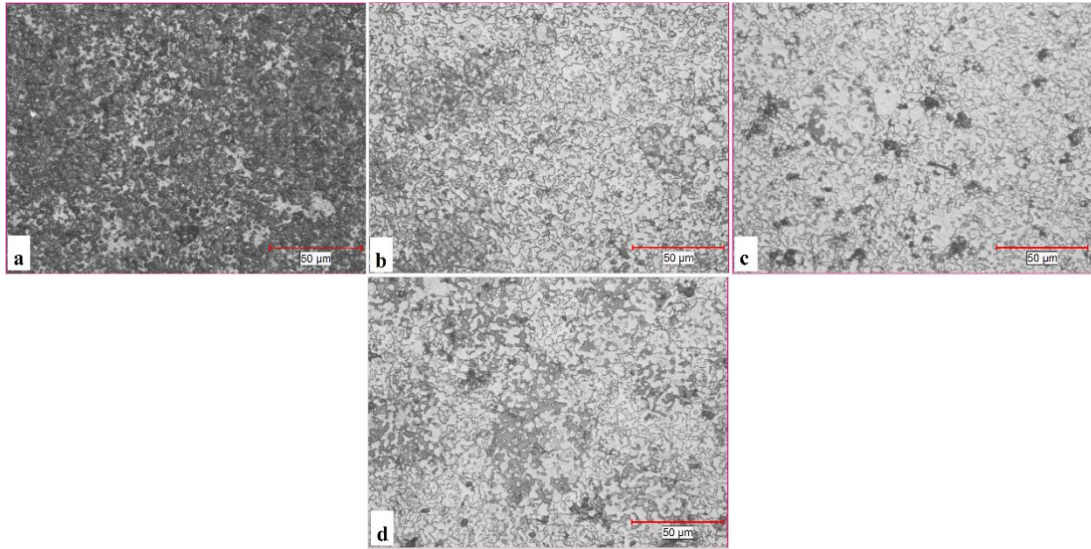
Figure B.5 Microstructure images of the 0W1/1CF alloys obtained by (OM)
(a:1500 °C, b:1550 °C, c:1550 °C/90 min d:1550 °C/120 min, 500x).
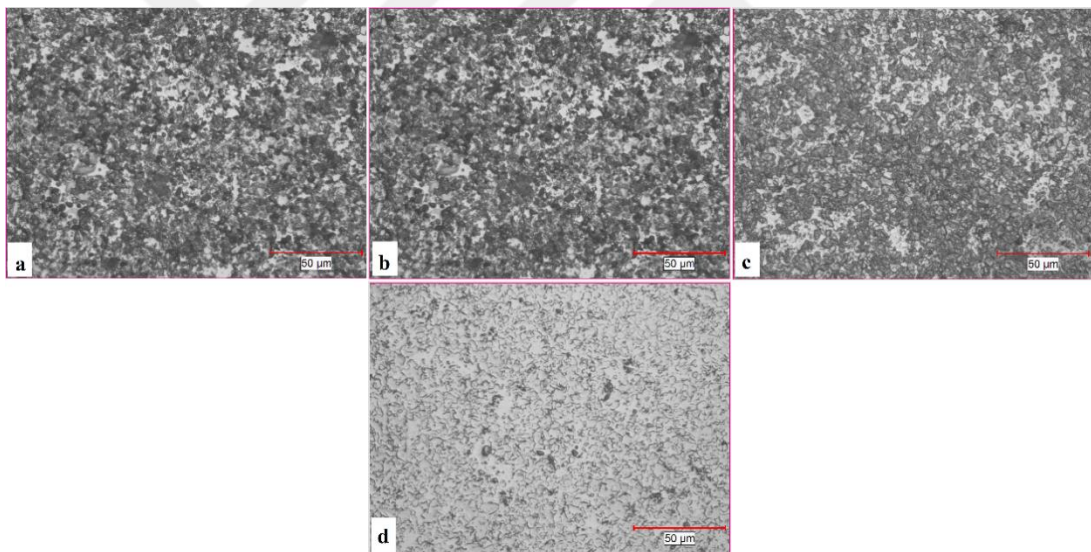
Figure B.6 Microstructure images of the 0W4/1CF alloys obtained by (OM)
(a:1500 °C, b:1550 °C, c:1550 °C/90 min d:1550 °C/120 min, 500x).
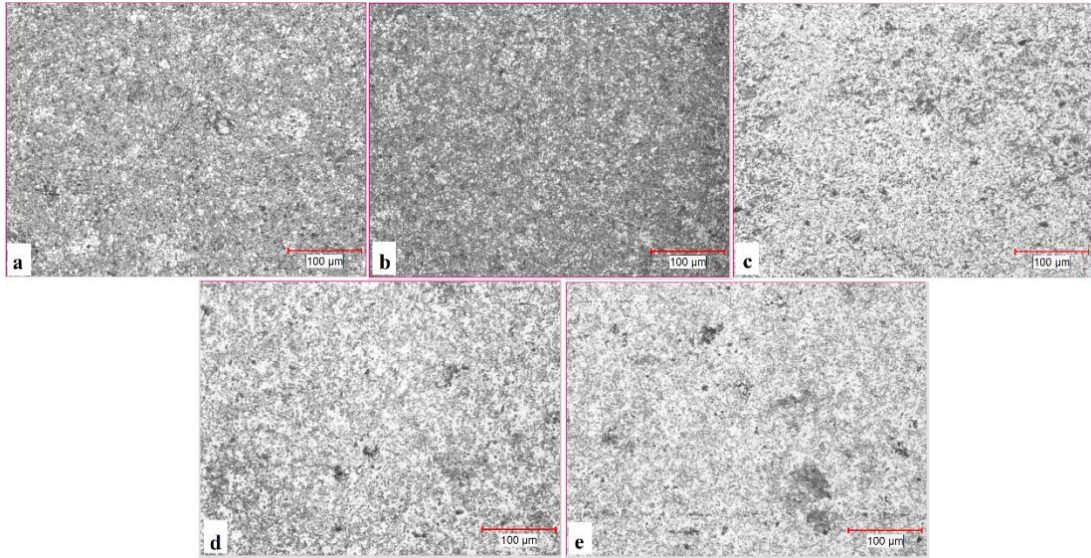
Figure B.7 Microstructure images of the 0W1/4NC alloys obtained by (OM)
(a:1450 °C, b:1500 °C, c:1550 °C, d:1550 °C/90 min, e:1550 °C/120 min, 200x).
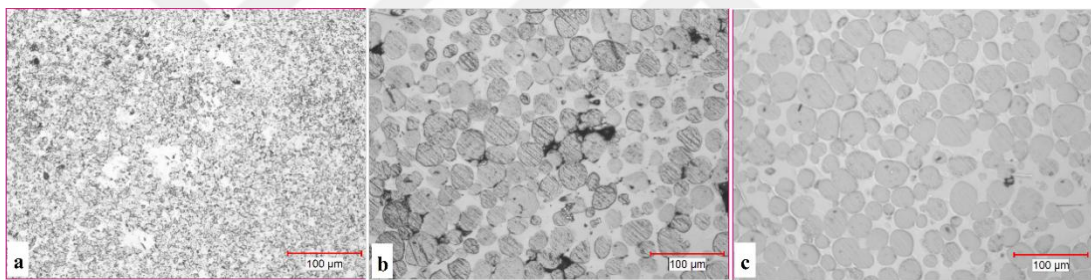
Figure B.8 Microstructure images of the 0W1/1NC alloys obtained by (OM)
(a:1450 °C, b:1500 °C, c:1550 °C, 200x).
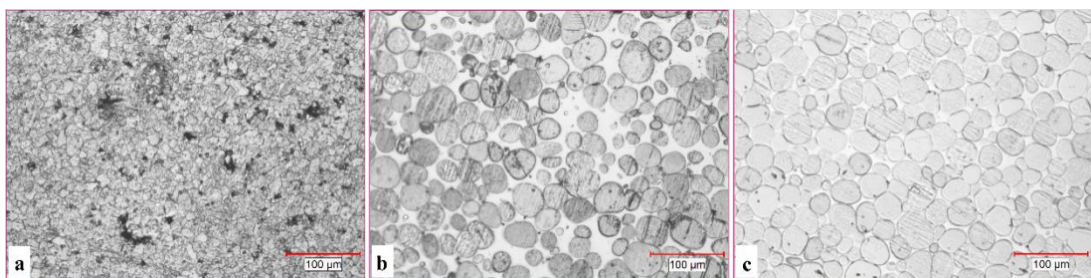
Figure B.9 Microstructure images of the 0W7/3NC alloys obtained by (OM)
(a:1450 °C, b:1500 °C, c:1550 °C, 200x).
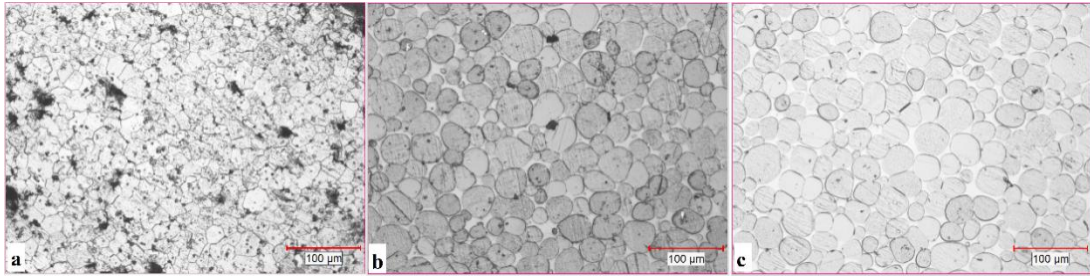
Figure B.10 Microstructure images of the 0W7/1.5/1.5NC alloys obtained by (OM) (a:1450 °C, b:1500 °C, c:1550 °C, 200x).
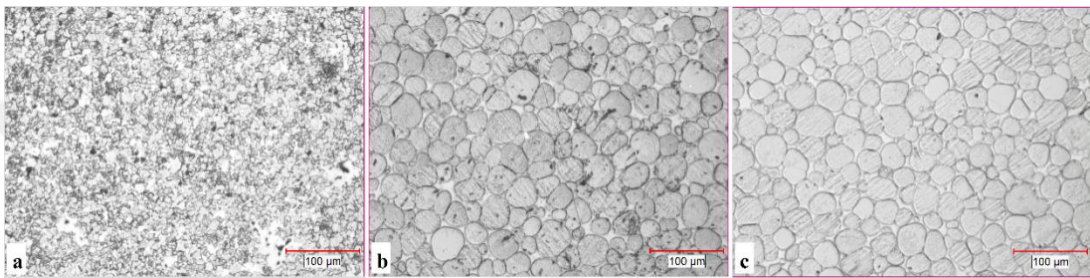
Figure B.11 Microstructure images of the 0W7/3NF alloys obtained by (OM) (a:1450 °C, b:1500 °C, c:1550 °C, 200x).
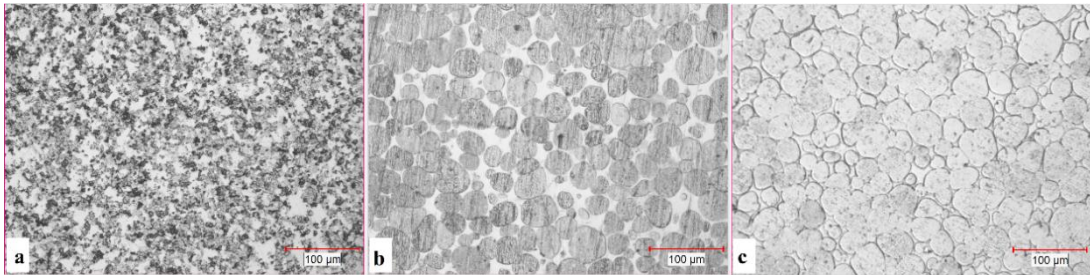
Figure B.12 Microstructure images of the 0W4/1NC alloys obtained by (OM) (a:1450 °C, b:1500 °C, c:1550 °C, 200x).
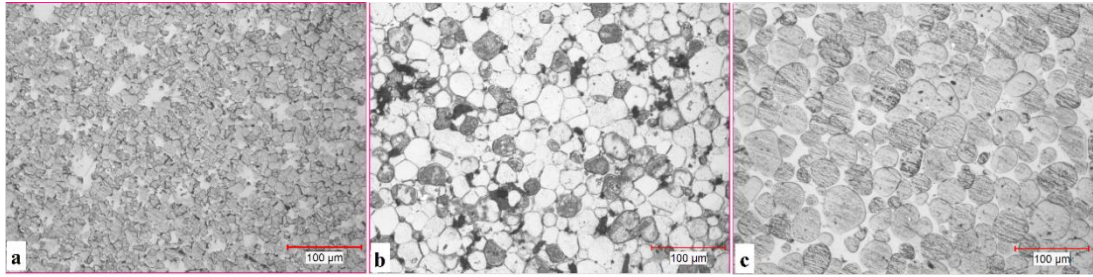
Figure B.13 Microstructure images of the 0W8/1NC alloys obtained by (OM)
(a:1450 °C, b:1500 °C, c:1550 °C, 200x).
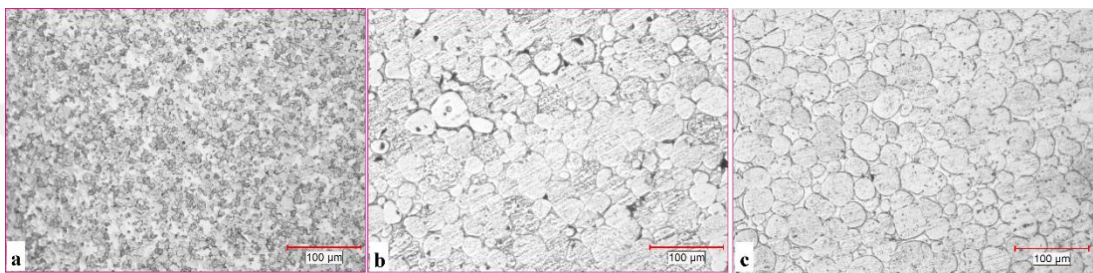
Figure B.14 Microstructure images of the 0W8/1NF alloys obtained by (OM)
(a:1450 °C, b:1500 °C, c:1550 °C, 200x).
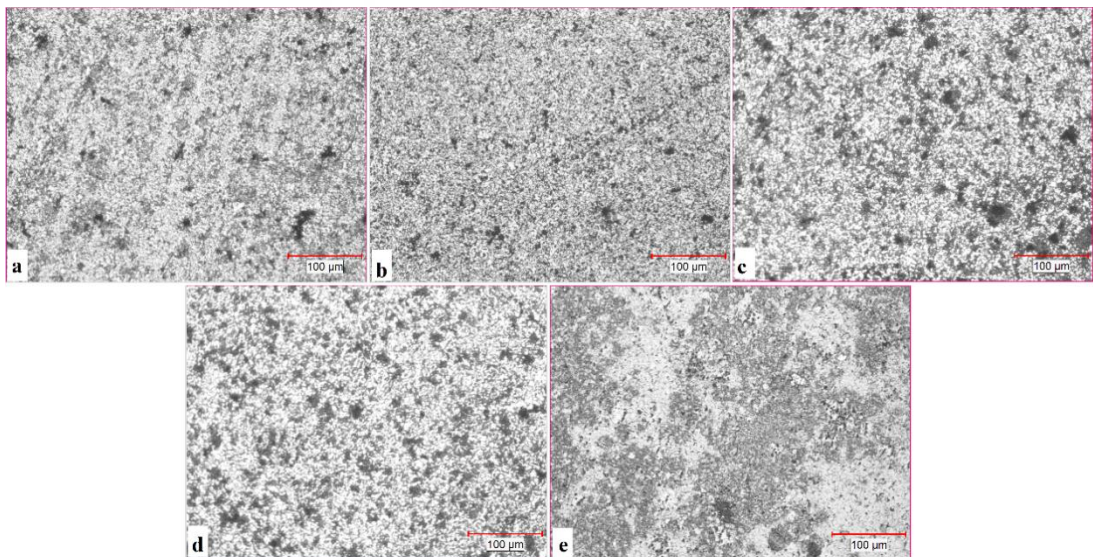
Figure B.15 Microstructure images of the 5W1/4NC alloys obtained by (OM)
(a:1450 °C, b:1500 °C, c:1550 °C, d:1550 °C/90 min, e:1550 °C/120 min, 200x).
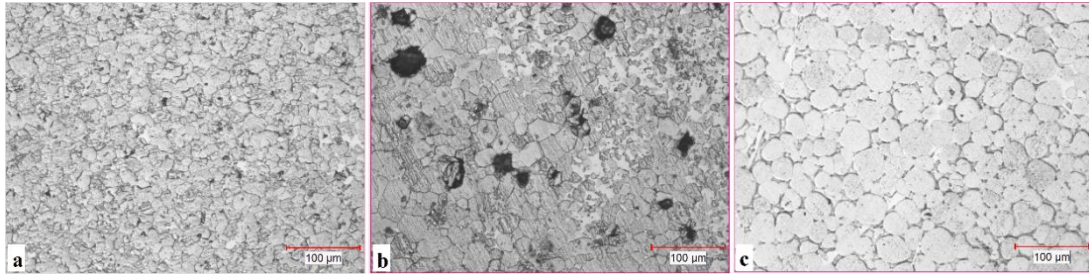
Figure B.16 Microstructure images of the 5W1/1NC alloys obtained by (OM)
(a:1450 °C, b:1500 °C, c:1550 °C, 200x).
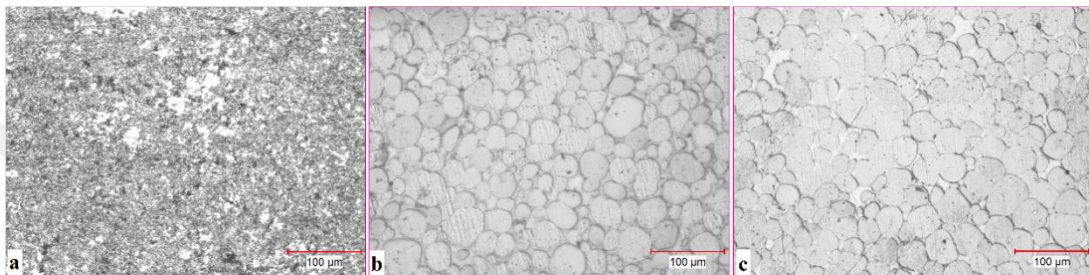
Figure B.17 Microstructure images of the 5W7/3NC alloys obtained by (OM)
(a:1450 °C, b:1500 °C, c:1550 °C, 200x).
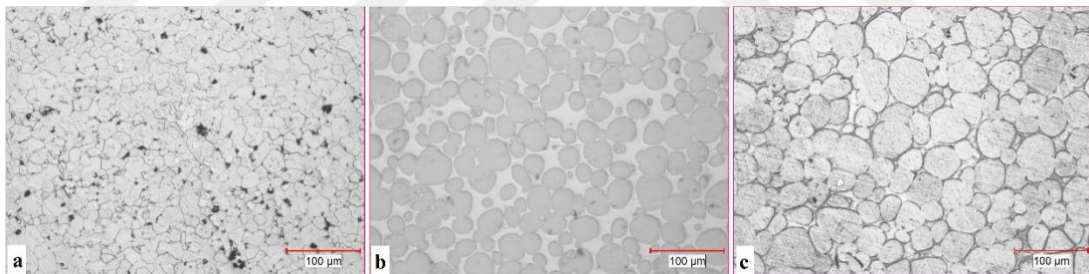
Figure B.18 Microstructure images of the 5W4/1NC alloys obtained by (OM)
(a:1450 °C, b:1500 °C, c:1550 °C, 200x).
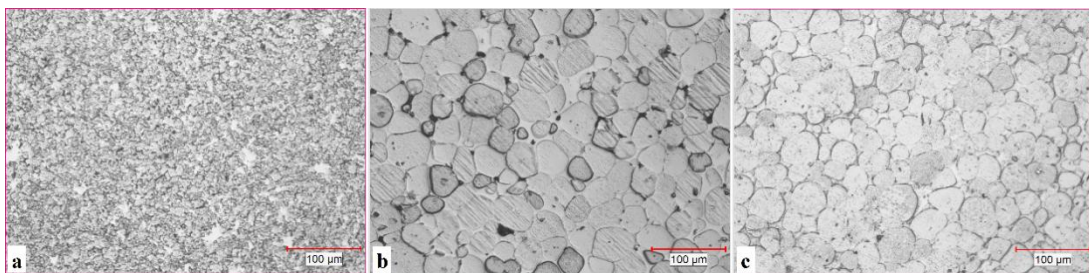
Figure B.19 Microstructure images of the 5W8/1NC alloys obtained by (OM)
(a:1450 °C, b:1500 °C, c:1550 °C, 200x).
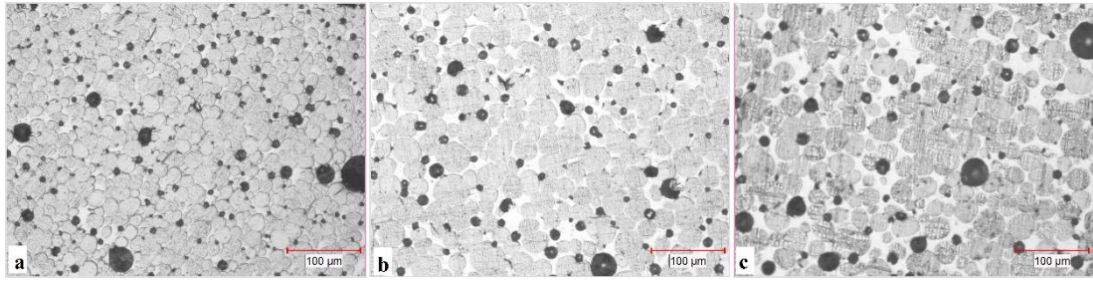
Figure B.20 Microstructure images of the 0W*7/3NF and 0W*7/3NC alloys
obtained by (OM) (a:0W*7/3NF at 1500 °C, b:0W*7/3NC at 1500 °C,
c:0W*7/3NC at 1550 °C, 200x).
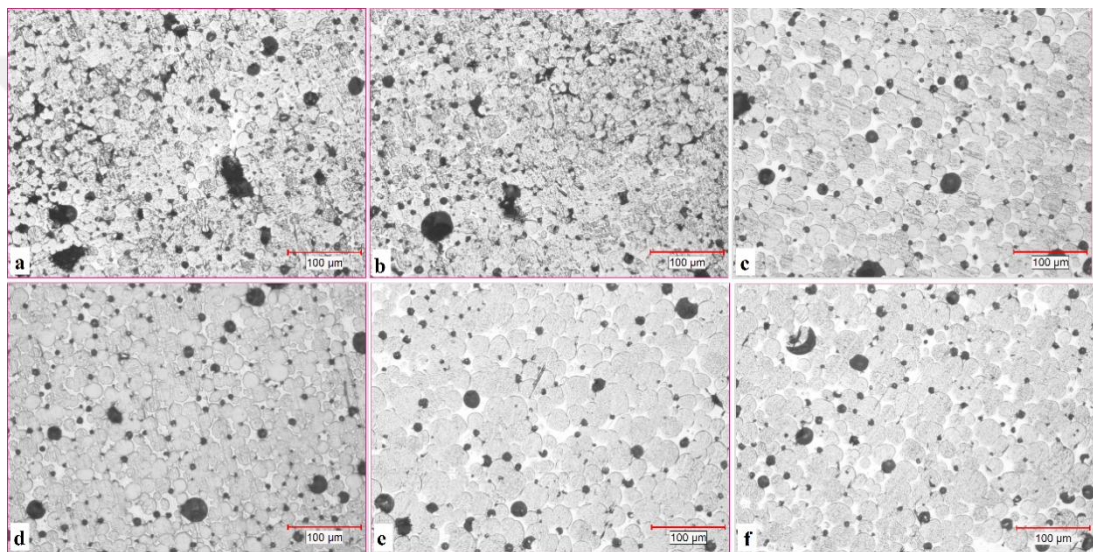
Figure B.21 Microstructure images of the 0W**4/1NC (a-b) and 0W*4/1NC (c-
d) alloys obtained by (OM) (a:1500 °C, b:1550 °C, c:CEP at1500 °C, d:CEP at
1550 °C, e:UHP at1500 °C, f:UHP at1550 °C, 200x).
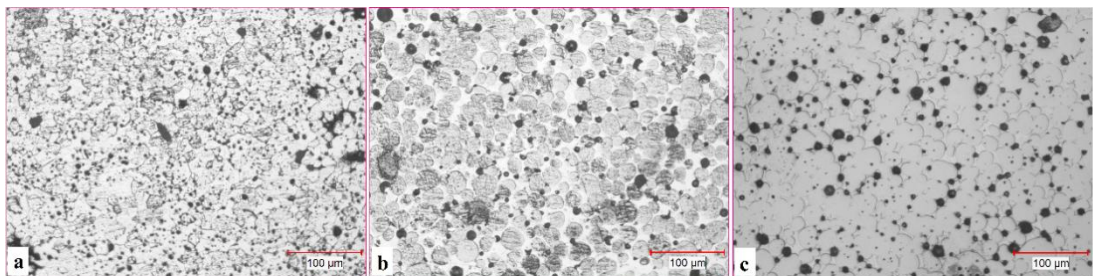
Figure B.22 Microstructure images of the 0W*8/1NC (a-b) and 5W*4/1NC (c)
alloys obtained by (OM) (a:1500 °C, b:1550 °C, c:1550 °C, 200x).

Appendix C – Related Phase Diagrams
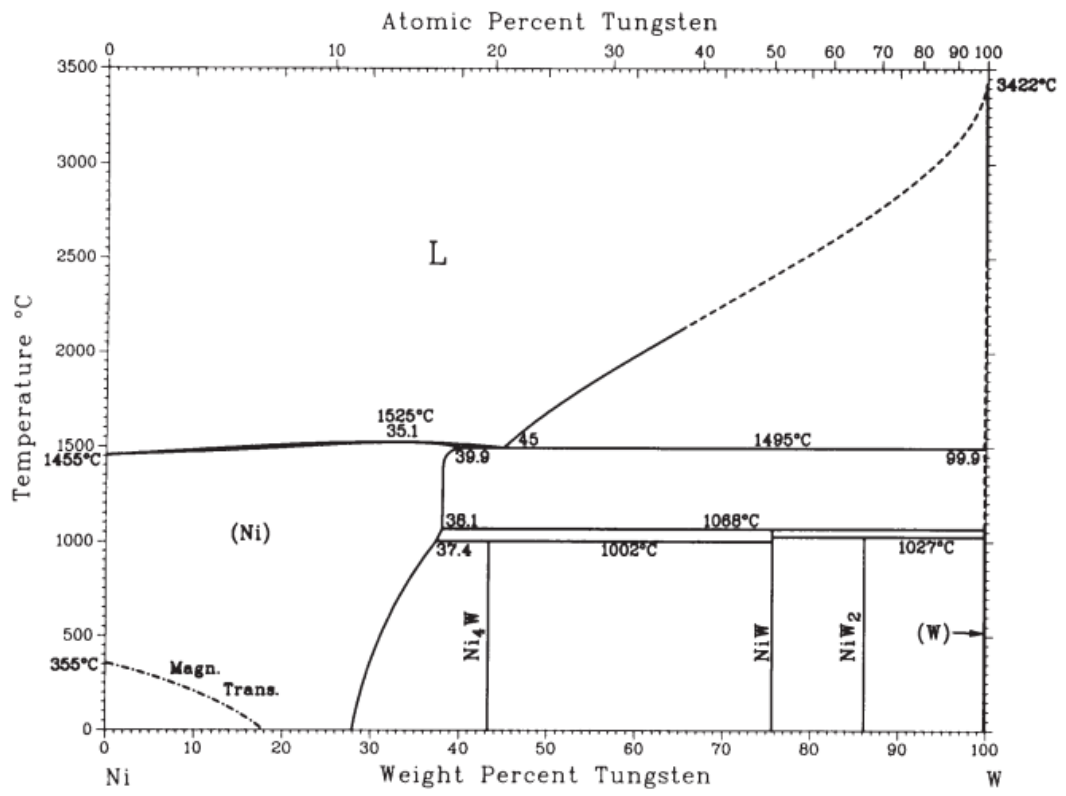
Figure C.1 Ni-W binary phase diagram [57].

As can be seen Figure C.1, solid state Ni can dissolve up to 39.9 wt.% W in its structure. Formed intermetallic phases such as Ni_4W, NiW and NiW_2 contained 44 wt.%, 78.8 wt.% and 86.3 wt.% W, respectively. Trace amount of Ni can be dissolved in W grains.
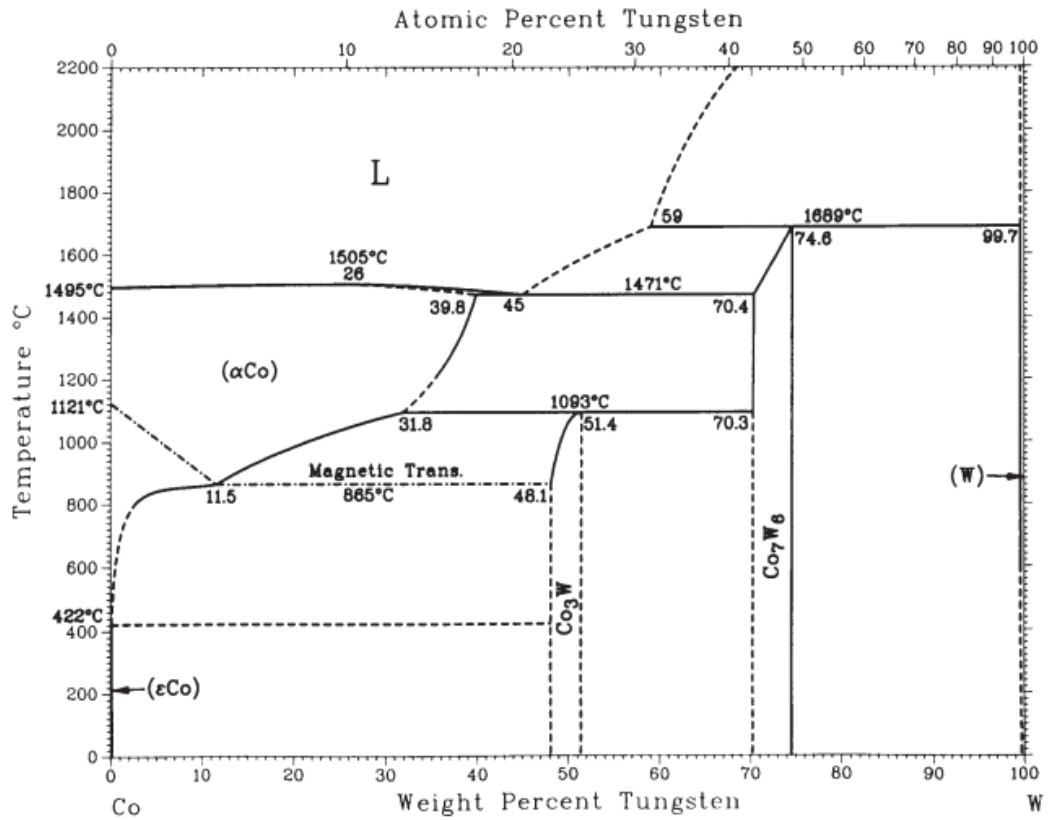
Figure C.2 Co-W binary phase diagram [57].

As can be seen Figure C.2, α-Co can dissolve up to 39.8 wt.% W in its structure, whereas εCo cannot dissolve the W. Formed intermetallic phases such as Co_3W and Co_7W_6 contained 48.1-51.4 wt.% and 70.3-74.6 wt.% W, respectively. Trace amount of Co can be dissolved in W.
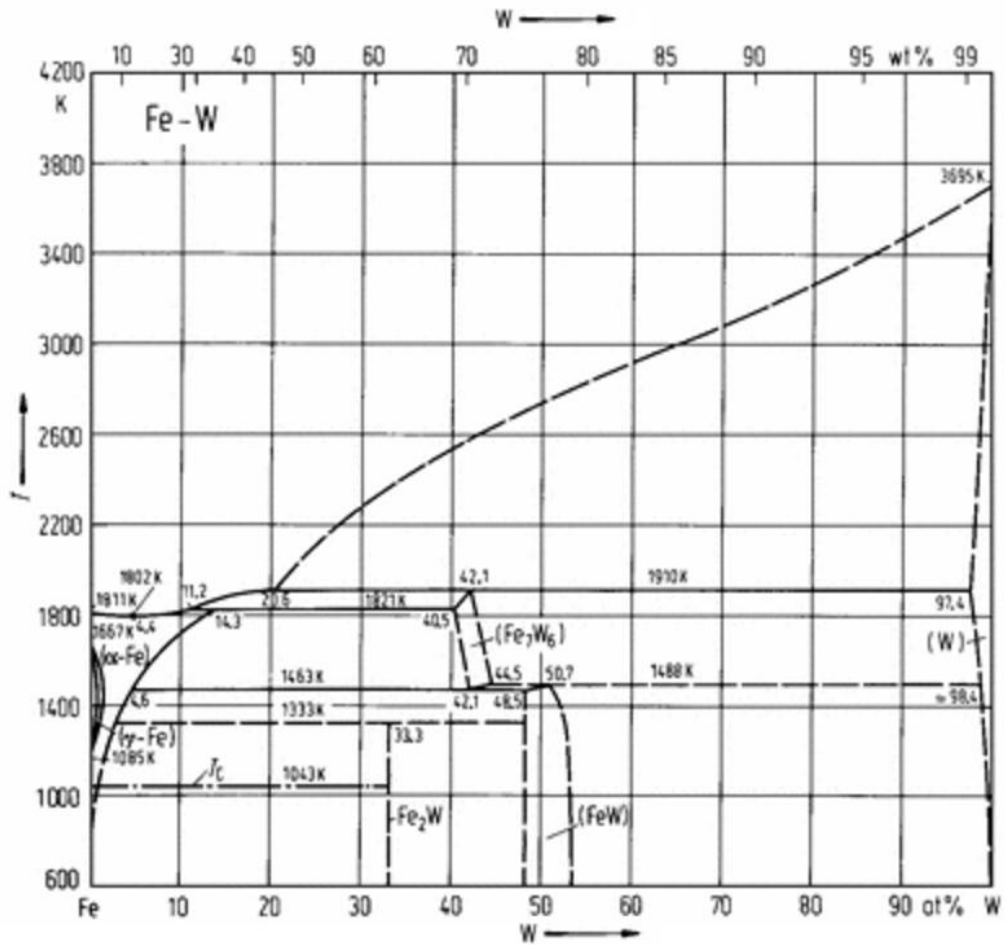
Figure C.3 Fe-W binary phase diagram [58].
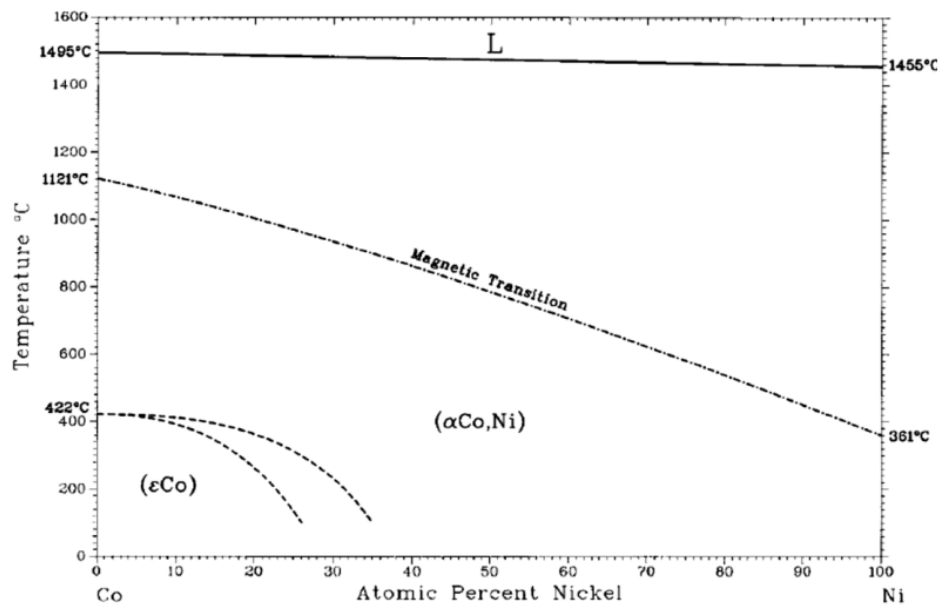
Figure C.4 Co-Ni binary phase diagram [57].
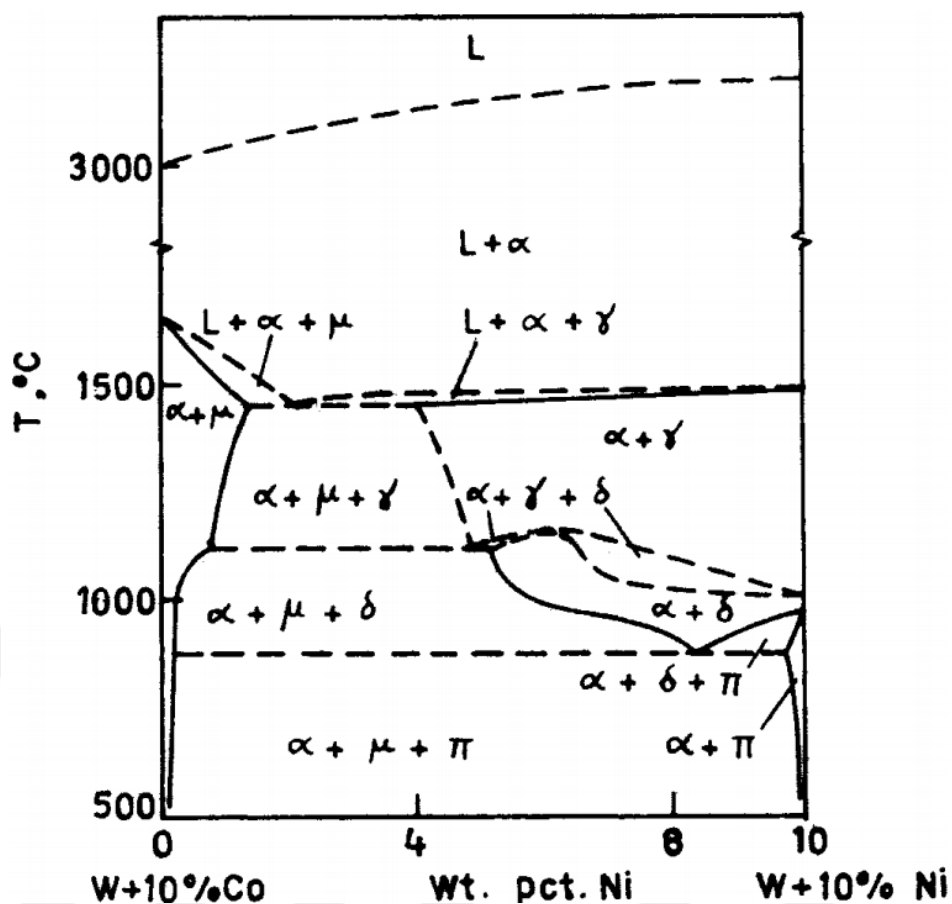
Figure C.5 Binary phase diagram of 10 wt.% (Co+Ni) added tungsten heavy alloys (1992 Nik) [47].

Reactions:

Table C.1 The reactions take place during solidification of W-rich Ni and Co added alloys [47].

Co-W	Co-Ni-W	Ni-W
P_1 L+α=μ (1689 °C)		E_1 L=α+γ (1497 °C)
E_2 L=μ+γ (1471 °C)	X L=α+δ+μ (T_1)	
P_2 γ+μ=φ (1094 °C)	L+γ+μ α+μ+γ	
P_3 γ+φ=ε (1050 °C)	U_1 α+γ = δ+μ (T_2)	
	γ+δ+μ α+δ+μ	P_4 α+γ=δ (1047 °C)
	U_2 α+δ = μ+π (T_3)	P_5 α+δ=π (1025 °C)
	α+π+μ δ+π+μ	P_6 γ+δ=π (992 °5C)

Where L is liquid phase, P is the peritectic reaction, E is the eutectic reaction, T is temperature, α is W terminal solid solution phase, μ is the Co_7W_6 intermetallic phase, γ is a FFC solid solution of Co and Ni, φ is Co_3W intermetallic phase, ε is a transformed solid solution of Co, δ is NiW intermetallic phase π is NiW_2 intermetallic phase.
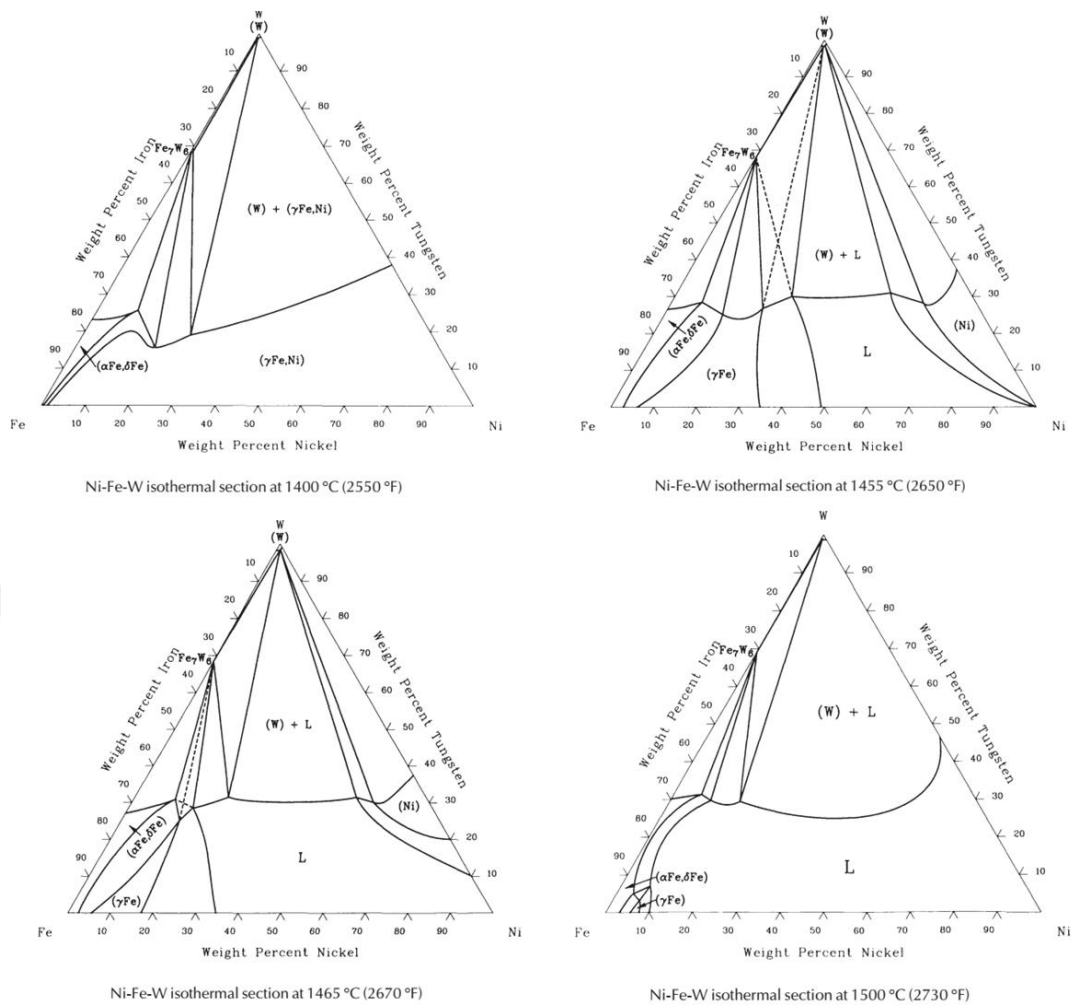
Figure C.6 Ternary phase diagram of W-Ni-Fe [57].
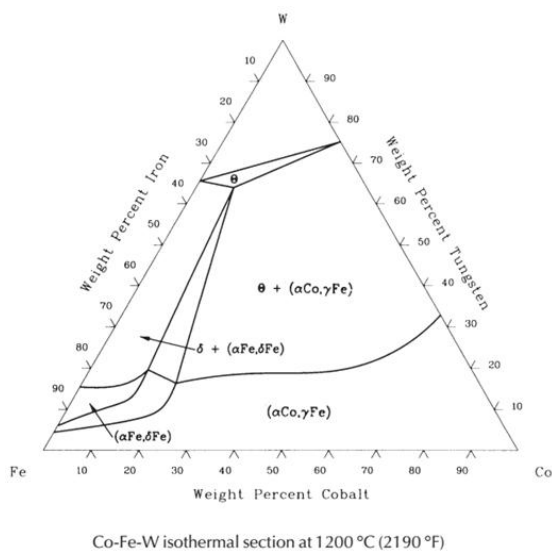
Figure C.7 Ternary phase diagram of W-Co-Fe[57].

Appendix D – Micro and Macro Scale Hardness Measurements

Table D.1 Hardness results of selected alloys obtained from HV(1).

| Alloy code | Applied sintering process | | | | | | | | | | | |
| | 1450 °C/60min | | | 1500 °C/60min | | | 1550 °C/60min | | | 1550 °C/90-120min | | |
	Min	Avg	Max	Min	Avg	Max	Min	Avg	Max	Min	Avg	Max
W	-	-	-	165	210	221	177	226	232	-	-	
W*	-	-	-	380	385	388	408	420	424	-	-	-
W**	-	-	-	362	368	376	380	384	392	-	-	-
0W10N	355	357	365	418	428	435	391	398	446	359/-	363/-	384/-
0W10C	157	168	182	194	200	209	278	280	286	337/-	387/-	403/-
0W10F	139	168	177	207	223	236	301	320	325	288/-	301/-	345/-
0W1/4NC	290	301	305	312	404	568	591	595	606	542/-	557/-	574/-
0W1/1NC	414	431	504	412	442	479	458	488	497	-	-	-
0W7/3NC	335	344	350	379	384	397	332	368	385	-	-	-
0W7/1.5/1.5NCF	288	322	360	354	376	384	321	342	365	-	-	-
0W7/3NF	319	337	350	338	343	354	305	317	327	-	-	-
0W4/1NC	307	318	344	350	363	379	327	333	348	-	-	-
0W8/1NC	379	404	431	365	379	395	397	399	407	-	-	-
0W8/1NF	321	346	381	330	351	372	348	368	376	-	-	-
0W*7/3NC	-	-	-	345	354	362	390	397	423	-	-	-
0W*7/3NF	-	-	-	313	318	331	-	-	-	-	-	-
0W*4/1NC	-	-	-	328	343	360	353	363	368	-	-	-
0W**4/1NC	-	-	-	307	319	325	314	327	335	-	-	-
0W*8/1NC	-	-	-	343	356	370	-	-	-	-	-	-
0W1/4CF	-	-	-	346	378	383	383	392	403	393/-	425/-	472/-
0W1/1CF	-	-	-	374	384	391	416	436	441	446/-	450/-	458/-
0W4/1CF	-	-	-	348	361	365	481	517	534	484/-	487/-	520/-
5W1/4NC	261	271	273	340	345	364	424	457	471	431/-	436/-	457/-
5W1/1NC	406	433	449	417	467	487	382	397	433	-	-	-
5W7/3NC	346	359	369	362	385	392	319	346	363	-	-	-
5W4/1NC	280	284	311	366	373	395	332	339	352	-	-	-
5W8/1NC	334	356	364	342	347	379	311	327	361	-	-	-
5W*4/1NC	-	-	-	-	-	-	363	371	373	-	-	-

Table D.2 Hardness results of selected binder phases HV(0.005).

Alloy code	1450 °C/60min			1500 °C/60min			1550 °C/60min			1550 °C/90-120min		
	Min	Avg	Max	Min	Avg	Max	Min	Avg	Max	Min	Avg	Max
W	-	-	-	-	-	-	-	-	-	-	-	-
W*	-	-	-	-	-	-	-	-	-	-	-	-
W**	-	-	-	-	-	-	-	-	-	-	-	-
0W10N	-	-	-	365	393	433	383	415	438	-	-	-
0W10C	-	-	-	-	-	-	-	-	-	-	-	-
0W10F	-	-	-	-	-	-	-	-	-	-	-	-
0W1/4NC	-	-	-	-	-	-	-	-	-	-	-	-
0W1/1NC-D	-	-	-	444	483	526	465	505	579	-	-	-
0W1/1NC-L				1362	1754	2318	1215	1856	2358			
0W7/3NC	-	-	-	338	393	528	463	505	672	-	-	-
0W7/1.5/1.5NCF	-	-	-	409	463	528	386	427	456	-	-	-
0W7/3NF	-	-	-	426	463	483	393	444	483	-	-	-
0W4/1NC	-	-	-	386	444	505	364	469	553	-	-	-
0W8/1NC	-	-	-	409	444	483	429	442	549	-	-	-
0W8/1NF	-	-	-	483	505	528	469	515	532	-	-	-
0W*7/3NC	-	-	-	345	356	378	356	383	411	-	-	-
0W*7/3NF	-	-	-	383	408	432	-	-	-	-	-	-
0W*4/1NC	-	-	-	356	376	393	364	376	403	-	-	-
0W**4/1NC	-	-	-	384	432	463	393	415	428	-	-	-
0W*8/1NC	-	-	-	426	483	528	428	-	-	-	-	-
0W4/1CF	-	-	-	-	-	-	-	-	-	-	-	-
0W1/1CF	-	-	-	-	-	-	-	-	-	-	-	-
0W1/4CF	-	-	-	-	-	-	-	-	-	-	-	-
5W1/4NC	-	-	-	-	-	-	-	-	-	-	-	-
5W1/1NC-D	-	-	-	505	608	672	505	579	639	-	-	-
5W1/1NC-L				1512	1932	2555	1215	1775	2112			
5W7/3NC	-	-	-	364	436	483	505	528	579	-	-	-
5W4/1NC	-	-	-	393	463	528	378	444	483	-	-	-
5W8/1NC	-	-	-	436	528	553	315	409	505	-	-	-
5W*4/1NC	-	-	-	-	-	-	463	505	553	-	-	-

D and L imply the dark and light region at 1/1 Ni/Co ratio alloys, respectively.

Table D.3 Hardness results of selected alloys obtained from HRA.

Alloy code	Applied sintering process											
	1450 °C/60min			1500 °C/60min			1550 °C/60min			1550 °C/90-120min		
	Min	Avg	Max	Min	Avg	Max	Min	Avg	Max	Min	Avg	Max
W	-	-	-	-	-	-	-	-	-	-	-	-
W*	-	-	-	-	-	-	-	-	-	-	-	-
W**	-	-	-	-	-	-	-	-	-	-	-	-
0W10N	62.2	62.6	63.4	63.9	64.1	64.7	59.8	60.3	60.8	58.9	60.7	61.3
0W10C	44.8	45.3	46.8	49.6	50.3	52.4	55.7	56.2	57.5	54.4	55.0	56.5
0W10F	46.1	46.6	47.6	50.2	51.1	53.2	56.3	56.9	58.2	58.8	60.8	61.3
0W1/4NC	56.4	56.7	57.2	64.1	64.5	66.1	69.8	70.9	72.1	69.6/	69.7/	70.3/
0W1/1NC	66.2	66.8	68.1	67.2	67.8	68.2	65.6	66.8	68.7	-	-	-
0W7/3NC	61.7	62.9	64.2	63.6	63.9	65.0	60.5	61.2	62.4	-	-	-
0W7/1.5/1.5NCF	61.9	62.4	63.0	62.6	62.9	63.5	58.6	60.9	61.3	-	-	-
0W7/3NF	61.8	62.5	63.3	61.5	62.0	62.8	58.4	58.7	60.4	-	-	-
0W4/1NC	63.4	63.9	64.3	58.6	60.8	61.7	60.5	61.6	62.3	-	-	-
0W8/1NC	62.6	63.2	64.1	63.1	63.5	64.6	60.7	61.2	62.2	-	-	-
0W8/1NF	62.4	63.2	63.8	61.1	61.7	62.2	59.7	60.4	60.7	-	-	-
0W*7/3NC	-	-	-	59.6	60.8	61.7	60.8	61.4	62.1	-	-	-
0W*7/3NF	-	-	-	56.2	58.4	59.3	-	-	-	-	-	-
0W*4/1NC	-	-	-	/60.8	/61.2	/62.3	/59.4	/59.7	/60.4	-	-	-
0W**4/1NC	-	-	-	-	-	-	-	-	-	-	-	-
0W*8/1NC	-	-	-	52.6	53.5	54.8	-	-	-	-	-	-
0W4/1CF	-	-	-	58.6	59.0	59.6	64.1	64.8	65.3	63.8	64.1	64.7
0W1/1CF	-	-	-	60.1	60.5	61.4	63.2	64.1	65.4	63.1	63.7	63.9
0W1/4CF	-	-	-	57.2	57.5	58.4	66.4	67.1	68.6	62.1	63.0	63.4
5W1/4NC	55.6	55.9	56.4	61.4	61.8	62.3	64.1	64.3	65.2	-	-	-
5W1/1NC	62.4	62.8	63.1	65.6	65.8	66.4	59.8	61.8	63.4	-	-	-
5W7/3NC	62.8	63.1	63.8	59.3	59.6	60.3	58.6	59.3	60.9	-	-	-
5W4/1NC	61.1	61.4	62.6	62.6	63.2	63.7	58.6	59.5	61.7	-	-	-
5W8/1NC	61.4	62.1	62.7	61.6	62.4	63.1	57.9	58.6	62.1	-	-	-
5W*4/1NC	-	-	-	-	-	-	54.0	54.7	55.1	-	-	-

Appendix E – Dissolved wt.% W in Binder Matrix Phase

Table E.1 EDS results of binder matrix phases obtained from WHAs.

Alloy code	Applied sintering process															
	1500 °C/60min				1550 °C/60min				1550 °C/90min				1550 °C/120min			
	W	Ni	Co	Fe	W	Ni	Co	Fe	W	Ni	Co	Fe	W	Ni	Co	Fe
0W10N	40.07	59.93	-	-	40.46	59.54	-	-	42.38	57.62	-	-	-	-	-	-
0W10C	76.13	-	23.87	-	77.14	-	22.86	-	76.84	-	23.16	-	-	-	-	-
0W10F	74.28	-	-	25.72	74.09	-	-	25.91	75.06	-	-	24.94	-	-	-	-
0W1/4NC	75.79	5.57	18.65	-	75.83	5.96	18.22	-	76.42	5.14	18.44	-	76.85	4.58	18.57	-
0W1/1NC	41.38	34.46	24.16	-	43.64	32.71	23.65	-	-	-	-	-	-	-	-	-
0W7/3NC	42.46	40.70	16.84	-	44.80	39.17	16.04	-	-	-	-	-	-	-	-	-
0W7/1.5/1.5NCF	32.96	46.26	10.11	10.66	35.24	45.12	9.99	9.64	-	-	-	-	-	-	-	-
0W7/3NF	26.26	51.84	-	21.90	26.77	51.94	-	21.29	-	-	-	-	-	-	-	-
0W4/1NC	42.37	44.58	13.05	-	44.41	44.07	11.52	-	-	-	-	-	-	-	-	-
0W8/1NC	42.15	51.32	6.53	-	42.78	50.68	6.54	-	-	-	-	-	-	-	-	-
0W8/1NF	33.67	58.57	-	7.76	38.73	54.43	-	6.84	-	-	-	-	-	-	-	-
0W1/4CF	75.51	-	5.21	19.28	75.71	-	5.67	18.62	74.80	-	6.08	19.12	77.38	-	4.89	17.73
0W1/1CF	74.82	-	12.59	12.59	74.30	-	11.76	13.93	74.85	-	12.62	12.53	75.52	-	12.27	12.31
0W4/1CF	75.36	-	19.83	4.81	77.10	-	17.64	5.26	75.81	-	19.09	5.10	77.61	-	17.47	4.92
5W1/4NC	75.24	4.73	20.03	-	75.82	4.88	19.30	-	76.18	5.03	19.79	-	77.43	4.72	17.85	-
5W1/1NC	42.67	34.42	22.91	-	44.69	29.32	25.99	-	-	-	-	-	-	-	-	-
5W7/3NC	35.29	47.41	17.29	-	43.39	39.53	17.08	-	-	-	-	-	-	-	-	-
5W4/1NC	35.18	52.12	12.70	-	38.53	49.55	11.92	-	-	-	-	-	-	-	-	-
5W8/1NC	34.46	58.00	7.54	-	44.76	49.41	5.83	-	-	-	-	-	-	-	-	-

Table E.2 EDS results of binder matrix phases obtained from W*HAs.

Alloy code	Applied sintering process							
	1500 °C/60min				1550 °C/60min			
	W^R	Ni	Co	Fe	W^R	Ni	Co	Fe
0W*7/3NC	35.25	45.22	19.53	-	42.13	38.52	19.35	-
0W*7/3NF	34.42	44.71	-	20.87	-	-	-	-
0W*4/1NC	38.89	49.69	11.42	-	41.18	47.59	11.23	-
0W**4/1NC	39.70	48.40	11.90	-	42.51	46.82	10.67	-
0W*8/1NC	40.27	52.55	-	7.18	-	-	-	-
5W*4/1NC	-	-	-	41.54	46.93	11.53	-	

R implies produced tungsten.

Appendix F – Average Grain Size Measurements

Table F.1 Average grain size results of selected alloys.

Alloy code	Applied sintering process (°C/min)								
	1500/60			1550/60			1550/90-120		
	Measured AGS			Measured AGS			Measured AGS		
	Min.	Avg.	Max.	Min.	Avg.	Max.	Min.	Avg.	Max.
W	-	-	-	-	-	-	-	-	-
W*	-	-	-	-	-	-	-	-	-
W**	-	-	-	-	-	-	-	-	-
0W10N	24.6	25.1	26.3	28.7	29.3	30.2	-	-	-
0W10C	-	-	-	-	-	-	-	-	-
0W10F	-	-	-	-	-	-	-	-	-
0W1/4NC	-	-	-	-	-	-	-	-	-
0W1/1NC	25.6	26.3	26.8	30.7	32.2	31.3	-	-	-
0W7/3NC	26.2	26.5	28.4	29.4	30.0	31.5	-	-	-
0W7/1.5/1.5NCF	26.5	27.0	27.4	28.9	29.2	29.7	-	-	-
0W7/3NF	26.7	27.1	28.2	29.8	30.7	30.9	-	-	-
0W4/1NC	27.1	27.4	28.2	29.6	30.5	30.7	-	-	-
0W8/1NC	27.2	27.6	27.9	31.3	31.9	32.7	-	-	-
0W8/1NF	27.3	27.9	28.3	31.9	32.2	33.2	-	-	-
0W*7/3NC	24.7	25.2	26.3	27.6	27.9	28.5	-	-	-
0W*7/3NF	24.6	24.7	26.1	-	-	-	-	-	-
0W*4/1NC	26.2	26.8	28.3	27.9	28.3	29.1	-	-	-
0W**4/1NC	24.1	24.4	24.7	26.3	26.7	27.2	-	-	-
0W*8/1NC	26.7	27.2	28.1	-	-	-	-	-	-
0W4/1CF	-	-	-	-	-	-	-	-	-
0W1/1CF	-	-	-	-	-	-	-	-	-
0W1/4CF	-	-	-	-	-	-	-	-	-
5W1/4NC	-	-	-	-	-	-	-	-	-
5W1/1NC	27.3	27.8	28.0	32.4	33.2	33.5	34.4	34.8	35.7
5W7/3NC	26.4	27.9	28.4	30.7	31.5	31.7	-	-	-
5W4/1NC	27.2	28.1	28.7	30.7	31.3	32.0	-	-	-
5W8/1NC	27.9	28.8	29.2	30.9	31.4	32.3	-	-	-
5W*4/1NC	-	-	-	28.2	28.5	29.1	-	-	-

Appendix G – % Binder Phase Area Measurements

Table G.1 Binder phase measurements for selected WHAs and W*HAs.

Alloy code	Applied sintering process (°C/min)								
	1500/60			1550/60			1550/90-120		
	Measured AGS			Measured AGS			Measured AGS		
	Min.	Max.	Avg.	Min.	Max.	Avg.	Min.	Max.	Avg.
W	-	-	-	-	-	-	-	-	-
W*	-	-	-	-	-	-	-	-	-
W**	-	-	-	-	-	-	-	-	-
0W10N	19.7	23.8	20.9	20.7	27.3	23.6	-	-	-
0W10C	-	-	-	-	-	-	-	-	-
0W10F	-	-	-	-	-	-	-	-	-
0W1/4NC	-	-	-	-	-	-	-	-	-
0W1/1NC	-	-	-	-	-	-	-	-	-
0W7/3NC	17.8	22.1	19.3	15.8	23.5	20.7	-	-	-
0W7/1.5/1.5NCF	18.6	21.8	20.1	17.9	24.7	22.4	-	-	-
0W7/3NF	20.8	23.4	22.8	19.6	25.8	23.8	-	-	-
0W4/1NC	17.4	24.6	21.1	17.6	24.9	21.4	-	-	-
0W8/1NC	17.9	25.5	21.5	18.4	26.1	22.7	-	-	-
0W8/1NF	18.3	26.7	22.1	19.6	29.3	24.4	-	-	-
0W*7/3NC	20.6	25.7	24.1	21.7	26.7	25.0	-	-	-
0W*7/3NF	21.8	28.5	24.7	-	-	-	-	-	-
0W*4/1NC	20.9	26.7	23.8	21.8	29.1	24.9	-	-	-
0W**4/1NC	-	-	-	20.3	25.7	23.8	-	-	-
0W*8/1NC	19.1	26.2	23.9	-	-	-	-	-	-
0W1/4CF	-	-	-	-	-	-	-	-	-
0W1/1CF	-	-	-	-	-	-	-	-	-
0W4/1CF	-	-	-	-	-	-	-	-	-
5W1/4NC	-	-	-	-	-	-	-	-	-
5W1/1NC	-	-	-	-	-	-	-	-	-
5W7/3NC	11.9	13.9	13.1	10,9	14.1	13.4	-	-	-
5W4/1NC	10.7	13.7	13.0	11.2	14.3	13.8	-	-	-
5W8/1NC	12.1	14.6	13.4	11.5	14.8	14.1	-	-	-
5W*4/1NC	-	-	-	14.3	19.2	17.3	-	-	-

CURRICULUM VITAE

PERSONAL INFORMATION

Name Surname : Mahmut EROL

Date of Birth : 05.01.1988

Phone : +90 538 0133609

E-mail : merol@ybu.edu.tr
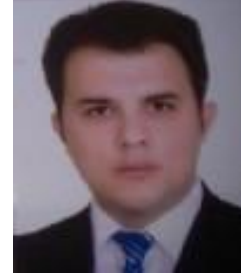
EDUCATION

High School : Merkez Super High School / İSTANBUL (2002-2006)
(4.08/5.00)

Bachelor : Yıldız Technical University / İSTANBUL (2007-2012)
(3.59/4.00)

Master Degree : Ankara Yıldırım Beyazıt University / (2014-continued)

WORK EXPERIENCE

Research Assist. : Ankara Yıldırım Beyazıt University / (2014-2017)

Research Assist. : Yıldız Technical University / (2017-continued)

TOPICS OF INTEREST

- Powder Metallurgy
- Microstructure Phase Relation
- Welding Metallurgy and NDT
- Heat Treatment Processes
- Corrosion, Metal Fatigue